Applications of regional ocean Ensemble Kalman Filter data assimilation

Imperial College
London

Yi Li

Department of Physics

Imperial College London

This dissertation is submitted for the degree of

Doctor of Philosophy

September 2018

I would like to dedicate this thesis to my family.

Declaration of Originality

I hereby declare that except where specific reference is made to the work of others, the contents of this dissertation are original and have not been submitted in whole or in part for consideration for any other degree or qualification in this, or any other university. This dissertation is my own work and contains nothing which is the outcome of work done in collaboration with others, except as specified in the text and Acknowledgements. Most of the work presented in this thesis has been published or submitted for publication:

Li, Y. and Toumi, R., 2017. A balanced Kalman filter ocean data assimilation system with application to the South Australian Sea. Ocean Modelling, 116, pp.159-172.

Li, Y. and Toumi, R., 2018. Improved tropical cyclone forecast by assimilating coastal surface currents in an idealized study. Geophysical Research Letters, Under review.

Yi Li
September 2018

Declaration of Copyright

Yi Li
September 2018

Abstract

Data assimilation has been widely used in the forecast of oceanic states and tropical cyclones. In this thesis, the Ensemble Kalman Filter (EnKF) based data assimilation algorithm is applied to two applications, a regional ocean data assimilation system for the South Australian Sea and a coupled ocean-atmosphere tropical cyclone (TC) forecast system.

The regional ocean data assimilation system consists of the data assimilation algorithm provided by the NCAR Data Assimilation Research Testbed (DART) and the Regional Ocean Modelling System (ROMS). We describe the first implementation of a physical balance operator (temperature-salinity, hydrostatic and geostrophic balance) to DART, to reduce the spurious waves which may be introduced during the data assimilation process. The effect of the balance operator is validated in both an idealised shallow water model and the ROMS model real case study. In the shallow water model, the geostrophic balance operator eliminates spurious ageostrophic waves and produces a better sea surface height (SSH) and velocity analysis and forecast. Its impact increases as the sea surface height and wind stress increase. In the real case, satellite-observed sea surface temperature (SST) and SSH are assimilated in the South Australian Sea with 50 ensembles using the Ensemble Adjustment Kalman Filter. Assimilating SSH and SST enhances the estimation of SSH and SST in the entire domain, respectively. Assimilation with the balance operator produces a more realistic simulation of surface currents and subsurface temperature profile. The best improvement is obtained when only SSH is assimilated with the balance operator. A case study with a storm suggests that the benefit of the balance operator is of particular importance under high wind stress conditions. Implementing the balance operator could be a general benefit to ocean data assimilation systems.

The TC forecast system consists of DART and coupled ROMS - WRF (the Weather Research Forecast model). High-frequency (HF) radars can provide high-resolution and frequent ocean surface currents observations during the TC landfall. We describe the first assimilation of such potential observations using idealised Observing System Simulation Experiments. In this system, synthetic HF radar observed coastal currents are assimilated and the forecast performances for weak (Category 2) and strong (Category 4) TCs are examined. Assimilating coastal surface currents improves the 24-hour forecasts of both intensity and track. For the strong case, the errors of the maximum wind speed (V_{max}) and the integrated power dissipation (IPD) forecast reduce up to 50%. For the weak case, the improvements in V_{max} and IPD forecast are lower (20%), but the track forecast improves 30%. These improvements are similar to the magnitude of the current operational TC forecast error, so that assimilating HF radar observations could be a substantial benefit.

Contents

List of Figures

List of Tables

Chapter 1

Introduction

1.1 The Data Assimilation Problem

The early civilisations began the prediction of atmospheric and oceanic states millennia ago. One of the main purposes for the study of atmospheric and oceanic circulation is the people's desire of forecast. In the early 1900s, Abbe and Bjerknes proposed that the weather could be predicted using the laws of physics (Bauer et al., 2015). Later, L. F. Richardson carried out the first numerical weather prediction in the 1920s, although he failed due to the lack of the geostrophic balance in the initial conditions and, probably more importantly, the lack of modern computers (Lynch, 2008; Shuman, 1989, https://www.metoffice.gov.uk/research/modelling-systems/history-of-numerical-weather-prediction).

Bjerknes defined the prediction as an initial value problem, and two conditions must be satisfied for successful predictions (Daley, 1991): '1. the present state must be characterized as accurately as possible; 2. the intrinsic laws, according to which the subsequent states develop out of the preceding ones, must be known.' This was later defined as determined approach. The second condition is usually satisfied by the development of General Circulation Models (GCMs). The first condition leads to the analysis of the observations, such that the atmospheric and oceanic variables are produced at points with fixed spatial resolution, as the initial values. These initial conditions were produced by interpolating the observations, later this procedure was replaced by data assimilation based on optimal control theory (Daley, 1991). The data assimilation technique combines the observational data with the short-term model forecast, and the product is called analysis. Accurate analysis is crucial for the operational forecasts.

The purpose of data assimilation is seeking a state which is the best fit between a short-term forecast (or background estimate or prior state), and a set of observations, given the probability distribution functions (PDFs) of the short-term forecast and observations. The Bayesian theorem is the cornerstone of data assimilation, which provides an objective criterion for fusing observations with numerical models to produce an estimate of the true state (e.g. Lahoz and Schneider, 2014; Wikle and Berliner, 2007).

The Bayes inference consists of three steps (Wikle and Berliner, 2007): 'In the first, a 'full probability model' is formulated, which is a joint probability distribution of all observable and unobservable components of interest. The next step in this process is to find the conditional distribution of the unobservable quantities of interest given the observed data by application of Bayes' Theorem. Finally, as with all modelling, one should evaluate the fit of the model and its ability to adequately characterise the processes of interest.'

The background or *prior* PDF of the state, $p(x)$, represents the distribution of possible values of the state, given all prior modelled information, and has an expected value x^b. At some point in time, the forecast estimate is informed by a vector of observations y, which has a PDF $p(y|x)$, or the conditional PDF of the observations, given the state estimate. The Bayes' theorem states that the conditional posterior PDF of the state, given the new observations and the prior PDF, is given by

$$p(x|y) = \frac{p(y|x)p(x)}{p(y)}, \tag{1.1}$$

$p(y)$ is the PDF of the observation vector, which acts as a normalising factor and guarantees that the probability of all possible states x is unity. It is given by $p(y) = \int p(y|x')p(x')dx'$ (Anderson and Anderson, 1999).

The state which we seek, called the analysis (x^a), is the most probable state of the joint PDF (Eq. 1.1). With the assumption of Gaussian distributions, one can compute the estimate x which minimises the mean of the square error, called the least-squares or variance-minimising estimator. This state can be written as a linear combination of the background state and the observation vector,

$$x^a = Fx^f + GH(x^f) + Ky + c, \tag{1.2}$$

where F, G and K are matrices and c is a vector; and x^f is the forecast (prior) state For the true states x_t and y_t ($y_t = H(x_t)$), Eq 1.2 is

$$x_t = Fx_t + GH(x_t) + KH(x_t) + c. \tag{1.3}$$

Because Eq. 1.3 applies for any x_t and y_t, we must have $c = 0$ and $F + GH(\cdot) + KH(\cdot) = I$. So the analysis is $x^a = x^f + Kd$, in which K is called the gain matrix and $d = y - H(x^f)$ is called the innovation. Under the assumption of linearity, $H(x)$ can be written in the linear form HX.

Substituting the expressions of x^a and K into Eq. 1.2 and using $Hx_t = y_t$, the errors can be written as

$$\begin{aligned} \epsilon^a &= \epsilon^f + K(\epsilon^o - H\epsilon^f) \\ &= (I - KH)\epsilon^b + K\epsilon^o, \end{aligned} \tag{1.4}$$

where ϵ^a, ϵ^f and ϵ^o are the errors of the analysis, the forecast and the observation, respectively (e.g., $\epsilon^a = x^a - x^t$, where x^t is the truth). We also assume that the errors are uncorrelated with each other.

For the multivariate problem, the error covariance of the analysis is

$$\begin{aligned} P^a &= \overline{\epsilon^a(\epsilon^a)^T} \\ &= \overline{((I - KH)\epsilon^f + K\epsilon^o)((I - KH)\epsilon^f + K\epsilon^o)^T} \\ &= (I - KH)\overline{\epsilon^f(\epsilon^b)^T}(I - KH)^T + (I - KH)\overline{\epsilon_b(\epsilon^o)^T}K^T \\ &+ K\overline{\epsilon_o(\epsilon^f)^T}(I_K H)^T + K\overline{\epsilon_o(\epsilon^o)^T}K^T. \end{aligned} \tag{1.5}$$

Recall that the forecast and observation errors are uncorrelated, so

$$P^a = (I - KH)\overline{\epsilon^f(\epsilon^f)^T}(I - KH)^T + K\overline{\epsilon_o(\epsilon^o)^T}K^T. \tag{1.6}$$

To minimise the analysis error, we need the variance (i.e., the diagonal elements of the covariance matrix) to be 0, i.e.,

$$\frac{\partial trace(\overline{\epsilon^a(\epsilon^a)^T})}{\partial K} = 0. \tag{1.7}$$

Substituting Eq. 1.6 and using some linear algebra, Eq. 1.7 becomes

$$\frac{\partial trace(\overline{\epsilon^a(\epsilon^a)^T})}{\partial K} = 2K[H\overline{\epsilon^f(\epsilon^f)^T}H^T + \overline{\epsilon^o(\epsilon^o)^T}] - 2\overline{\epsilon^f(\epsilon^f)^T}H^T = 0. \tag{1.8}$$

Solving Eq. 1.8 gives

$$K = P^f H^T(HP^f H^T + R)^{-1}, \tag{1.9}$$

where P^f and R are the error covariance matrices, defined as

$$\begin{aligned} P^f &= \overline{(x-x^b)(x-x^b)^T}, \\ R &= \overline{(y-H(x))(y-H(x))^T}, \end{aligned} \tag{1.10}$$

and Eq. 1.2 becomes

$$x^a = x^b + K(y - Hx^f). \tag{1.11}$$

where P^f and R are the forecast and observation covariance matrices, respectively.

This gain matrix minimises the posterior error $\overline{(x-x^a)(x-x^a)^T}$, such that x^a is the best linear unbiased estimator (BLUE). The gain matrix can be interpreted easily in the case of one-dimensional state. Assume the forecast variance is σ_f^2 and the observation is a single value of the same variable (such that $H = 1$) with observation error variance σ_o^2, the gain matrix is the weights giving to observation and forecast, $K = \frac{\sigma_f^2}{\sigma_f^2+\sigma_o^2}$ and Eq. 1.11 is simplified as

$$x^a = x^f + \frac{\sigma_f^2}{\sigma_f^2+\sigma_o^2}(y - x^f). \tag{1.12}$$

When the observation is more accurate than the forecast (i.e., $\sigma_f^2 > \sigma_o^2$, $K \to 1$), more weight is given to the observation and vice versa.

In the numerical forecasting, the forecast states x^f are generated by integrating a model forward until the time at which an observation is made. The model evolution is as follows,

$$x_{k+1}^f = M_k(x_k^a) + q_k, \tag{1.13}$$

where M_k represents the forward evolution of the true state, q_k represents error of the forward evolution, x_k^a represents the analysis made at time-step k, and x_{k+1}^f is the forecast at time-step $k+1$. When an observation is made, a new analysis can be produced using Eq. 1.11, using this forecast as the background estimate. Then this analysis is used as initial conditions to produce new forecasts using Eq. 1.13. This process is repeated, to generate a series of forecasts and analyses. If the forecast error covariance B is static in time, this algorithm is called three-dimensional data assimilation.

If P^f evolves in time, then the algorithm is four-dimensional data assimilation. To do so, not only the model state is modelled, but also the evolution of the PDF (Eq. 1.1). Under the Gaussian assumption, only the mean and variance need to be computed. There are two popular data assimilation approaches: variational and sequential (Lahoz and Schneider, 2014). The variational approach adjusts the model trajectories to fit the observations by minimising the cost function. On the other hand, the sequential approach updates the model state by comparing the mean and variability of both model and data, each time when the new observation is available. These two approaches are both based on the Bayesian theorem and can be simplified to similar algorithms under the assumptions of Gaussianity and linearity. In this thesis we focus on the sequential approach, the ensemble Kalman Filter (EnKF) in particular.

1.1.1 The Ensemble Kalman Filter and Square Root Filters

The ensemble Kalman Filter (EnKF) approach was initially proposed by Evensen (1994). As indicated by its name, EnKF uses an ensemble of model states to update the forecast error covariance matrix B, and the model ensemble evolves with time. By doing so, EnKF preserves nonlinearity in the evolution of forecast error statistics, though it still retains the assumption that error PDFs are characterizable by their mean and covariance, and that the linear update (Eq. 1.11) is optimal. Another advantage of the EnKF is that, in contrast with the Four-dimensional variation (4DVAR), a popular variational approach, EnKF eliminates the cost of developing an adjoint model. As pointed by (Tippett et al., 2003), EnKF belongs to the family of *square root filters* (SRFs), here the derivation of SRF is given following Tippett et al. (2003).

The $n \times n$ prior and posterior error covariance matrices (P^f and P^a) are both symmetric and positive definite so they can be represented as $P^f = Z^f Z^{fT}$ and $P^a = Z^a Z^{aT}$, where the matrices Z^f and Z^a are matrix square roots of P^f and P^a, respectively. A covariance matrix and its matrix square root have the same rank or number of nonzero singular values. When a covariance matrix P has rank m, there is an nxm matrix square root Z satisfying $P = ZZ^T$; in low-rank covariance representations the rank m is much less than the state-space dimension n. This representation is not unique; P can also be represented as $P = (ZU)(ZU)^T$, where the matrix U is any $m \times m$ orthogonal transformation $UU^T = U^T U = I$. The projection $|x^T Z|^2 = x^T P x$ of an arbitrary n-vector x onto the matrix square root Z is uniquely determined, as is the subspace spanned by the columns of Z. For a m-member ensemble, the sample covariance P^a is given by $P^a = SS^T/(m-1)$, where the columns of the $n \times m$ matrix S are mean-zero analysis perturbations about the analysis ensemble mean; the rank of P^a is at most $(m-1)$. A matrix square root of the analysis error covariance matrix is the matrix of scaled analysis perturbation ensemble members $Z = (m-1)^{-1/2} S$.

The covariance matrices of Kalman filter evolve from timestep k to $k+1$ as

$$P_k^f = M_k P_{k-1}^a M_k^T, \tag{1.14}$$

and

$$P_k^a = (I - K_k H_k) P_k^f (I - K_k H_k)^T + K_k R_k K_k^T. \tag{1.15}$$

Using the square root matrices, Eq. 1.14 and 1.15 can be replaced by

$$Z_k^f = M_k Z_{k-1}^a, \tag{1.16}$$

and

$$Z_k^a = (I - K_k H_k) Z_k^f + K_k W_k, \tag{1.17}$$

where W_k is a $p \times m$ matrix whose m columns are identically distributed, mean-zero, Gaussian random vectors of length p with covariance R_k/m.

Kalman SRFs provide a deterministic algorithm for transforming the forecast ensemble into an analysis ensemble with consistent statistics. Eq. 1.15 is rewritten as

$$\begin{aligned} P_k^a = Z_k^a Z_k^{aT} &= [I - P_k^f H_k^T (H_k P_k^f H_k^T + R_k)^{-1} H_k] P_k^f \\ &= Z_k^f [I - Z_k^{fT} H_k^T (H_k Z_k^f Z_k^{fT} H_k^T + R_k)^{-1} H_k Z_k^f] Z_k^{fT} \\ &= Z_k^f (I - V_k D_k^{-1} V_k^T) Z_k^{fT}, \end{aligned} \tag{1.18}$$

where $V_k = (H_k Z_k^f)^T$ and $D_k = V_k^T V_k + R_k$. Then the analysis perturbation ensemble is calculated from

$$Z_k^a = Z_k^f X_k U_k, \tag{1.19}$$

where $X_k X_k^T = (I - V_k D_k^{-1} V_k^T)$ and U^k is an arbitrary $m \times m$ orthogonal matrix.

1.1.2 The Ensemble Adjustment Kalman Filter

In many typical earth science data assimilation applications the state-dimension n and the number of observations p are large, and the method for computing the matrix square root of $(I - V_k D_k^{-1} V_k^T)$ and the updated analysis perturbation ensemble Z_k^a must be chosen accordingly.

Anderson (2001) proposed the Ensemble Adjustment Kalman Filter (EAKF), a variant of the EnKF algorithm. In EAKF the model state is computed through an adjustment matrix so that the posterior covariance satisfies the Kalman gain exactly. Tippett et al. (2003) pointed out that EAKF is a type of ensemble square root filter.

In EAKF, Z_k^a is updated using

$$Z_k^a = A_k Z_k^f, \tag{1.20}$$

and the ensemble adjustment matrix A_k is defined as

$$A_k = F_k G_k \widetilde{C}_k (I + \widetilde{\Gamma}_k)^{-1/2} G_k^{-1} F_k^T, \tag{1.21}$$

where $P_k^f = F_k G_k^2 F_k^T$ is the eigenvalue decomposition of P_k^f and the orthogonal matrix $\widetilde{C}_k$ is chosen such that $\widetilde{C}_k^T G_k F_k^T H_k^T R_k^{-1} H_k F_k G_k \widetilde{C}_k$ is diagonal. Choosing the orthogonal matrix $\widetilde{C}_k$ to be $\widetilde{C}_k = G_k^{-1} F_k^T Z_k^f C_k$ gives that $\widetilde{\Gamma}_k = \Gamma_k$ and that the ensemble adjustment matrix is

$$A_k = Z_k^f C_k (I + \Gamma_k)^{-1/2} G_k^{-1} F_k^T. \tag{1.22}$$

The EAKF analysis is therefore

$$Z_k^a = Z_k^f C_k (I + \Gamma_k)^{-1/2} G_k^{-1} F_k^T Z_k^f. \tag{1.23}$$

1.1.3 The Localisation and Physical Balance Problem in Data Assimilation

With the chaotic nature of Earth's atmosphere, initial conditions must be as close to the truth as possible. At the same time, they must be balanced to prevent the production of gravity waves, which propagate through the model and degrade the forecast. As described earlier, the first numerical weather forecast by L.F. Richardson failed largely due to the spurious waves in his initial conditions (Lynch, 2008).

In the context of variational approaches, Courtier and Talagrand (1990) showed that, because a standard 4DVAR algorithm uses all degrees of freedom of the problem to minimize the cost function, it generates as many gravity waves as needed in order to best fit the observations. Thus, a balanced analysis requires the addition of a balance constraint to the cost function minimization (Neef et al., 2006). Many methods have been applied over the years to handle imbalances that variational data assimilation systems create. For NWP, the geostrophic and hydrostatic balance were prevalent in the global models (e.g. Parrish and Derber, 1992) but as the model resolution keeps increasing the balance breaks down (e.g. Vetra-Carvalho et al., 2012). There have been efforts to maintain the balance in convective scales. For instance, Honda et al. (2006) separated the error into synoptic and mesoscale components, calculating the regression coefficients from forecasts that have had a low-pass filter applied to them. Barker et al. (2004) added an additional term to the calculation of balanced pressure to include cyclostrophic balance.

For the ensemble systems, the data assimilation is usually degenerated by the spurious covariances with distant grid points. This is caused because the ensemble size (order of 100) is usually too small compared with the model dimension (with the typical order of magnitude of 10^8 to 10^9 for the art-of-state NWP systems, for example, the ECMWF IFS system with the T1279L137 resolution since July 2013 (Bocquet and Sakov, 2014)), thus the covariance matrix cannot fully represent the relationship between distant variables. The localisation technique is often used to 'localise' the impact of one observation within a certain distance. The Schur (elementwise) product is often used in the localisation technique (e.g. Hamill et al., 2001; Houtekamer and Mitchell, 2001),

$$(P^f)\prime = P^f \cdot C, \tag{1.24}$$

where the elements in matrix C represent some localisation function f_{loc} of distance d between grid points i and j. In this thesis the Gaspri-Cohn algorithm (Gaspari and Cohn, 1999) is used,

$$f_{loc} = exp[\frac{-d(x,y)^2}{2L^2}], \tag{1.25}$$

where $d(x,y)$ is the distance between the variable x and the observation y and L is the localisation distance used for scaling the effect of the observation.

However, localisation may cause imbalance to the dynamical system (e.g. Greybush et al., 2011; Lorenc, 2003a), although a balanced model error covariance produces a balanced analysis state (Cohn and Parrish, 1991). Lorenc (2003a) pointed out that when a SSH observation at a single point is assimilated without localisation, the increments of the SSH and ocean currents are balanced. If localisation is used, the gradient of the SSH increases while the ocean currents reduce. Therefore spurious ageostrophic waves are created in this process. Fig. 1.1 illustrates such spurious waves. Mitchell et al. (2002) reported that different ensemble size, assimilating frequency or localisation radius can cause imbalance for GCMs. Kepert (2009) suggested using localisation of streamfunction and velocity potential instead of u and v velocities, but this method is not easy to implement for regional ocean models. For the multivariate problem, it is also difficult to specify the relationship among various variables. A common practice is to use linear regression, but this can be a major source of error (Anderson, 2007). To solve this problem, Anderson (2007) proposed to 'localise' the impact of observation to model states (e.g., SST observation at one point and simulated ocean currents at another point), but he also pointed out that it is usually difficult to define the 'distance' between them, especially for high-dimensional GCMs. The imbalance can be reduced by using the balance operators (e.g. Wu et al., 2002) under some assumptions (e.g., the hydrostatic and geostrophic assumptions). In this thesis, we use a multivariate balance operator proposed by Weaver et al. (2005) to solve the imbalance problem. In this algorithm, each model variable is separated into balanced and unbalanced components, and several balance assumptions are made to calculate the increments. This physical constraint has been used in several variational ocean data assimilation systems (e.g. Balmaseda et al., 2013; Li et al., 2008; Moore et al., 2011b).

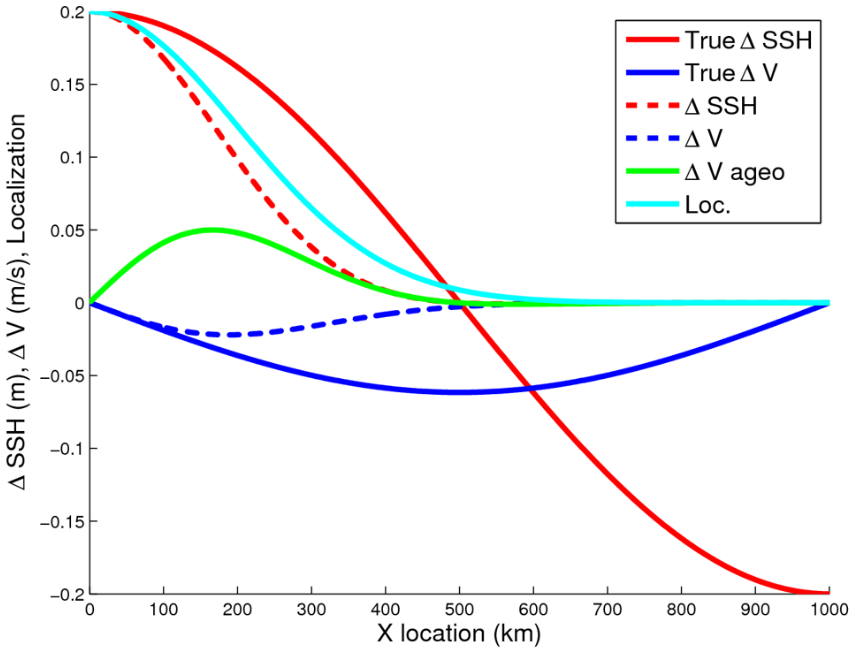

Figure 1.1 Example showing the introduction of imbalance by localisation (after Lorenc (2003a) and Greybush et al. (2011)). Waveforms of SSH (red) and meridional ocean currents (blue) before (solid) and after (dashed) multiplication by a Gaussian localisation function (cyan) (Eq. 1.24). Values on the y axis denote the size of the analysis increment (m; ms^{-1}) from the assimilation of an SSH observation located at the origin. The spurious ageostrophic portion of v after localisation is in green.

The geostrophic balance is a major constraint on large scale motion in the ocean and atmosphere (e.g. Gill, 1982). This is a balance between the pressure and the Coriolis force. The fluid, not initially in equilibrated state, adjusts in a rotating system and this process is called geostrophic adjustment and the balance state is called geostrophic balance.

For most of the ocean and atmosphere problems, as discussed in this thesis, the horizontal scale is much larger than the vertical scale and the hydrostatic assumption can be made. The momentum equation can be simplified as,

$$\begin{aligned} \frac{\partial u}{\partial t} - fv &= -g\frac{\partial \eta}{\partial x}, \\ \frac{\partial v}{\partial t} + fu &= -g\frac{\partial \eta}{\partial y}. \end{aligned} \tag{1.26}$$

where f is the Coriolis parameter, g is the gravitational constant. Therefore when the fluid is in balance, the flow follows the equations

$$\begin{aligned} fu &= -g\frac{\partial \eta}{\partial y}, \\ fv &= g\frac{\partial \eta}{\partial x}, \end{aligned} \tag{1.27}$$

and has the property that the flow is along contours of constant pressure. The time scale of the geostrophic adjustment is just ($1/f$, approximately 10^4 s in this study) (Kuo and Polvani, 1997) thus dynamic models can restore to balance quickly, but the idealised studies (in Chapter 4) shows that the balance in data assimilation procedure improves the forecast.

1.1.4 The Regional Ocean Data Assimilation

The development of ocean data assimilation and prediction systems has lagged behind the NWP for many years, mainly because, until relatively recently, observations of the oceans have been relatively scarce compared to the data-rich atmosphere (Tonani et al., 2015). The development of global and regional ocean data assimilation systems began in the 1990s. In the United States, the Naval Research Laboratory (NRL) implemented a 1/4° global NRL Layered Ocean Model (NLOM) system in 1997 (Dombrowsky et al., 2009). In Europe, the Met Office implemented the Forecasting Ocean Assimilation Model (FOAM) system (Bell et al., 2009) in 1997 (global, 1°), and the French Navy implemented the Système Opérationnel d'Analyse et de Prévision (SOAP) system in 1993 in the Azores current region (12.5 km horizontal resolution), then extended it to the northeastern Atlantic (at 1/10°) in 1998 (Dombrowsky et al., 2009).

The development of operational ocean systems leads to the formation of the Global Ocean Data Assimilation Experiment (GODAE) program in 1997 (succeeded by GODAE-OceanView in 2009, https://www.godae-oceanview.org). There are now over 10 operational global ocean data assimilation and forecast systems within the GODAE-OceanView program (Tonani et al., 2015) but there is still a need for the development of regional systems. The regional systems can be designed to provide detailed information in specific areas of interest. The model parameterisation can be selected and tuned to simulate the characteristic processes of that region including the mesoscale eddies, fronts, air-sea interaction and biogeochemical processes. In addition, the vertical resolution of global models are usually low, which may be unsuitable in the coastal and shelf regions where small-scale processes and coastal dynamics are important and need to be resolved with coastal models.

There are many challenges facing the regional ocean data assimilation systems, including sensitivity of ocean currents to data assimilation parameters and the availability of observation. In the regions of strong currents the choice of data assimilation parameters has a large impact of the assimilation results. As noticed by Stepanov et al. (2012), when assimilating the RAPID data set in the North Atlantic, the use of boundary-focused covariance has the largest impact on data assimilation results, especially on the meridional overturning circulation (MOC) at 26°N with strong adverse impacts on the MOC stream function at higher and lower latitudes. Additionally, better Meridional Overturning Circulation (MOC) values are more sustained when applying open-ocean profiling data assimilation, e.g. from Argo data, along with the RAPID boundary data assimilation. The open-ocean assimilation reduces any negative feedbacks and maintains better open-ocean density distributions, particularly in the sub-polar gyre latitudes, allowing a decoupling of the 26.5°N MOC transports from the water formation processes further north.

There are usually fewer observations available for regional models, especially in the coastal regions. There are several problems for the regional models to using the global monitoring systems. For instance, the resolution of satellite altimetry is sometimes too low to resolve small scale features in coastal regions. Profiling floats (e.g. ARGO) are usually not available in shallow-water regions. There are several studies in the Mediterranean Sea showing that the multi-platform observations (remote-sensing, in-situ observation, gliders, etc.) are able to provide information of mesoscale and sub-mesoscale eddies (Pascual et al., 2013; Tintoré et al., 2013). Recently developed technologies including telemetering moorings and autonomous underwater vehicles (AUVs) could also be helpful in providing the vertical structure which is critical in modelling the density stratification. In this thesis, a regional ocean data assimilation system is developed and applied to the South Australian Sea.

1.1.5 Coupled Data Assimilation and the Forecast of Tropical Cyclones

The Coupled General Circulation Models (CGCMs) have been developed for the atmosphere-ocean interaction study. Studies of the coupled models have shown advantages over uncoupled ones in both climate (e.g. Wang et al., 2005) and weather (e.g. Warner et al., 2010) forecast and have been used operationally (e.g. Saha et al., 2010). Data assimilation for the coupled systems is therefore needed. The coupled data assimilation systems are divided into two categories: weakly-coupled and strongly-coupled. The weakly-coupled data assimilation updates the states of different domains (here, ocean and atmosphere) separately during the assimilation stage and integrates the numerical forecast model to exchange the information. On the other hand, the strong-coupled data assimilation updates the states of both domains together in the assimilation stage through the cross-domain covariance. It has been shown that the strongly-coupled data assimilation is superior, using either variational data assimilation (e.g. Smith et al., 2015) or ensemble approaches (e.g. Sluka et al., 2016). In this thesis a strongly-coupled data assimilation system is developed and used for tropical cyclone (TC) forecast.

A tropical cyclone is a warm-centred low-pressure system which is non-frontal, conceived over warm tropical and sometimes subtropical waters, and characterized by strong vertical convection and a closed low-level wind circulation. It is the near surface maximum sustained wind speed alone which determines the category of a TC. During its life a TC may grow from a tropical depression to a tropical storm or, if it strengthens enough, to a hurricane or typhoon. A TC is called hurricane if it has the near surface maximum sustained wind speed in excess of 33 ms^{-1} over the Atlantic Ocean and the East Pacific Ocean, and typhoon over the Western North Pacific Ocean. The maximum 1-min sustained wind speed is used by the National Hurricane Center (NHC) for the TC definition in the Atlantic Ocean and the East Pacific Ocean, whereas the maximum 10-min sustained wind speed is applied by the Joint Typhoon Warning Center (JTWC) in the Western North Pacific Ocean, North Indian Ocean, and Southern Hemisphere.

Traditionally TCs are considered as an intense yet small feature phenomenon, with little effect on the large scale climate system. However, recent evidence has suggested that hurricanes could play a much more significant role in global climate. TCs mix the warmer surface waters with the cooler subsurface waters, exciting cold wakes that last over a period of weeks (e.g. Wang et al., 2016). The restoration of cold wakes to normal conditions is associated with net, vertically integrated heating of ocean columns, which in statistical equilibrium must be balanced by oceanic heat transport out of the regions affected by the storms (e.g. Emanuel, 2001; Hu and Meehl, 2009; Scoccimarro et al., 2011). The ocean heat transport is largely carried by the meridional overturning circulation (MOC) which is partially driven by the mixing of warmer water into the colder water in depth (Munk and Wunsch, 1998).

TCs affect the populous coastal regions frequently, causing casualties as well as economic and societal losses (e.g. Emanuel, 2005). Both theory and numerical models indicate that the destructiveness of TCs tends to increase in a warming climate (e.g. Emanuel, 2005, 1986, 1987; Jones et al., 2017; Knutson et al., 2010; Mendelsohn et al., 2012; Webster, 2005). Therefore the forecasts of TC intensity and tracks are of great importance. During the past decades the forecast of TC tracks have been improved rapidly but errors in TC intensity forecasts have not been significantly reduced. For instance, the 24-hour Atlantic Hurricane track forecast error at National Hurricane Center (NHC) reduced from 100 n mi (185 km) in 1990 to 36.5 n mi (67 km) in 2016. However, the 24-hour intensity forecast error remained around 10 kt (5.1 m/s) (Cangialosi and Franklin, 2017). Thus many efforts have been made to improve the TC forecast, especially the intensity forecast.

Under favoured atmospheric conditions, the intensification and weakening of TCs are linked to upper ocean properties. The upper oceanic heat content is one of the variables that determine the TC intensity (e.g. Mainelli et al., 2008). In the continental shelf region, the ocean stratification also plays an important role (Seroka et al., 2016). The responses of the upper ocean to TCs have been studied intensively (e.g. Price, 1981, 1983; Price et al., 1994), and the response can be long before the arrival of TC centre. For example, Seroka et al. (2016) and Glenn et al. (2016) reported there was significant ahead-of-eye-centre cooling during Hurricane Irene (2011) in the Mid-Atlantic Bight. Glenn et al. (2016) and Bruneau et al. (2018) also reported significant change of surface ocean currents ahead-of-eye-centre during Hurricane Irene (2011). Therefore both in-situ and remote-sensing ocean observations have been assimilated to improve the forecast of TCs. Sea surface temperature (SST) (e.g. Wada and Kunii, 2017), sea surface height (SSH) and Argo observed subsurface temperature and salinity (Halliwell et al., 2017a), glider observed subsurface temperature and salinity (e.g. Dong et al., 2017) have been assimilated in different systems. Goni et al. (2017) summarised the application of the autonomous and Lagrangian ocean observations used in the Atlantic hurricane forecast.

However, the spatial coverage of subsurface gliders and Argo floats is quite limited, especially in the coastal regions. The satellite observations can be infrequent, impacted by the clouds and of coarse resolution. The use of high-frequency (HF) radar systems in coastal areas has rapidly increased (Paduan and Washburn, 2013). The HF radars remotely measure ocean surface currents by exploiting a Bragg resonant backscatter phenomenon. Electromagnetic waves in the HF band(3–30MHz) have wavelengths that are commensurate with wind-driven gravity waves on the ocean surface; the ocean waves whose wavelengths are exactly half as long as those of the broadcast radio waves are responsible for the resonant backscatter. The HF radar systems are capable of mapping surface currents hourly to ranges approaching 200 km with a horizontal resolution of a few kilometres. The spatial and temporal resolution of HF radars makes them well suited for observing coastal ocean currents. Such observations have been assimilated into ocean circulation models (e.g. Paduan and Washburn, 2013). It has also been shown that HF radars produce reliable observations as tropical cyclones approach (e.g. Glenn et al., 2016; Li et al., 2017). In this thesis the synthetic HF radar observations are assimilated in an idealised case and the forecast skill of tropical cyclones is analysed.

1.2 Thesis Layout

In the following chapters, I first describe the data assimilation package (Data Assimilation Research Testbed, DART), numerical models and data used in this thesis in Chapter 2. A regional ocean data assimilation system for the South Australian Sea is developed in Chapter 3. The system consists of DART and the Regional Ocean Modelling System (ROMS) and satellite observations are assimilated using this system. The physical balance problem in this system is discussed in Chapter 4. A physical balance operator is added to reduce the imbalance and the effect is tested in both an idealised shallow water model and the South Australian Sea system. Chapter 5 applies DART to a ROMS-WRF (the Weather Research and Forecasting atmospheric model) coupled model and the synthetic ocean currents potentially observed by HF radar are assimilated to improve the forecast skills of tropical cyclones.

Chapter 2

Methods and Data

2.1 Methods

2.1.1 Numerical Models

COAWST Coupled Model

The Coupled Ocean–Atmosphere–Wave–Sediment Transport (COAWST, svn 797) Modelling System (Warner et al., 2010) has been used in this study as a platform where the atmosphere model WRF (the Weather Research and Forecasting model) and the ocean model ROMS (the Regional Ocean Modelling System) are set up. COAWST is developed by the Woods Hole Science Coastal and Marine Science Center and is designed to couple several key circulation models to study their interdependence and coupled effects. The component modules within COAWST include WRF, ROMS, the wave model Simulating WAves Nearshore (SWAN) (Booij et al., 1999) and the sediment capabilities of the Community Sediment Transport Model (CSTM) (Warner et al., 2008). In this study, only WRF and ROMS are used. However, COAWST can serve as a suitable platform for fully coupled simulations in the future.

COAWST uses the Spherical Coordinate Remapping Interpolation Package (SCRIP) (Jones, 1998) computed weights to interpolate between different grids used by the different models (Warner et al., 2010). The Model Coupling Toolkit (MCT, Larson et al., 2005) is used to transmit and transform distributed data between the component models within COAWST. MCT is a program written in Fortran90 and works with the MPI (Message Passing Interface) communication protocol. It is compiled as a set of libraries, which are linked during the compilation. During model initialisation each model decomposes its own domain into sections (or segments) that are distributed to processors assigned for that component. Each grid section on each processor is initialised into MCT, and the coupler compiles a global map to determine the distribution of model segments. Each segment also initialises an attribute vector that contains the fields to be exchanged and establishes a router to provide an exchange pathway between model components. During the run phase of the simulation the models will reach a predetermined synchronization point, fill the attribute vectors with data, and use MCT to send and receive commands to exchange fields (Warner et al., 2010, 2008).

ROMS Ocean Model

ROMS is a free-surface, hydrostatic, primitive equations ocean model with a stretched, terrain-following coordinate system (Haidvogel et al., 2008; Shchepetkin and McWilliams, 2005, 2009). Jointly developed by Rutgers University and the University of California at Los Angeles, ROMS has been widely used for a diverse range of applications (e.g. Haidvogel et al., 2000; White and Toumi, 2014; Wilkin et al., 2005). In addition, ROMS is one of the few community ocean models which support 4D-VAR (e.g. Moore et al., 2011a,b,c; Song et al., 2012).

The horizontal equations of motions are shown here in Cartesian coordinates,

$$\begin{aligned}\frac{\partial u}{\partial t}+\overrightarrow{v}\cdot\boldsymbol{\nabla}\boldsymbol{\cdot}u-fv=-\frac{\partial\phi}{\partial x}-\frac{\partial}{\partial z}(\overline{u'w'}-\nu\frac{\partial u}{\partial z})+F_u+D_u,\\ \frac{\partial v}{\partial t}+\overrightarrow{v}\cdot\boldsymbol{\nabla}\boldsymbol{\cdot}v+fu=-\frac{\partial\phi}{\partial y}-\frac{\partial}{\partial z}(\overline{v'w'}-\nu\frac{\partial v}{\partial z})+F_v+D_v,\end{aligned} \tag{2.1}$$

where t is time, (x,y) are the horizontal coordinates, z is the vertical coordinate, (u, v, w) are the (x,y,z) components of vector velocity $\overrightarrow{v}$, f is the Coriolis parameter, ν is the molecular viscosity, ϕ is the dynamic pressure, F_u, F_v are the forcing terms and D_u, D_v are the diffusive terms. The overbar represents a time average and the prime represents a fluctuation about the mean.

The time evolution of the scalar concentration field $C(x,y,z,t)$ (such as the salinity and nutrients) is governed by the advective-diffusive equation,

$$\frac{\partial C}{\partial t}+\overrightarrow{v}\cdot\boldsymbol{\nabla}\boldsymbol{\cdot}C=-\frac{\partial}{\partial z}(\overline{C'w'}-v_\theta\frac{\partial C}{\partial z})+F_C+D_C, \tag{2.2}$$

where v_θ is the molecular viscosity, F_C and D_C are the forcing and diffusive terms.

These equations are closed by parameterising the Reynolds stresses and turbulent tracer fluxes as,

$$\begin{aligned}\overline{u'w'}&=-K_m\frac{\partial u}{\partial z},\\ \overline{v'w'}&=-K_m\frac{\partial v}{\partial z},\\ \overline{C'w'}&=-K_C\frac{\partial C}{\partial z},\end{aligned} \tag{2.3}$$

where K_m and K_C are the mass and scalar concentration vertical eddy viscosities.

The equation of state, which correlates the density regarding the temperature, salinity and pressure is given by,

$$\rho=\rho(T,S,P), \tag{2.4}$$

where T is the potential temperature, S is the salinity and P is the pressure.

In the Boussinesq approximation, the density variations are neglected in the momentum equations except in their contribution to the buoyancy force in the vertical momentum equation. Under the hydrostatic approximation, it is further assumed that the vertical pressure gradient balances the buoyancy force,

$$\frac{\partial \phi}{\partial z} = -\frac{\rho g}{\rho_0}, \tag{2.5}$$

where the dynamic pressure $\phi = (P/\rho_0)$, g is the gravitational acceleration and ρ_0 is the reference density.

Assuming incompressibility, the continuity equation is written as,

$$\frac{\partial u}{\partial x} + \frac{\partial v}{\partial y} + \frac{\partial w}{\partial z} = 0. \tag{2.6}$$

By discretizing the continuity equation using a finite volume approach and integrating vertically, we obtain the free-surface relationship as follows,

$$\eta_{i,j}^{n+1} = \eta_{i,j}^{n} - \frac{\Delta t}{\Delta A_{i,j}}[\overline{U_{i+\frac{1}{2},j}} - \overline{U_{i-\frac{1}{2},j}} + \overline{V_{i,j+\frac{1}{2}}} - \overline{V_{i,j-\frac{1}{2}}}]. \tag{2.7}$$

Where η is the free surface, $\Delta A_{i,j}$ is the horizontal area of the grid box (i,j), $\overline{U}$ and $\overline{V}$ are the barotropic volume fluxes. In a time-splitting, free surface model such as ROMS, the free-surface Equation (Eq. 2.7) and the vertically integrated momentum equations are advanced using a smaller time step compared to the tracer equations. The 3D momentum components (Eq. 2.1) are computed during the baroclinic time step and vertically integrated to provide forcing terms for the barotropic mode. During the barotropic time stepping, the free surface and the barotropic velocities are averaged over the barotropic time steps and fed back into the 3D momentum equations.

Horizontally, the state variables are staggered using an Arakawa C-grid (Fig. 2.1). The free surface, density and tracers are located in the centre of the cells (ρ points).

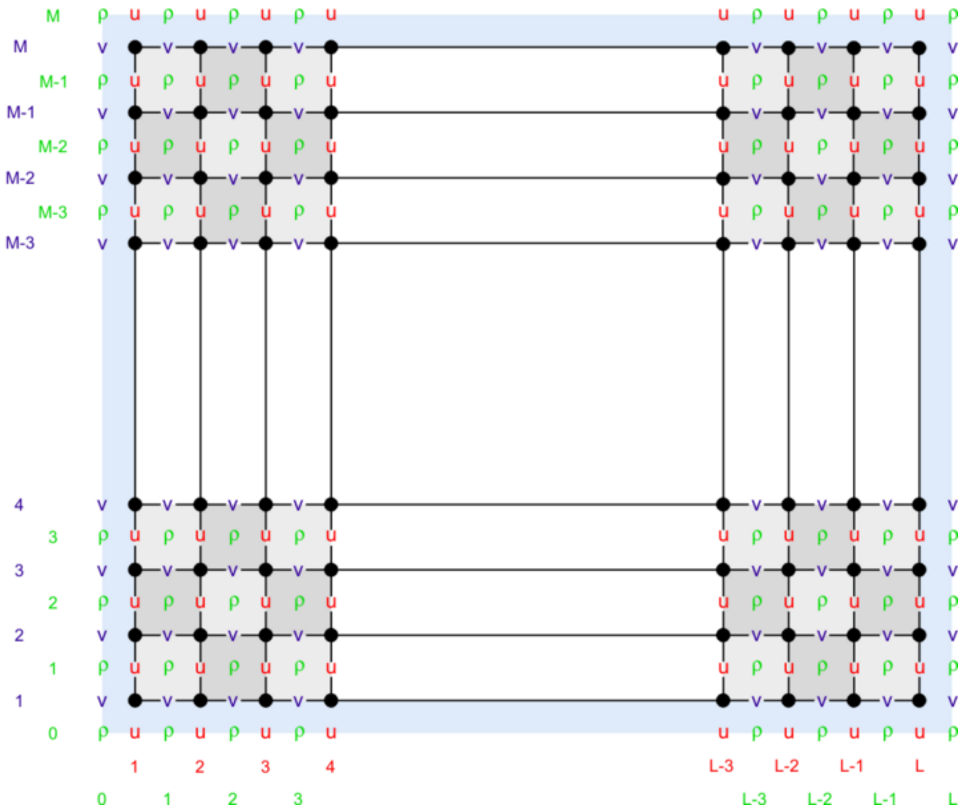

Figure 2.1 Arakawa-C grid staggering of the ROMS grid showing the horizontal velocity points (u and v) and density (ρ). From the ROMS website (https://www.myroms.org/wiki/Numerical_Solution_Technique).

There are 3 tracer types: the active tracers (potential temperature and salinity), the inert tracers (dyes and pollutants) and passive tracers (sediment and biological). The horizontal velocities (u and v) are located at the west-east and north-south cell edges. Overall, the ρ-point quantities are evaluated between the points where currents are evaluated.

In the vertical direction, the governing equations are discretized over the topography using a stretched, terrain-following sigma (σ) coordinate (Fig. 2.2). Hence, each cell may have different thickness (H_Z) and volume. The state variables are staggered vertically such that the density (ρ), horizontal velocities (u and v) and tracers are located at the centre of the grid cell. The vertical velocity (w) is located at the top and bottom faces of the cell.

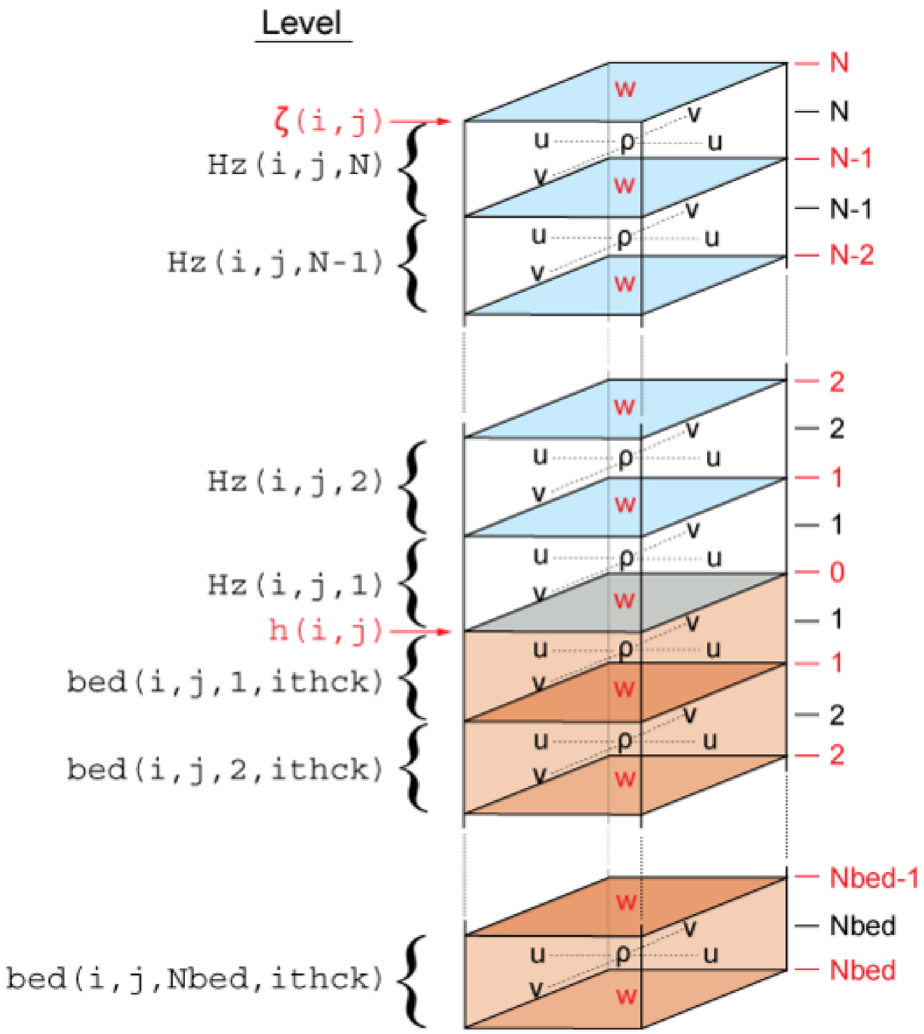

Figure 2.2 Vertical coordinate system of the ROMS grid showing the horizontal velocity points (u and v), vertical velocity points (w) and density points (ρ). From the ROMS website (https://www.myroms.org/wiki/Numerical_Solution_Technique).

In this thesis, the ROMS model is configured as follows. In the South Australian Sea system described in Chapters 3 and 4, the vertical coordinate is set to a minimum depth of 5 m and a maximum depth of 5000 m, with 35 layers. In the coupled system in Chapter 5, the maximum depth is set to 1500 m and the model has 27 vertical layers. The 4th-order centred vertical advection and 3rd-order upstream horizontal advection schemes are used for tracer advection. The horizontal advection of momentum is calculated using a 3rd-order upstream split scheme with the Smagorinsky-like viscosity applied, and the vertical advection of momentum is calculated using a splines scheme. Such configurations have been used in several other studies (e.g. Newinger and Toumi, 2015; White and Toumi, 2014).

WRF Atmosphere Model

The WRF model is a next-generation mesoscale numerical weather prediction (NWP) system designed for both atmospheric research and operational forecasting applications (e.g. Powers et al., 2017). The model is jointly created by the National Center for Atmospheric Research (NCAR), the National Oceanic and Atmospheric Administration (NOAA), the Air Force Weather Agency (AFWA), the Naval Research Laboratory (NRL), the University of Oklahoma, and the Federal Aviation Administration (FAA). The model is developed and supported for both research and operational applications across a range of physical scales from tens of meters to thousands of kilometres. Applications of WRF include real-time forecasting, regional climate modelling, idealised simulations, and data assimilation. WRF is currently in use operationally by NCEP, AFWA, and several other centres.

The WRF system contains two dynamical solvers, referred to as the ARW (Advanced Research WRF) core and the NMM (Nonhydrostatic Mesoscale Model) core. The ARW has been developed in large part and is maintained by NCAR's Mesoscale and Microscale Meteorology Laboratory, while the NMM core was developed by the National Centers for Environmental Prediction and is currently used in their HWRF (Hurricane WRF) system. The ARW-WRF (version 3.7.1) is used in this study. It is fully compressible, Euler nonhydrostatic with a run-time hydrostatic option available. It uses terrain-following, dry hydrostatic-pressure vertical coordinates, with vertical grid stretching permitted. The top of the model is a constant pressure surface. The Arakawa C-grid is used for the grid staggering in the horizontal directions (Fig. 2.3). The coordinating is similar with ROMS, but ROMS has an additional row of V and

ρ points at the start and end of the grid along the x direction and an additional row of U and ρ points at the start and end of the grid along the y direction. Therefore the ROMS grid is larger than WRF with the same domain size and resolution. This is important in the coupled model and the WRF grid has to be at least two grid cells larger than the ROMS grid to ensure that the ocean variables in all the ocean grid cells are provided with a corresponding atmosphere variable.

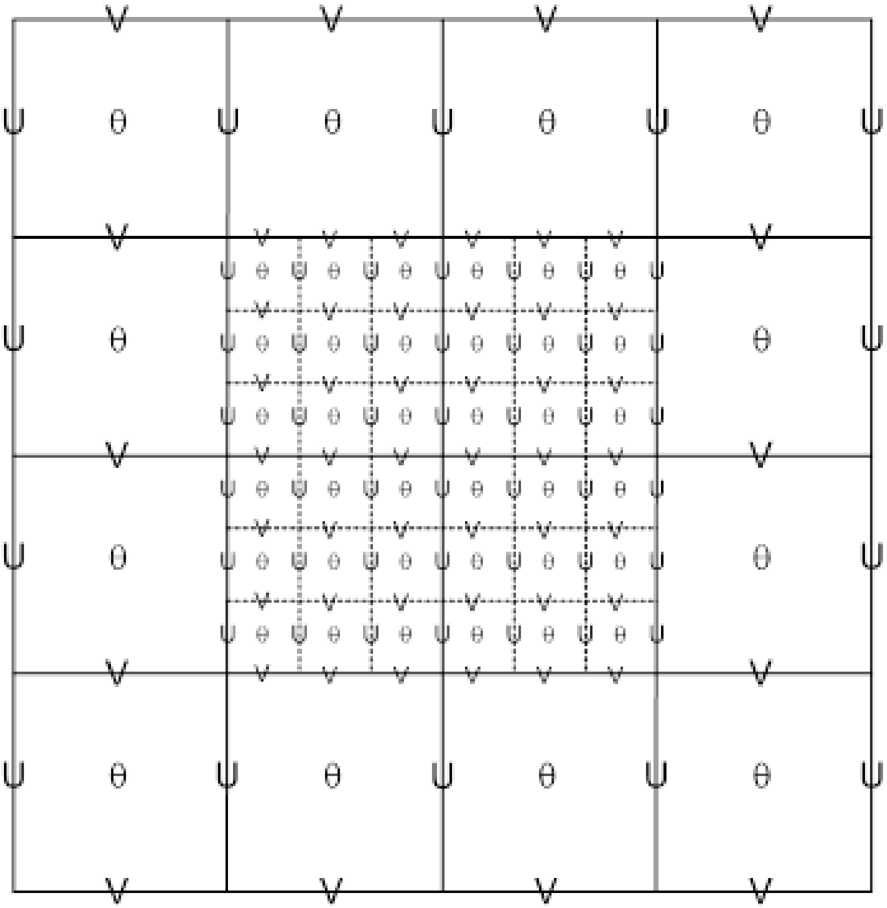

Figure 2.3 Arakawa C-grid staggering in WRF, showing the horizontal velocity points (U and V) and temperature (θ). A portion of a nested grid with 1:3 grid size ratio is shown with the solid lines denoting coarse-grid cell boundaries and the dashed lines denoting fine-grid cell boundaries. Extracted from the WRF technical description (Skamarock et al., 2008).

Several parameterisation configurations are supported by WRF, and the selection is important for the success of the TC simulation. First, a cumulus parameterisation scheme is essential to represent the vertical motions that cannot be resolved at certain horizontal resolutions, (e.g., coarser than 10 km). The microphysics processes in the rainbands are also important for the TC evolution regarding the diabatic heating. The microphysics module in ARW offers several schemes to explicitly resolve water vapour, cloud and precipitation processes. A TC feeds on the moisture and heat supplied by the boundary layer processes, so the surface layer scheme and the planetary boundary scheme are also essential parts of TC simulations. A surface layer scheme is required so that the surface fluxes and friction effect can be simulated. A planetary boundary layer (PBL) scheme is responsible for the turbulence modeling above the surface layer. The radiation schemes determine the radiative heating/cooling processes. Both short-wave and long-wave radiation parameterisations are one-dimensional schemes in the vertical.

The following set-up is used in this thesis (Table 2.1). No cumulus parameterisation scheme is used since the resolution (5 km) is high. The microphysical process are treated with the WRF Single Moment 6-class (WSM6) scheme of microphysical processes (Hong and Lim, 2006). The Rapid Radiative Transfer Model scheme (Mlawer et al., 1997) and Dudhia (1989) scheme are used to estimate the effects of long-wave and short-wave radiation. The Unified Noah Land Surface Model (Tewari et al., 2004) is used to calculate the heat and moisture fluxes over the land. The planetary boundary layer processes are parameterised using the Mellor-Yamada-Janjic scheme (Janjić, 1994) and the surface layer uses an Eta similarity scheme (Monin and Obukhov, 1954). Such combinations have been tested in a series of sensitivity tests and used in several studies (Bruneau et al., 2018; Corsaro and Toumi, 2017; Wang et al., 2015).

Option	Value	Meaning
mp_physics	6	Micro Physics Option (WRF Single–moment 6 scheme)
ra_lw_physics	1	Long-wave Radiation Option (RRTM scheme)
ra_sw_physics	1	Short-wave Radiation Option (Dudhia scheme)
sf_sfclay_physics	2	Surface Layer Option (Eta Similarity Scheme)
sf_surface_physics	2	Land Surface Option (Unified Noah Land Surface Model)
bl_pbl_physics	2	PBL Physics Option (MYJ)
cu_physics	0	Cumulus Parameterization Option (None)

Table 2.1 WRF parameterisation configurations

2.1.2 DART

The data assimilation algorithms provided by the Data Assimilation Research Testbed (DART) are used in all experiments in this thesis. DART is ‘an open-sourced community facility that provides software tools for data assimilation research, development and education’ (Anderson, 2009). DART employs several ensemble based Kalman Filters. It is developed at the National Center of Atmospheric Research (NCAR) and has been used for both ocean and atmosphere problems (e.g Hoteit et al., 2013; Karspeck et al., 2013; Torn and Hakim, 2008).

As described in Chapter 1, the ensemble-based approach is relatively simple to implement, which only requires a prediction model and an observation operator (the H operator). The DART framework is designed ‘so that incorporating new models and new observation types requires minimal coding of a limited set of interface routines, and does not require modification of the existing model code’ (Anderson et al., 2009). In this thesis we use the DART framework to develop the interfaces (*model_to_dart* and *dart_to_model*) between the data assimilation algorithms and ROMS/COAWST. The interfaces are created independently of the ROMS/COAWST model. Other algorithms, including data assimilation, localisation and inflation are provided by DART. The localisation technique, as described in Section 1.1.3, reduces the spurious impact of observations from sampling error caused by the small ensemble size, and inflation ensures the variance of the ensemble is consistent with the estimates derived from the comparison of the forecasts with new data. The configurations of localisation and inflation are described in the following chapters.

The work-flow of the system is illustrated in Fig. 2.4. The whole data assimilation procedure is controlled by a Fortran namelist. At the beginning (top of the figure), the first data assimilation cycle assimilates the observations and the initial ensembles. The *dart_to_model* interface converts the state vector in DART form to ROMS/COAWST form which serves as the initial conditions. Then the model is advanced to the required time. The model outputs are converted to the state vector by the *model_to_dart* interface and the process repeats. When there are no more observations or the control information is met, a set of restart files and a set of diagnostic files are written.

DART has been used for both ocean and atmosphere problems. For instance, Hoteit et al. (2013) developed a regional ocean data assimilation system using DART and the Massachusetts Institute of Technology ocean general circulation model (MITgcm). This system was applied to the Gulf of Mexico with 0.1° resolution and showed a high forecast skill, with estimated ensemble spread mainly concentrated around the front of the loop current. It was also demonstrated that the ensemble assimilation accurately reproduces the observed features without imposing a negative impact on the dynamical balance of the system. Liu et al. (2012) investigated the impact of radio occultation (RO) refractivity observations on the forecast of Hurricane Ernesto's genesis (2006) using WRF and DART and found that assimilating the RO refractivity data in addition to traditional observations leads to a stronger initial vortex of the storm and improved forecasts of the storm's intensification.

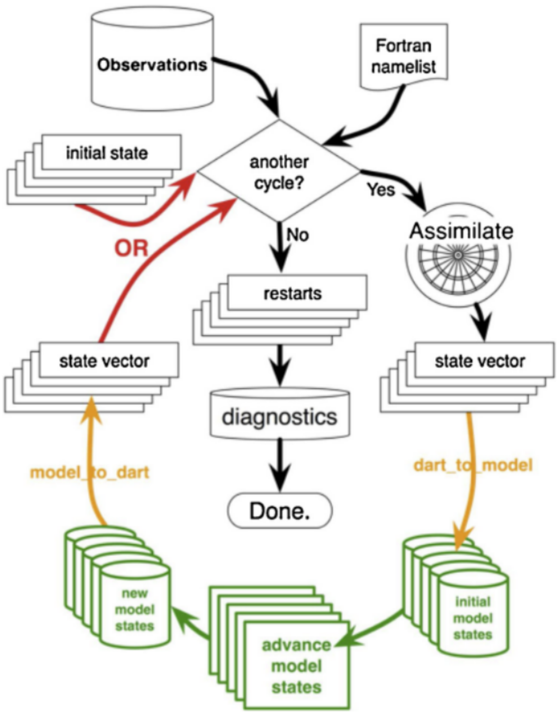

Figure 2.4 A schematic illustration of the DART assimilation system, extracted from Hoteit et al. (2013).

2.2 Data

Both direct and indirect datasets are used in Chapters 3 and 4 for the South Australian Sea system. The along-track satellite observations are assimilated, and gridded products, ocean surface drifters and ARGO floats are used for the evaluation. The along-track sea surface height (SSH) data is provided by AVISO (Archiving, Validation and Interpretation of Satellite Oceanographic data, https://www.aviso.altimetry.fr). AVISO merges observations from different satellites but only Jason-1, Geosat and Envisat were operating during our data assimilation period (01/01/2007 to 01/07/2007). TMI (TRMM Microwave Imager) is one of the 5 instruments carried by TRMM (the Tropical Rainfall Measuring Mission), which launched on 27 November 1997. TMI measures sea surface temperature (SST) in addition to rainfall, sea surface wind speed, column water vapour and cloud liquid water.

The comparison with gridded products, including AVISO 1/4° gridded daily dynamic topography and OISST (Optimum Interpolation Sea Surface Temperature) version 2 daily SST data, illustrates the effects over the whole domain. The OISST data is developed and distributed by the National Oceanic and Atmospheric Administration (NOAA, https://www.ncdc.noaa.gov/oisst), it composites observations from different platforms (satellites, ships, buoys) on a 1/4° global grid and the gaps are filled by interpolation (Reynolds et al., 2007). There are two kinds of daily OISST, AVHRR-Only and AVHRR+AMSR, named after the relevant satellite SST sensors. In this thesis the AVHRR+AMSR data is used. This dataset combines the observations by the Advanced Very High Resolution Radiometer (AVHRR) and Advanced Microwave Scanning Radiometer on the Earth Observing System (AMSR-E). AVHRR has the longest record (from late 1981 to the present) of SST measurements from a single sensor design. AMSR-E data is available from 2002 to 2011. Infrared instruments, like AVHRR, can make observations at relatively high resolution but cannot see through clouds. Microwave instruments like AMSR-E can measure SSTs in most weather conditions (except heavy rain) but not adjacent to land. Thus, in AVHRR+AMSR, observations near land come from AVHRR, while AMSR-E has superior spatial coverage over the open ocean. The combined use of infrared and microwave in cloud-free regions reduces systematic biases due to the independent error characteristics of the two sensors. After AMSR-E lost its full functionality in Oct 2011, AVHRR+AMSR production ended.

Apart from the gridded SSH and SST data products, the gridded and directly observed ocean currents data and the Argo floats data are also used to evaluate the effect of data assimilation. The comparison with the Ocean Surface Current Analysis Real-time (OSCAR; Bonjean and Lagerloef, 2002) currents, illustrates the effects over the whole domain. The OSCAR data provides 1/3° 5-day mean near real-time global ocean currents products of the top 30 m calculated from satellite altimetry and wind fields. Although the more complex physical process is missing, OSCAR provides 'as close to a direct satellite measurement of surface currents on a fixed global grid at regular intervals as possible' (Dohan and Maximenko, 2010). Ocean surface currents from 7 drifters (2791 data points) (http://www.aoml.noaa.gov/phod/dac/gdp_drifter.php; Lumpkin and Pazos, 2007) and subsurface temperature and salinity observed by 8 Argo floats (198 profiles) are also used to provide independent validation. The ARGO floats were located around 120°E, 25.5°S and the drifters were distributed in the south part of the domain (Fig. 3.6).

Chapter 3

The South Australian Sea system

In this chapter, an EnKF based regional ocean data assimilation system has been developed and applied to the South Australian Sea. This system consists of ROMS and the data assimilation algorithms provided by DART. The DART/ROMS system supports a wide range of state of the art ensemble data assimilation algorithms and the assimilation of a wide range of ocean observations. The South Australian Sea system is implemented on a 10 km horizontal grid with 35 vertical layers and all data assimilation experiments are performed over a 6 month period. Sea surface temperature (SST) and sea surface height (SSH) are assimilated separately and together. The results show that the system improves the simulations of both SST and SSH. SSH assimilation also reduces the error of the modelled ocean currents.

3.1 Introduction

The South Australian Sea (31.5°S to 39.5°S, 117°E to 140°E) is studied in this chapter. This region hosts the world's longest zonal, mid-latitude shelf (about 2500km) between Cape Leeuwin and Portland (Middleton and Bye, 2007) and the longest northern boundary current (Fig. 3.1). The Leeuwin Current, flowing southward from the tropics near the west coast of Australia, enters the South Australian Sea around Cape Leeuwin and extends to Tasmania. The coastal currents show strong seasonality (e.g. Middleton and Bye, 2007). In winter, the Leeuwin Current and local winds act to drive eastward currents that average up to 20–30 cm/s. The currents associated with the intense coastal-trapped wave-field (6–12 day band) are of order 25–30 cm/s and can peak at 80–90 cm/s. During summer, the winds lead to weak average coastal currents (<10 cm/s) that flow to the north-west (e.g. Middleton and Bye, 2007, in their Fig. 2).

In addition, this region is of high ecological and economic importance. It has been recognised as one of the 64 Large Marine Ecosystems (LMEs) by NOAA (http://www.lme.noaa.gov/). However, there is huge uncertainty in the estimates of the primary production, which vary from < 100 mg C m^{-2} day^{-1} to > 500 mg C m^{-2} day^{-1}, partially due to the uncertainties in the observation and modelling of ocean currents (e.g., the upwelling of the coastal waters) (van Ruth et al., 2010).

The oil/gas exploration and tourism ventures have been emerging in this area since the late 1960s. There have been recent plans to further explore the Great Australian Bight by a number of companies, including BP/Statoil and Chevron. The proposal to explore in the bight has been the focus of community opposition and modelling commissioned by the Wilderness Society showed that a worst-case scenario leak of oil could have a catastrophic effect on the southern coastline of Australia (Milman, 2015). The simulation and predictability of the ocean circulation, temperature and other oceanic variables are therefore important.

While global systems provide analyses and prediction for this region, regional systems are still in need for higher resolution forecast, assimilation of particular observations and emergency alerts (e.g. Hoteit et al., 2013; Phillipson and Toumi, 2017). Such a system based on the Ensemble Kalman Filter (EnKF) algorithm is developed in this chapter. Here we present the first implementation of DART (Anderson et al., 2009) to ROMS, to provide several state-of-the-art algorithms with localisation, inflation techniques. Another advantage of this regional system over the global DA systems

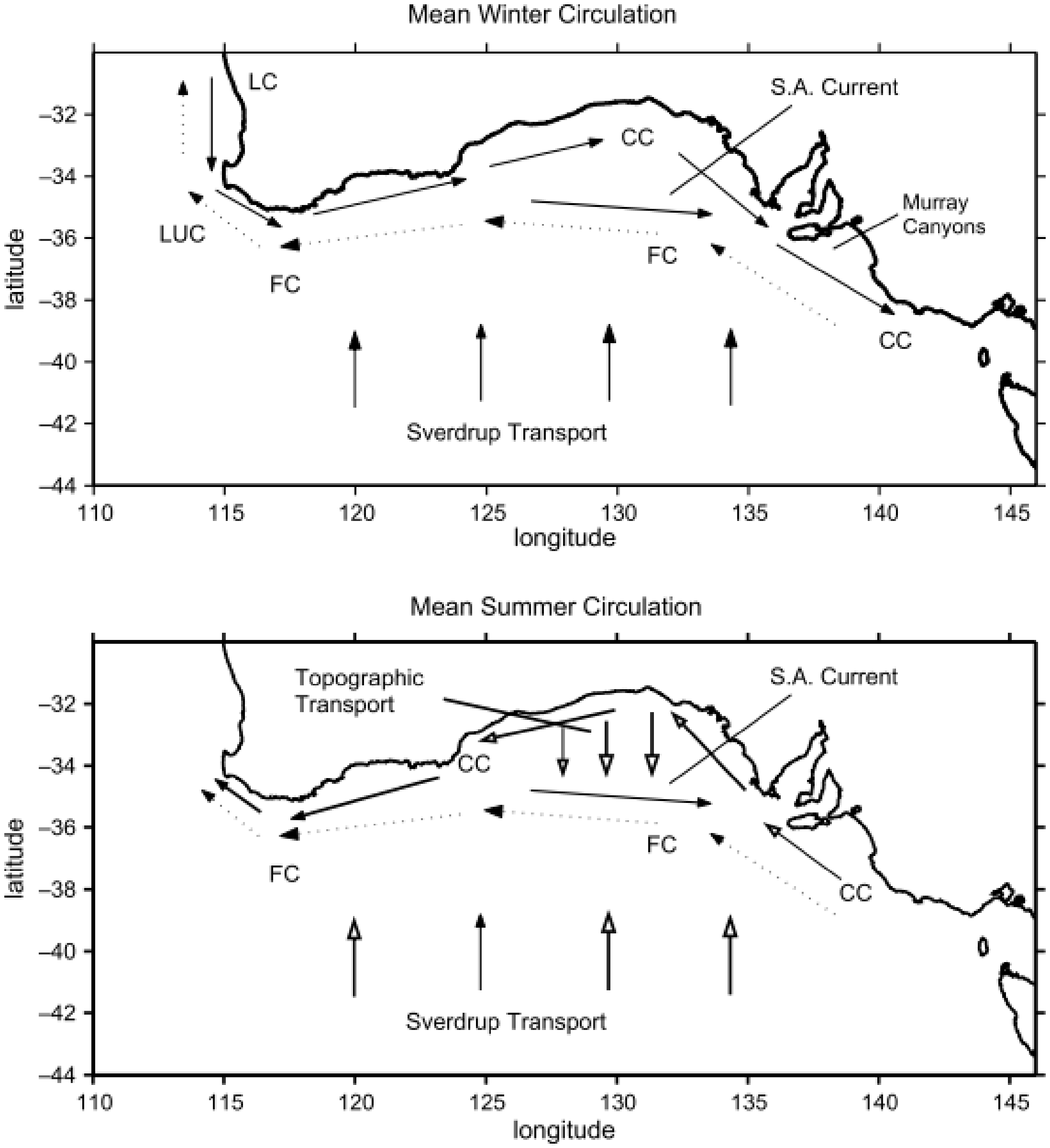

Figure 3.1 Upper panel: A schematic of some key circulation features for winter, including the Leeuwin Current (LC), Leeuwin Undercurrent (LUC), Flinders Current (FC) and shelf-edge South Australian Current (SA Current). Water is downwelled throughout and as a dense salty outflow from the Gulfs. Lower panel: Summertime circulation and upwelling occurs off Kangaroo Island and the Bonney Coast. Shelf-edge downwelling may occur in the western Bight. From Middleton and Bye (2007).

available (e.g., the Copernicus MyOcean dataset (http://www.copernicus.eu/projects/

myocean), the U.S. navy HYCOM dataset (https://hycom.org/)) is that the tidal currents are simulated in this study.

The following sections describe the implementation of data assimilation algorithm in the regional ocean model, the results of the climatology run and the DA experiments, and the discussion.

3.2 Methods

3.2.1 The Configurations of DART

In this study, the data assimilation algorithms provided by DART are used, including the EAKF, the localisation and the inflation techniques. A major challenge for ensemble methods with small ensemble size is the spurious long-distance correlations (Houtekamer and Mitchell, 1998). The localisation technique is usually used to suppress the influence of distant observations (e.g. Mitchell et al., 2002). The optimum choice of the localisation scale depends on several factors, such as the sampling correlation (e.g. Emerick and Reynolds, 2011). The Gaspari-Cohn localisation algorithm (Eq. 1.24) (Gaspari and Cohn, 1999) is used here, as recommended by DART. The localisation radius halfwidth is set to 0.03 arc in the ROMS case, which is about 110 km in the region. This value is selected after comparing a series of assimilation experiments (details are shown in the following section) with different localisation configurations (0.02 arc, 0.03 arc, 0.04 arc and 0.05 arc). Generally, a larger scale produces a better result for SSH while a smaller one produces better SST. The results with the scale of 0.03 arc are overall the best for both variables.

Assimilation of each observation adds information to the dynamic system and thus the spread of the ensemble decreases. This reduction of ensemble spread could be problematic due to the model and observation error and bias. The problem is addressed in DART by inflating the spread periodically (Anderson and Anderson, 1999). For an ensemble with N members and the model size is M, the model forecast ensemble is adjusted by,

$$x_{m,n}^{inf} = \sqrt{\lambda}(x_{m,n} - \overline{x_m}) + \overline{x_m}, m = 1, 2, \ldots, M; n = 1, 2, \ldots, N. \tag{3.1}$$

λ is called the inflation factor. Studies have shown that the inflation could improve the performance of the regional ocean data assimilation systems (e.g. Hoteit et al., 2013). A more favourable method is to vary the inflation spatially and temporally, instead of using a fixed number. DART employs a hierarchical Bayesian filter (HBF) adaptive inflation algorithm (Anderson and Collins, 2007) to produce varying inflation. The inflation factor, λ, is viewed as a one-dimensional state vector for this model of variance error, and observations in conjunction with Bayes theorem can be used to improve the estimate of λ. If the observation is further from the ensemble mean than expected, HBF uses more inflation and vice versa. In this chapter, we use the adaptive inflation for the prior state and the inflation is assigned with initial value of 1.02, the lowerbound of 1.0, the inflation damping of 0.9 and evolves with the standard deviation of 0.6. In most of the experiments, the actual inflation coefficient is 1 to 6, which is a reasonable value.

The initial state ensemble is essential for the success of data assimilation as it provides information about the variability and uncertainty of the system. An appropriate initial ensemble should include 'information about the main physical quantities that govern the evolution of the state' thus it could speed up convergence toward the 'true' ocean state (Hoteit et al., 2008). Following Hoteit et al. (2013), a second-order sampling scheme (Pham, 2001) is used to generate the initial ensemble. Firstly, we create a set of model states using the results of the control run (in this study, a 7 year control run, as described in the following section) in winter since the South Australian Sea is dominated by strong seasonality (Middleton and Bye, 2007). Secondly, an Empirical Orthogonal Function (EOF) analysis is applied to extract the dominant variability from this long model trajectory. Then the initial states are generated using the following equation,

$$x_0^i = \bar{x} + \sqrt{N} L_0 \omega_i^T, \tag{3.2}$$

where N is the ensemble size, L_0 is the matrix whose $N-1$ columns are the EOFs, $\bar{x}$ is the mean of the long-term trajectory and ω_i is the ith row of a $N \times (N-1)$ random orthogonal matrix Ω with zero column sums. The ensemble size is determined according to the limitation of computation resource and model variance, in this study the ensemble size is 50. This ensemble size is selected after a set of sensitivity tests (details are shown in the following section) and the size of 50 performs similarly with 100 while the computational cost is significantly lower. The ensemble members are thus generated with mean $\bar{x}$ and covariance matrix $L_0 L_0^T$ which is an optimum approximation of the original states (Hoteit et al., 2013). The ensemble is then used to initialise DART.

3.2.2 Experiment Design

The ROMS model is implemented in the South Australian Sea on a 10 km horizontal grid with 35 vertical layers. The model domain extends from 39.5°S to 31.5°S and 117°E to 140°E. The bathymetry (Fig. 3.2) is obtained from the Scripps Institute of Oceanography global seafloor topography (Smith, 1997). Tidal sea level and horizontal velocity are extracted from Oregon State University TPXO7.2 global inverse tidal model at 1/12° resolution (http://volkov.oce.orst.edu/tides/global.html). The initial and lateral boundary conditions for temperature, salinity, three-dimensional velocity fields, and non-tidal sea level are obtained from the daily mean, 1/12° HYCOM re-analysis (Metzger et al., 2014). The model is forced with the 6-hourly re-analysis atmospheric state from the National Centers for Environmental Prediction (NCEP) Climate Forecast System Re-analysis (CFSR) project (Saha et al., 2010). The atmospheric forcing variables include downward longwave radiation, downward shortwave radiation, sea level pressure, 2m specific humidity, 2 m air temperature, 10 m winds, and total precipitation. Climatological river discharge is obtained from RivDIS database (Vorosmarty et al., 1998) provided by KNMI (http://climexp.knmi.nl/) to calculate the flow rate of the major river (River Murray) in this region.

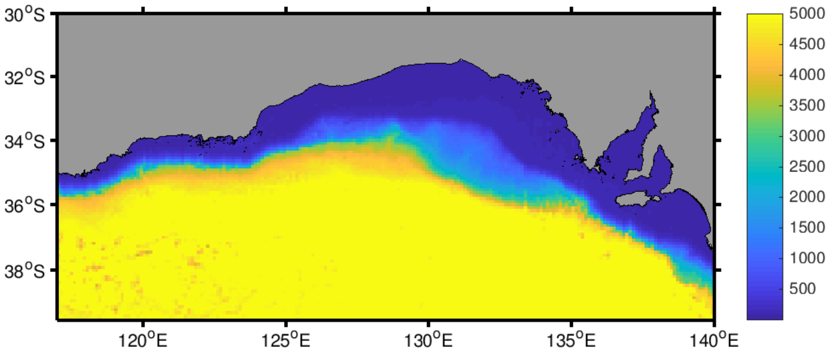

Figure 3.2 The bathymetry used in the South Australian Sea system. The units are m below the sea surface. The bathymetry is set to a minimum depth of 5 m below the sea surface and a maximum depth of 5000 m.

The control simulation runs for 8 years from 2005 to 2012. The first year is discarded as the spin-up period. The data assimilation simulations all run from January 1^{st}, 2007 to July 1^{st} 2007. In the data assimilation experiments, the AVISO along-track sea surface height (SSH) anomalies (http://www.aviso.altimetry.fr/en/home.html) and TMI along-track sea surface temperature (SST) dataset (http://www.remss.com/missions/tmi) are assimilated every five days. Here all observations within ± 2.5 days of the assimilation time are binned as if they were available at the middle of this assimilation window. This window length is similar with previous studies (e.g. Hoteit et al., 2013; Oke et al., 2013). The main variability from the 30 year CFSR data for each month are extracted using EOF analysis and the atmospheric forcing for each of the ensemble members is created in a similar way as the initial ensembles,

$$x^i = x + 0.2 * \sqrt{N} L_0 \omega_i^T, \tag{3.3}$$

where x is the forcing variables (wind field and radiation in this thesis), L_0 is the EOF matrix of the 30 year (1981-2010) data during the appropriate month of the forcing, and ω_i is the ith row of a random matrix Ω as described in Eq. 3.2. Thus the forcing for each ensemble member is different, and the error of CFSR is assumed to be 20%. The open boundary forcing is from HYCOM analysis and unvaried.

Three data assimilation experiments are carried out to assimilate satellite observed along-track SST and SSH data, separately and together. The setup of all experiments is summarised in Table 3.1. The gridded SSH and SST data and OSCAR surface currents data are used for the model comparison. In the experiments, the assimilated data is pre-processed. Following Moore et al. (2011c), the AVISO data is processed before being assimilated by adding the observed sea level anomalies to the difference between the detided ROMS mean SSH and AVISO dynamic topography for 2006-2012 to remove the offset between the model SSH and AVISO dynamic topography. Because the AVISO SSH data is de-tided, we use the FES2012 tidal model (Lyard et al., 2006) to add the tidal signal to the original AVISO SSH. The water levels simulated by ROMS and FES2012 model are similar in most of the domain, but in regions where the ocean is shallow and bathymetry is complicated, they are different. It has been shown that the satellite observed SST data in the coastal regions are usually not reliable (e.g. Hoteit et al., 2013; Smit et al., 2013) therefore the SST and SSH data within 100 km distance to the coastline is discarded. As for the model evaluation, the AVISO gridded data is processed similarly to the along track data to ensure the spatiotemporal mean of AVISO and model SSH are equal.

Experiment	Assimilated Variables
ExpA (control run)	None
ExpB	SSH
ExpC	SST
ExpD	SSH and SST

Table 3.1 Experiment design for the South Australian Sea data assimilation system

3.3 The Climatology Run

Before conducting any DA experiment for the real case, a model capable of producing reasonable climatology is required. Here we compare the modelled SST and sea level anomalies (SLA) with satellite product and currents with observed climatology. A comparison between simulated daily SLA standard deviation from the 7-year control run with AVISO gridded SSH anomalies dataset is shown in Fig. 3.3. It is clear that the model variability is generally higher than AVISO observation, especially in the south central part. However, the model is able to capture the main feature of the SSH pattern, especially the higher variability in the coastal region as well as the high variability invading from the western boundary.

EOF analyses are carried out to extract the main variability of SLA. The first 2 EOFs of the original SLA (figure not shown) in ROMS and AVISO are similar. The first EOF is the strong seasonal cycle along the coast and it explains over 85% of the variability. The second EOF is the seasonal cycle in the deep ocean region, especially in the west part of the domain. In AVISO it explains about 3% of the variability while in ROMS the variability is 2%. The first 2 EOFs of the deseasonalised SLA from ROMS and AVISO are also similar(Fig. 3.4 and 3.5). The deseasonalised data is calculated by extracting the daily mean of the 7-year data. The first EOF represents an annual cycle overlapped on a low-frequency oscillation near the coastline and it explains 39% and 50% of the variability in AVISO and ROMS, respectively. ROMS shows a

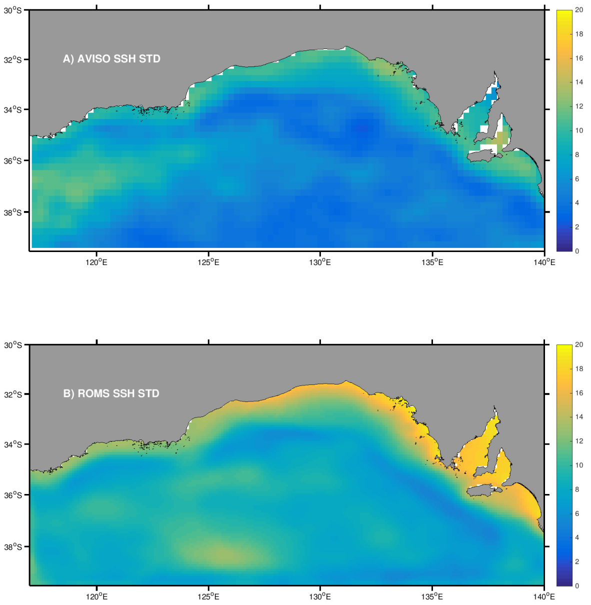

Figure 3.3 Spatial distributions of the standard deviation of daily sea level anomaly (SLA) from A) AVISO observation and B) ROMS control run between 2006 and 2012. The units are cm.

similar spatiotemporal pattern with AVISO. The second EOF of AVISO represents the meso-scale eddy events in the west of the domain while for ROMS this feature is located in the middle of the domain. The frequency of the second EOF is also annual and it explains 15% and 31% of the variability in AVISO and ROMS, respectively. The model reproduces the seasonal cycle and low-frequency feature, but the eddy activity is not captured well.

Fig. 3.6 displays the comparison between the simulated SST and the OISST dataset. The OISST data for the period 2006-2011 is AVHRR+AMSR while for the year 2012 it is AVHRR-only since AMSR-E satellite lost its function in October 2011. Both the mean and the variability of the model results and observation are in good agreement. The model reproduces the warm pattern with little variability along the coast, which is a main feature of the north boundary currents in this region (e.g. Middleton and Bye, 2007). The model also captures the high variability in the shallow water region

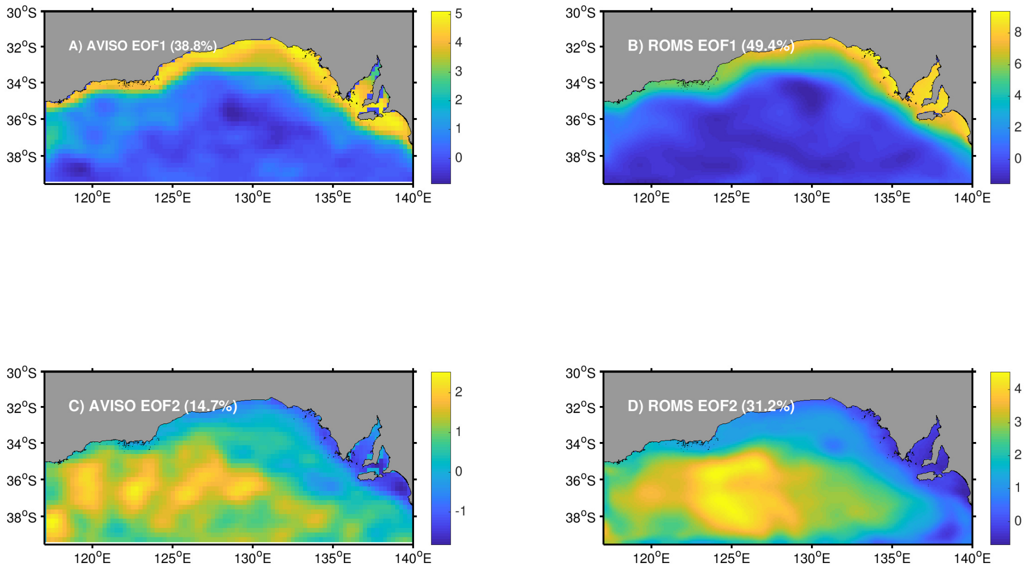

Figure 3.4 Spatial distributions of the first 2 EOFs of deseasonalised (left panel) AVISO daily SLA data and (right panel) ROMS simulated SLA between 2006 and 2012.

of the Spencer Gulf and the Gulf St Vincent. However, the model variability in the central western part is greater than OISST, indicating a stronger meandering of the north boundary currents than observed.

The ocean circulation is also well reproduced (Fig. 3.7). The surface ocean currents are mainly driven by the wind forcing. In the summer, the coastal current flows westward in the Great Australian Bight. On the other hand, in the winter, this region is dominated by the stronger westerly wind which drives the north boundary currents eastward, and the currents are much stronger than in summer. In the 7 year mean of simulated surface currents, both strong eastward boundary currents in the winter and weak westward currents in the summer are reproduced, as seen in the observed climatology (e.g. Middleton and Bye, 2007, in their Fig. 2). The problem is that, in the simulation, the Leeuwin Current is too strong, especially in the summer.

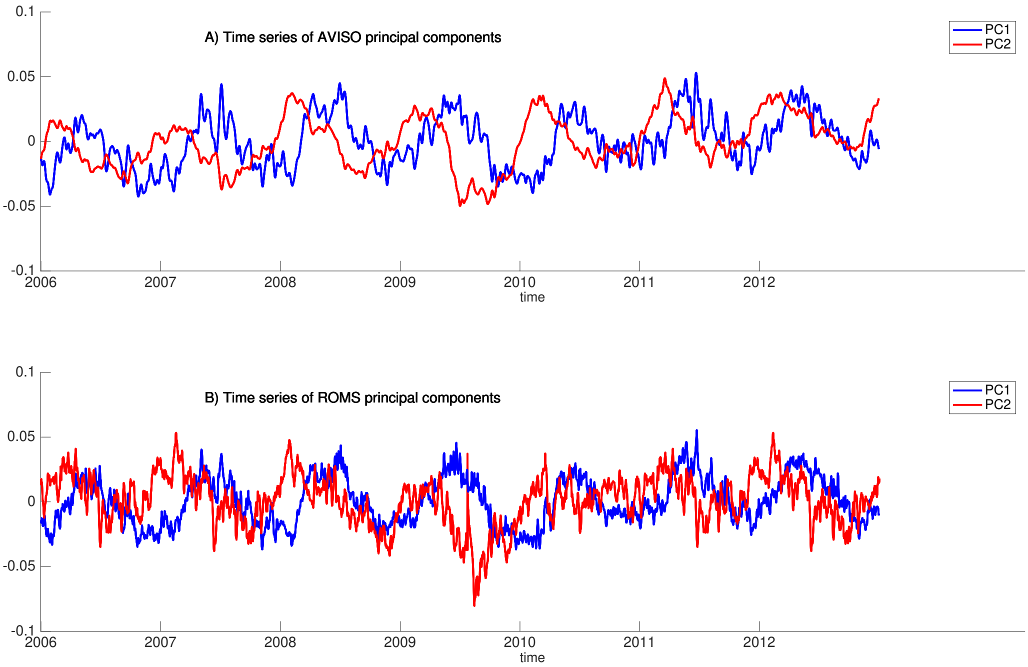

Figure 3.5 Domain average of the first 2 principal components of deseasonalised (A) AVISO daily SLA data and (B) ROMS simulated SLA during the period between 2006 and 2012.

3.4 The DA Experiments

In this section, we first select the optimal combination of filter parameters through a series of sensitivity experiments and then a set of 6-month data assimilation tests is carried out.

3.4.1 Sensitivity Tests

As described above, an EnKF assimilation system is sensitive to a set of filter parameters. Here the sensitivity of the South Australian system is studied by integrating the system with different localisation scales and ensemble sizes for 2 months. The inflation factor is also important but we use the adaptive inflation scheme thus the factor is computed adaptively by DART and not tested. In these sensitivity tests, the along-track SST

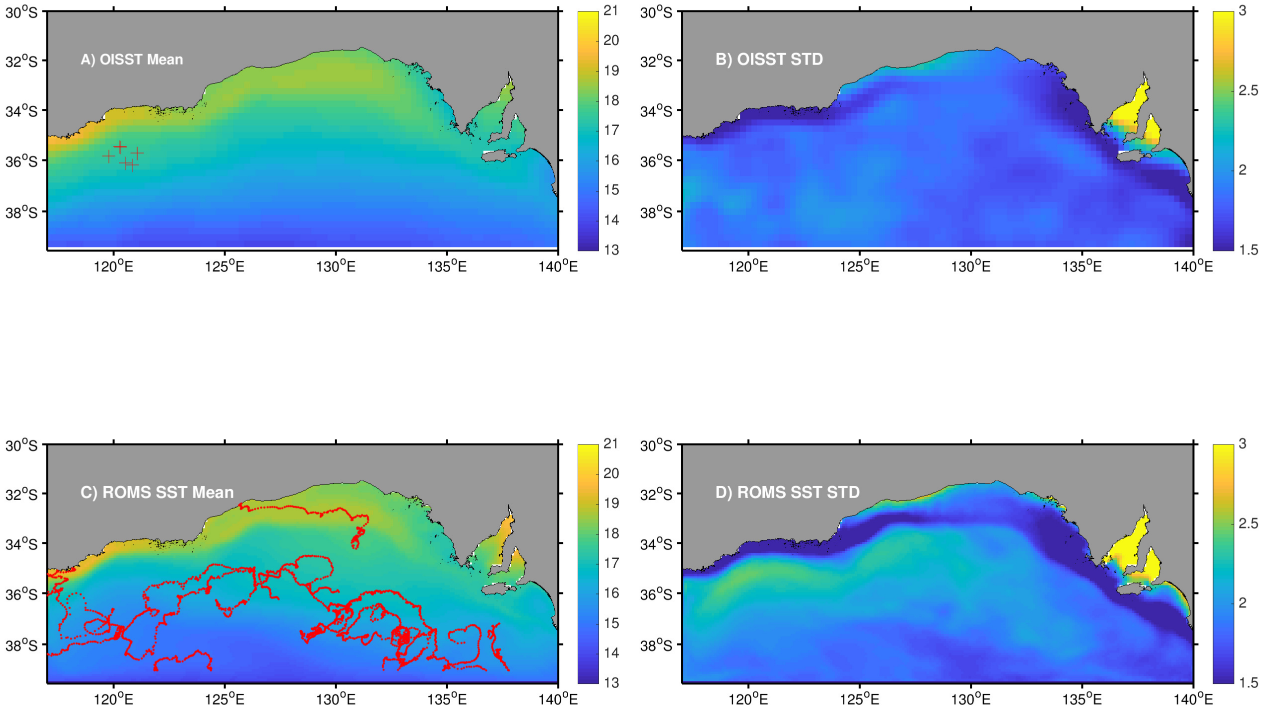

Figure 3.6 Spatial distributions of ROMS simulated daily SST mean and standard deviation compared to OISST observation during the period between 2006 and 2012. The units are °C. The crosses and dots in A) and C) represent the locations of ARGO floats and drifters (used in Chapter 4).

and SSH are assimilated separately and the results are compared with respect to the gridded data.

Sensitivity to Ensemble Size

Large ensemble sizes are always favoured by the assimilation systems, which represent the mean and spread of the prior distribution more accurately. For instance, Miyoshi et al. (2014) used a 10240-member (2 orders of magnitude greater than the typical ensemble size) EnKF system with an atmospheric general circulation model (AGCM) of

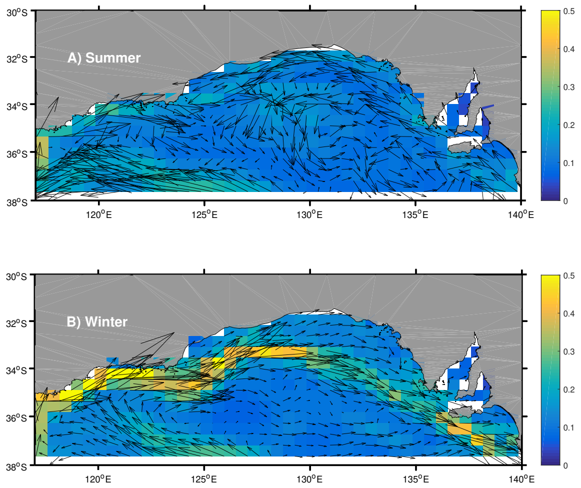

Figure 3.7 Spatial distributions of ROMS simulated mean surface currents for the A) summer and B) winter during the period between 2006 and 2012. The shading indicates the speed (the units are m/s).

intermediate complexity and showed that the large ensemble size benefits the analysis by reducing the spurious long-range correlations. In addition, the experiments were carried out on the Japanese 10 petaflops 'K' supercomputer which ranked number one in the TOP500 list in June and November 2011. However, when the filter is implemented with more complex general circulation models (GCMs), such as ROMS, on a less powerful computer, a large ensemble is computationally too expensive and a limited number of ensemble members is therefore inevitable.

Here we examine the sensitivity of this system by testing 3 ensemble sizes (30, 50 and 100), with the localisation radius of 0.03 arc. The initial conditions and atmospheric forcings for each experiment are generated using Eq. 3.2 and Eq. 3.3. It is evident, as expected, increasing the ensemble size decreases the root mean square errors (RMSEs) of SSH and SST (Fig. 3.8). The size of 50 and 100 are obviously superior to 30, but the improvement of 100 over 50 is marginal although it almost doubles the computational time and cost. Therefore the ensemble size of 50 is selected to get a balance between an optimum performance and the computing efficiency.

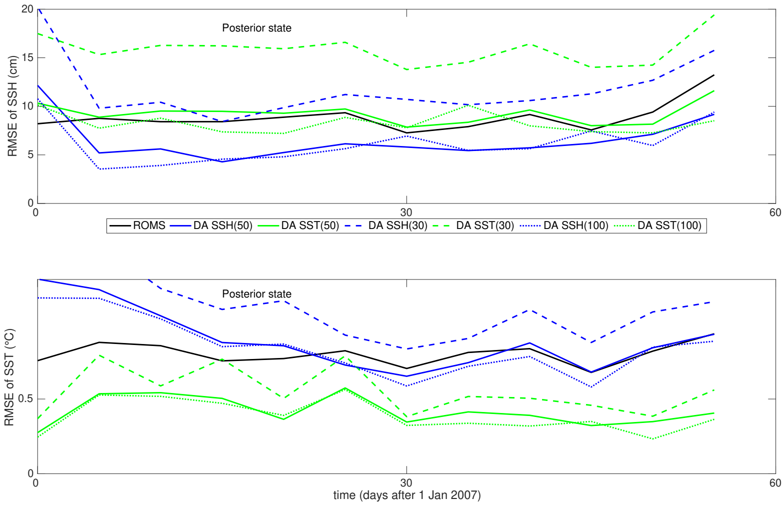

Figure 3.8 Temporal evolution of RMSEs of SSH (top) and SST (bottom) for the posterior state (i.e., the analysis) during the period from 01/01/2007 to 01/03/2007, with different ensemble sizes. The units are cm and °C, repectively.

Sensitivity to Localisation Scale

As described above, localisation is required in an ensemble system with a limited ensemble size. Studies have shown that the performance of localisation is affected by several parameters, such as the location (latitude) of the region in study (e.g. Hacker and Lei, 2015), the ensemble size (Houtekamer and Mitchell, 2001; Miyoshi et al., 2014) and the scale of the phenomenon in study (Buehner and Shlyaeva, 2015). However, the selection of localisation radius is not still well understood and can only be obtained via sensitivity tests.

Here 4 localisation configurations (0.02 arc, 0.03 arc, 0.04 arc and 0.05 arc) are compared to select an optimal scale. As in all the other experiments, an ensemble size of 50 is used in the sensitivity tests. The RMSEs (Fig. 3.9) suggest that the system is sensitive to the localisation scales, but the effects on SSH and SST are different. Generally, the error of SSH decreases as the localisation increases, while a smaller localisation radius produces a better SST analysis. The reason is that, the SSH observations are much more sparse and infrequent than the SST, larger localisation

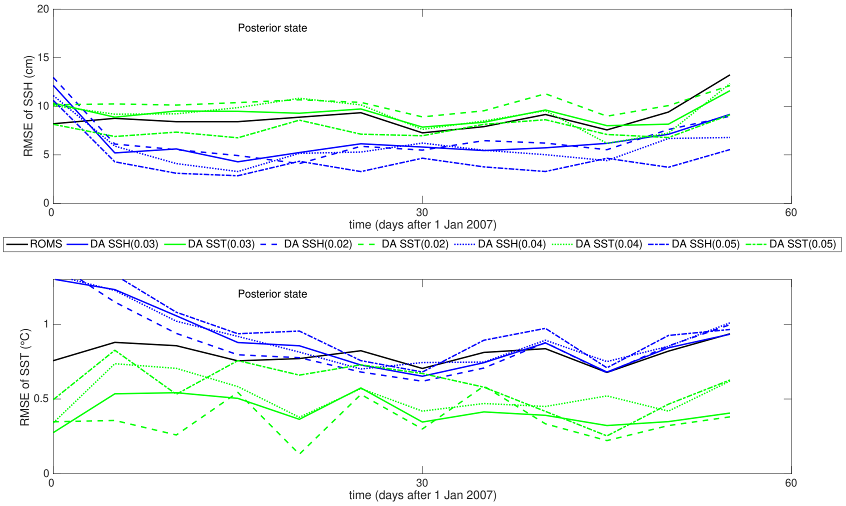

Figure 3.9 Temporal evolution of RMSE of SSH (top) and SST (bottom) for the posterior state (i.e., the analysis) during the period from 01/01/2007 to 01/03/2007, with different localisation scales. The units are °C.

radius makes use of the observations more and smooths the analysis. A potential problem is that the gridded AVISO SSH data is interpolated and smoothed thus the comparison could be unfair. Other studies (e.g. Hoteit et al., 2013) indicate that larger radius degrades the analysis but favours the forecast. In the following experiments, the localisation radius of 0.03 arc (about 110 km in this region) is selected, to get an optimal overall performance of SST and SSH. This is also similar with the results of Hoteit et al. (2013), who used 125 km in the Gulf of Mexico.

3.4.2 The Analysis and 5-day Forecast

The along-track SST and SSH are assimilated in these experiments, together and separately, with the ensemble size of 50, the localisation radius of 0.03 arc and the spatially adaptive inflation factor. We validate the performance of data assimilation by comparing the domain-averaged and time-averaged RMSEs of SST and SSH for different experiments. The results suggest that assimilating SST and SSH improves these two variables, and assimilating SSH also produces better ocean surface currents.

However, unlike in some other studies (e.g. Hoteit et al., 2013; Kurapov et al., 2011), SSH assimilation does not generate a more accurate SST distribution. When both SST and SSH are assimilated at the same time, the correction to both SST and SSH field is very similar to that of the SST assimilation only.

Sea Surface Temperature

The error of surface and subsurface temperature is calculated against the OISST dataset and Argo observations. Compared to the control run (ExpA), assimilating SST alone (ExpC) reduces the SST error by 58% from 0.86°C to 0.36°C (Fig. 3.10(A)) and Table 3.2). The 5-day forecast (prior state) is also much better (RMSE = 0.55°C) than the control run (Fig. 3.10(B)). The improvements are consistent throughout the 6-month period.

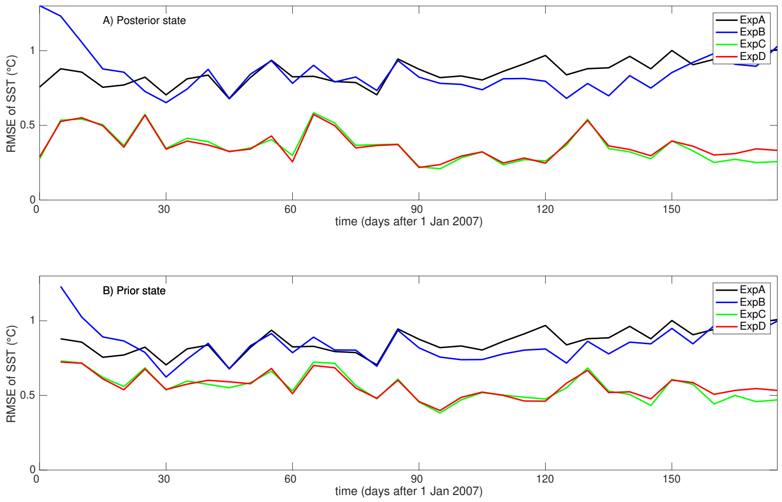

Figure 3.10 Temporal evolution of RMSE of SST for A) posterior state (i.e., the analysis) and B) prior state (i.e., the 5-day forecast) during the period from 01/01/2007 to 01/07/2007. The units are °C.

The difference of the RMSE between assimilating SST with (ExpD) and without SSH is marginal (RMSE for the posterior state is 0.37°C), and the RMSE is quite similar to the control run when only SSH is assimilated (ExpB), indicating that the process of

	ExpA	ExpB	ExpC	ExpD
SSH	8.87	6.57	9.55	7.98
SST	0.86	0.85	0.36	0.37

Table 3.2 The averaged RMSE of SSH and SST from the posterior states compared with the gridded AVISO and OISST data during the period from 01/01/2007 to 01/07/2007. The units are cm and °C respectively.

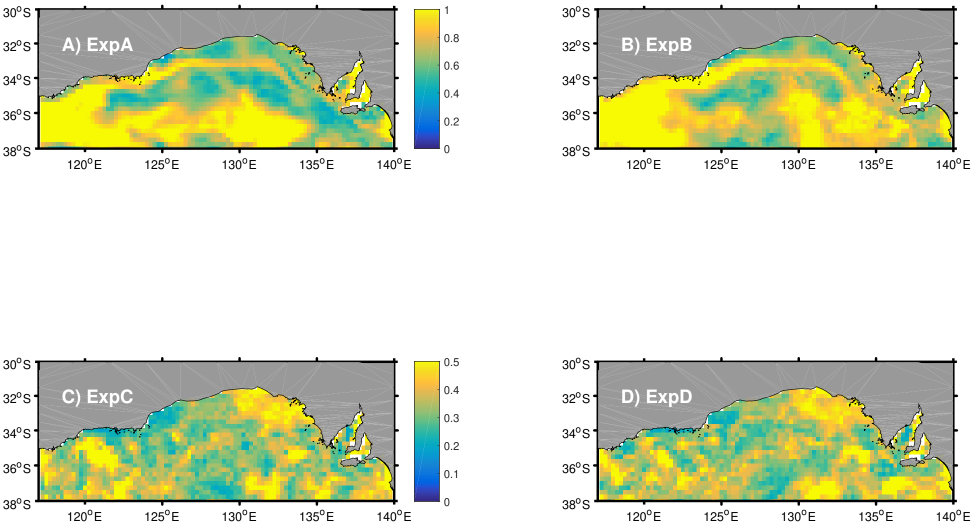

Figure 3.11 Spatial distributions of RMSE of SST for the posterior state (i.e., the analysis) during the period from 01/01/2007 to 01/07/2007, the units are °C. Note: the color scales are different.

SST adjustment is mainly determined by the assimilation of SST. The SST observations are more numerous (˜3200/day) and have a bigger and more regular spatial coverage than the SSH observations (˜400/day). This effect could be studied by conducting OSSEs (Observing System Simulated Experiments) in which the observation density and frequency could be modified. However, a finer tuning of SSH/SST combination may improve the results.

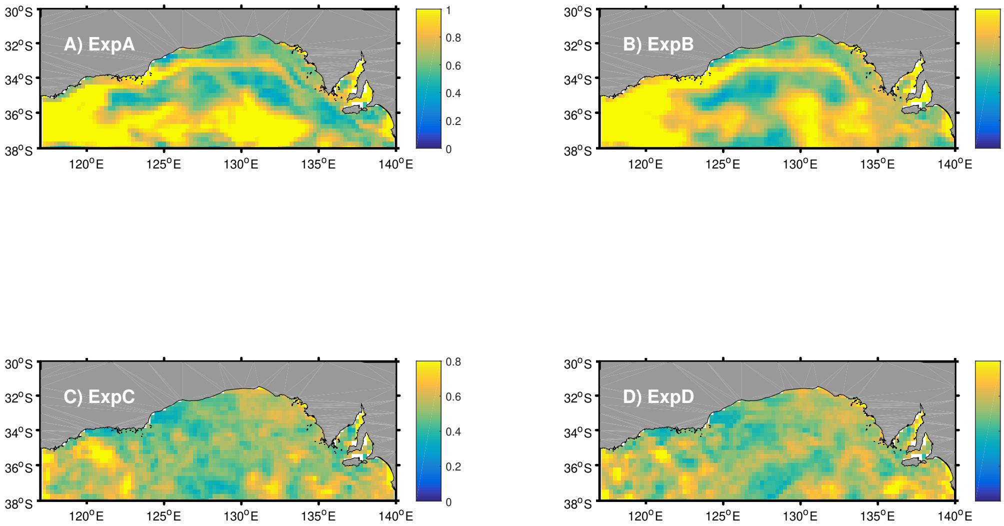

Figure 3.12 Spatial distributions of RMSE of SST for the prior state (i.e., the 5-day forecast) during the period from 01/01/2007 to 01/07/2007, the units are °C. Note: the color scales are different.

The spatial pattern of SST error in these experiments are shown in Fig. 3.11 (the posterior state) and Fig. 3.12 (the prior state). Assimilating SST reduces the error in the entire domain. In the control run, the RMSE is as high as over 0.8°C in the west and middle part of the region. The error in the northern boundary current is also high and the modelled SST is higher than observations, indicating the modelled Leeuwin current is too strong. When SSH is assimilated, the error decreases slightly in the central part but the distribution in other part is similar. When SST is assimilated, either alone or with SSH, the RMSE in the posterior state is reduced to 0.3°C - 0.4°C in most of the domain. In the 5-day forecast (the prior state), the errors with SST assimilation is still much lower (0.4°C - 0.6°C in most of the domain) than the control run.

Sea Surface Height

For SSH the largest improvement is achieved by assimilating SSH only (ExpB). The error against AVISO data in posterior state reduces by 26% from 8.9 cm to 6.6 cm (Fig. 3.13(A)). In the control run, the error is approximately 8 cm in most of the region, but in the southern part, it is about 13 cm (Fig. 3.14(A)). When SSH is assimilated, the error in the whole domain is low (5 cm) and uniform(Fig. 3.14(B)). In the 5-day forecast, ExpB still produces a lower error (7.0 cm, Fig. 3.15(B)) than the control run showing that the signal in SSH assimilation can last at least 5 days. When SST is assimilated alone, the error in the analysis (9.6 cm) is actually higher than in the control run, especially in the autumn and winter seasons. When both SSH and SST are assimilated, the error in the analysis (8.0 cm) is lower than the SST alone assimilation, but is still higher than the control run during the last 80 days. The information contained by the SST observations is largely about the surface heat flux and mixed layer dynamics and has little effect on SSH; this type of error tends to be at large horizontal scales (e.g. Hoteit et al., 2013). Thus the error of SSH in ExpC is higher than that in the control run.

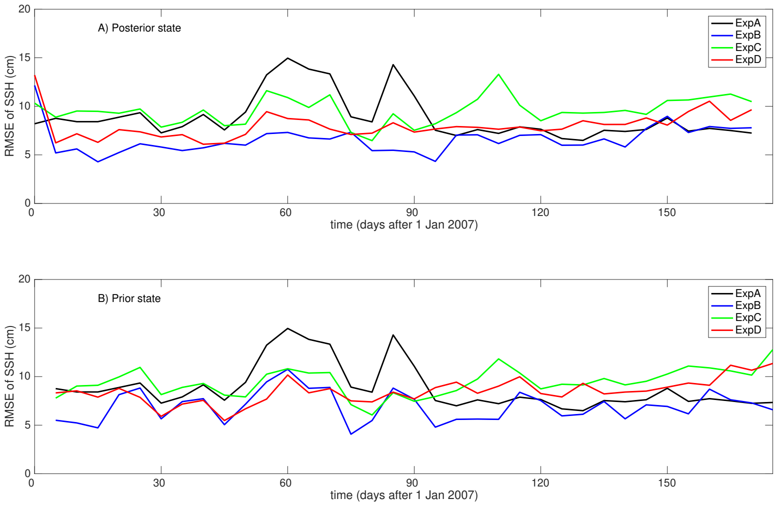

Figure 3.13 Temporal evolution of RMSE of SSH for A) posterior state (i.e., the analysis) and B) prior state (i.e., the 5-day forecast) during the period from 01/01/2007 to 01/07/2007. The units are cm.

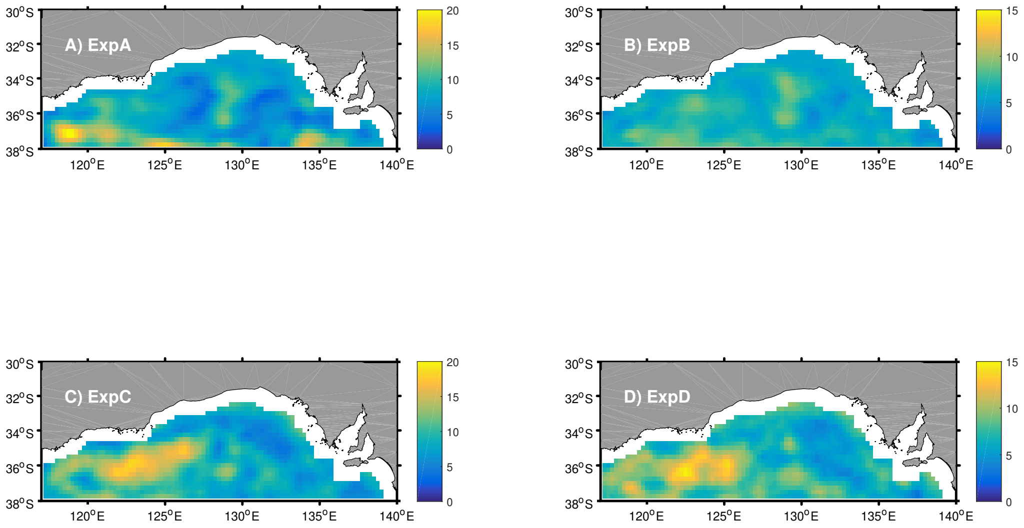

Figure 3.14 Spatial distributions of RMSE of SSH for the posterior state (i.e., the analysis) during the period from 01/01/2007 to 01/07/2007, the units are cm. Note: the color scales are different.

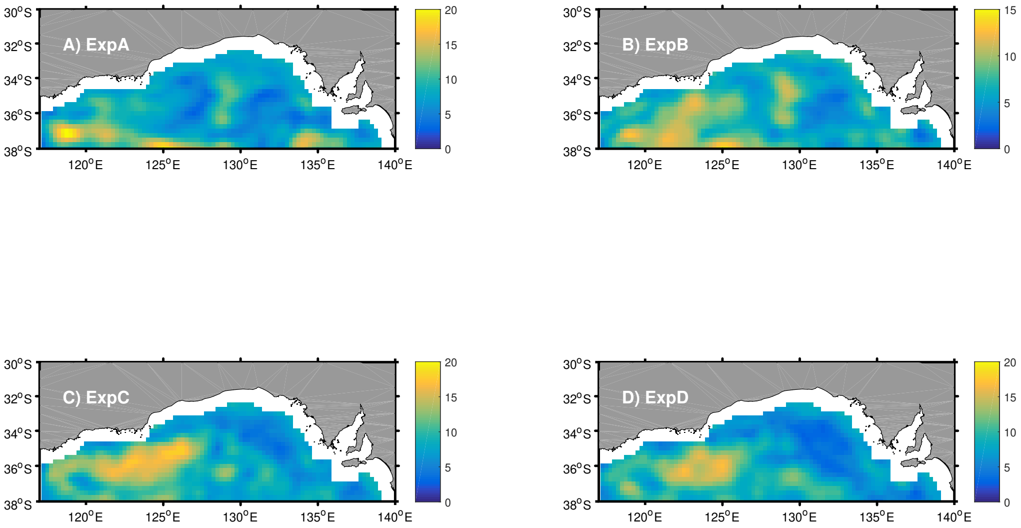

Figure 3.15 Spatial distributions of RMSE of SSH for the prior state (i.e., the 5-day forecast) during the period from 01/01/2007 to 01/07/2007, the units are cm. Note: the color scales are different.

For the spatial pattern, the error is around 10 cm in most of the domain for the control run, except in the south part where the error can be as high as 20 cm. When the SSH observations are assimilated, the error reduces to under 10 cm in the entire domain. However, when SST is assimilated, the area with high error (>10 cm) is bigger, although the maximum is lower, assimilating SSH with SST does not make much improvement.

Surface Ocean Currents

A major challenge facing ocean data assimilation and forecasting is the simulation of currents. Here the modelled surface currents are compared against OSCAR 1/3° 5-day mean ocean currents product, which provides a wide spatial and temporal coverage (Fig. 3.16). Without data assimilation, the half-year mean RMSE of the currents components u and v in the control run (ExpA) is 2.03 cm/s and 0.86 cm/s respectively. The geostrophic relationship is the major constraint for surface ocean currents and assimilating SSH produces the most realistic surface currents, the error of u and v decreases by 32% to 1.39 cm/s and 12% to 0.76 cm/s in ExpB (SSH assimilation). However, SST assimilation degrades the currents simulation during most of 6 months, no mater whether SSH is assimilated or not.

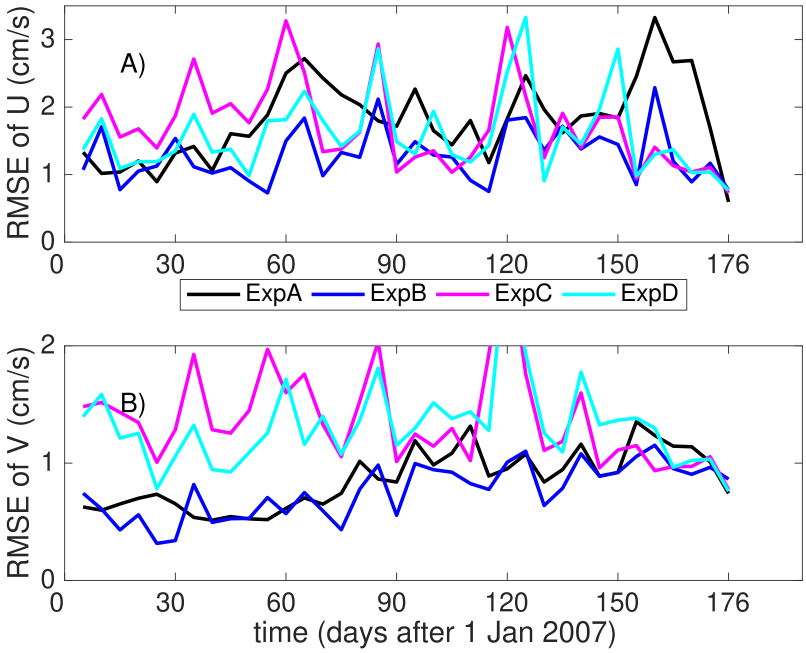

Figure 3.16 Temporal evolution of RMSE of top 30m A) zonal and B) meridional currents compared with OSCAR during the period from 01/01/2007 to 01/07/2007. The units are cm/s.

3.5 Discussion and Conclusion

In this chapter we describe an EnKF based regional ocean data assimilation system and apply it to the South Australian Sea. This system implements the Ensemble Adjustment Kalman Filter (EAKF) in the Data Assimilation Research Testbed (DART) to the Regional Ocean Modeling System (ROMS). This system is suitable for high-resolution basin-wide and coastal oceanic applications.

Sensitivity tests have been conducted and the ensemble size of 50 and the localisation radius of 0.03 arc (110 km) are selected. The ensemble size of 50 produces similar results with 100, while only consumes half of the computational time and cost. The localisation radius of 0.03 arc generates the best overall analysis of SST and SSH.

Along-track SST and SSH are assimilated separately in a 10 km resolution ROMS model of the South Australian Sea, with a 5-day period, the error of SST and SSH reduces in the analysis. However, assimilating SST deteriorates the overall estimation of SSH, especially in the winter season. On the other hand, in the SSH assimilation experiment, the distribution of SST is similar to the control run. The assimilation of both SST and SSH is similar to just SST. The influence of SST assimilation is stronger because the number of SST observations is much higher than SSH. The comparison with OSCAR dataset shows that assimilating SSH also improve the simulation of ocean currents by 32% and 12% for u and v. This system is capable of providing reliable analysis for the South Australian Sea region, and could be applied to other regions with ease.

Chapter 4

Physical Balance in EnKF

In the previous chapter, an Ensemble Kalman Filter (EnKF) based regional ocean data assimilation system has been developed and applied to the South Australian Sea. This system consists of the data assimilation algorithm provided by the NCAR Data Assimilation Research Testbed (DART) and the Regional Ocean Modelling System (ROMS). In this chapter a physical balance operator, including temperature-salinity, hydrostatic and geostrophic balance, is implemented to DART, to reduce the spurious waves which may be introduced during the data assimilation process. This is the first implementation of such a balance operator in the EnKF algorithm. The effect of the balance operator is validated in both an idealised shallow water model and the ROMS model real case study. In the shallow water model, the geostrophic balance operator eliminates spurious ageostrophic waves and produces a better sea surface height (SSH) and velocity analysis and forecast. Its impact increases as the sea surface height and wind stress increase. In the real case, assimilation with the balance operator produces a more realistic simulation of surface currents and subsurface temperature profile. The best improvement is obtained when only SSH is assimilated with the balance operator. A case study with a storm suggests that the benefit of the balance operator is of particular importance under high wind stress conditions. Implementing this balance operator could be a general benefit to ocean data assimilation systems.

4.1 Introduction

The importance of the physical balance in numerical modelling has been noted for a long time. In fact, the world's first numerical weather forecast (NWP), made by hand by L. F. Richardson in the early 20th century (Daley, 1991; Lynch, 2008, https://www.metoffice.gov.uk/research/modelling-systems/history-of-numerical-weather-prediction) failed, largely because of the spurious waves, caused by the imbalance between the pressure and wind fields, contaminated the forecast (e.g. Daley, 1991; Lynch, 2008). Data assimilation, as the main NWP initialising technique, should reduce the spurious waves to ensure the success of the forecast.

The initialisation problem in the real cases is very complicated. The observations are usually sporadic and mutually incompatible, and the density is highly variable (Daley, 1991), resulting in the posterior state that is close to the observation in some regions while close to the model forecast in other regions. Furthermore, the data assimilation algorithms are designed to fuse both observation and model results and give estimates of variables at different locations and time. Data assimilation uses the multi-dimensional probability distribution functions (PDFs), which are based on the physical relations, to connect the variables. Under the Gaussian assumption, the PDFs can be interpreted as error covariance matrices (which only reflect the mean and covariance). However, the physical balance is not necessarily represented well by the covariance matrices. For instance, Lorenc (2003a) pointed out that the balance may not be well represented when the scales of the motions are different.

In this chapter, we first describe the balance operator and its implementation in an idealised two-dimensional shallow water model and the South Australian Sea system in Section 2. In Section 3 we evaluate the effect of balance operator in both the shallow water model and the ROMS model. In Section 4 we discuss and analyse the results from Section 3. A summary concludes this chapter in Section 5.

4.2 Methods

4.2.1 Balance Operator

Recall that the Kalman Filter is written as

$$x^a = x^b + K(y - Hx^b), \tag{4.1}$$

where K is the Kalman Gain,

$$K = BH^T(HBH^T + R)^{-1}. \tag{4.2}$$

For an ocean model such as ROMS, there are 5 components in the state vector x: sea surface height η; potential temperature T; salinity S; horizontal velocities u and v. Temperature is usually the most observed variable in the ocean so Weaver et al. (2005) proposed to compute the relations between the variables based on T. Each variable except T is decomposed into two components, the balanced component and the unbalanced one. Therefore,

$$\begin{pmatrix} T \\ S \\ \eta \\ u \\ v \end{pmatrix} = \begin{pmatrix} T \\ S_B \\ \eta_B \\ u_B \\ v_B \end{pmatrix} + \begin{pmatrix} 0 \\ S_U \\ \eta_U \\ u_U \\ v_U \end{pmatrix} = L \begin{pmatrix} T \\ S_U \\ \eta_U \\ u_U \\ v_U \end{pmatrix}, \tag{4.3}$$

where the variables with subscript B represent the balanced component of the variables while those with subscript U represent the unbalanced one. The balanced part of

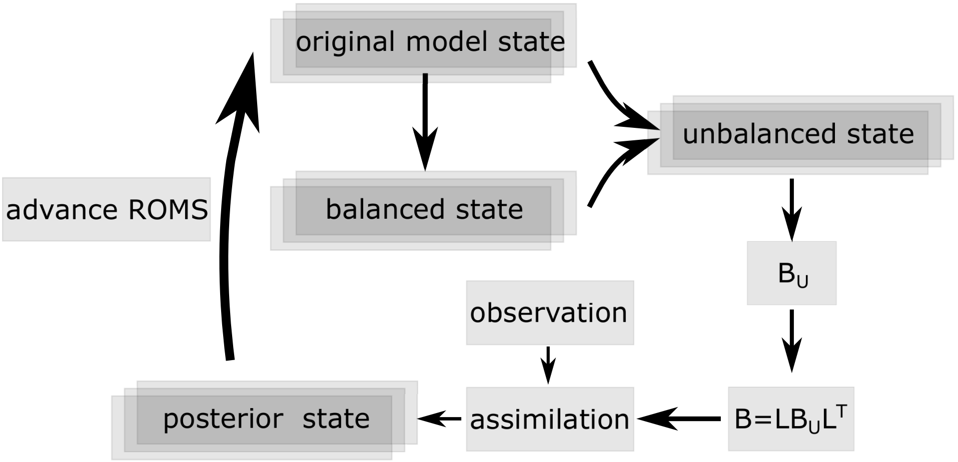

Figure 4.1 A schematic description of the balanced data assimilation system.

variable x_1 can be derived from other variable x_2 through the linear balance operator L. The details of L are explained later.

The model error covariance is thus converted to,

$$B = LB_uL^T, \tag{4.4}$$

and Eq.4.1 is written as,

$$x^a = x^b + LB_uL^TH^T(HLB_uL^TH^T + R)^{-1}[y^o - H(x^b)], \tag{4.5}$$

where B_u is the error covariance of the unbalanced components. Here we assume that the balanced components of the ocean state are correlated while the unbalanced residuals are uncorrelated (Weaver et al., 2005).

An update scheme is designed based on this algorithm. This scheme starts from an ensemble of initial model states or short-term forecast, then the balanced component is calculated and the unbalanced component is derived. B_u is computed from the unbalanced component, after which the model states are updated using Eq.4.5 (Fig. 4.1).

The Linear Balance Operator and Background Error Covariance Matrix

Weaver et al. (2005) proposed to use 3 balance constraints, the temperature - salinity balance, hydrostatic balance and geostrophic balance for ocean data assimilation, and the variables and their increments can be decomposed as following,

$$\delta T = \delta T, \tag{4.6}$$

$$\delta S = \delta S_B + \delta S_U = L_{ST}\delta T + \delta S_U, \tag{4.7}$$

$$\delta \eta = \delta \eta_B + \delta \eta_U = L_{\eta\rho}\delta\rho + \delta\eta_U, \tag{4.8}$$

$$\begin{aligned} \delta u &= \delta u_B + \delta u_U = L_{up}\delta p + \delta u_U \\ \delta v &= \delta v_B + \delta v_U = L_{vp}\delta p + \delta v_U \end{aligned}, \tag{4.9}$$

where

$$\delta\rho = L_{\rho T}\delta T + L_{\rho S}\delta S, \tag{4.10}$$

$$\delta p = L_{p\rho}\delta\rho + L_{p\eta}\delta\eta. \tag{4.11}$$

The first constraint (Eq. 4.7) is the T - S relationship which regulates the property of the water mass. It is based on the property of the prior ensemble,

$$\delta S_B = r\frac{dS}{dz}\frac{dz}{dT}\delta T, \tag{4.12}$$

where $r = 1 - e^{-z/z_M}$ is defined the same as in the ROMS-4DVAR (Moore et al., 2011b) package, z is the vertical coordinate and z_M is the mixed layer depth. The mixed layer depth is set to a constant value (200 m). In this region, the mixed layer depth is between 50 m to 120 m but under some extreme events (e.g., storms) it can be up to about 200 m. For a smaller actual mixed layer depth, this assumption will overweight the balanced salinity below the mixed layer. The density (Eq. 4.10) is a function of temperature and salinity and is calculated using a linearised version of the equation of state described by Jackett and Mcdougall (1995), where $L_{\rho T} = \rho_0 * \alpha$ and $L_{\rho S} = \rho_0 * \beta$. The reference density ρ_0 is set to 1025 kg/m^3 and α and β is the thermal expansion and saline contraction coefficients, respectively.

The second constraint is the hydrostatic balance which computes the balanced (baroclinic) sea level from the density and, therefore, temperature and salinity. The complete expression of the baroclinic relationship is an elliptic equation (Weaver et al., 2005),

$$\nabla \cdot H \nabla \delta \eta_B = -\nabla \cdot \int_{z=-H}^{0} \int_{z^{'}=z}^{0} (\nabla \delta \rho(z^{'})/\rho_0) dz^{'} dz, \tag{4.13}$$

where H is the ocean depth. Eq. 4.13 excludes the influence of advection, assuming it is not important. However, this may be problematic in the areas where the contribution of advection is great such as the coastal region. To reduce the computational cost, a simplified version of Eq. 4.13 is used in this thesis by assigning a 'depth of no motion' z_0 (1000 m in this thesis),

$$\delta \eta_B = \int_{z^{'}=z_0}^{0} (\delta \rho(z^{'})/\rho_0) dz^{'}, \tag{4.14}$$

and in regions where the ocean is shallower than z_0 Eq. 4.14 is integrated from the bottom.

Then the pressure at depth z is computed by integrating the hydrostatic equation from z to the surface,

$$\delta p(z) = \int_{z^{'}=z}^{0} (\delta \rho(z^{'}) g) dz^{'} + \rho_0 g \delta \eta, \tag{4.15}$$

The third balance operator is the geostrophic balance, which computes the increments of u and v from sea level.

$$\begin{aligned} \delta u_B(z) &= -\frac{1}{\rho_0 f}\frac{\partial \delta p(z)}{\partial y} \\ \delta v_B(z) &= \frac{1}{\rho_0 f}\frac{\partial \delta p(z)}{\partial x} \end{aligned}, \tag{4.16}$$

where f is the Coriolis force, x and y are the horizontal coordinates. The continuity constraint is not explicitly implemented, but it is satisfied above the depth of no motion because the balanced velocity is in geostrophic balance with η.

By using the above three balance constraints, the balanced component can be computed. In addition, we assume that the unbalanced components are uncorrelated with each other and thus the unbalanced error covariance is a block diagonal,

$$B_u = \begin{pmatrix} B_T & 0 & 0 & 0 & 0 \\ 0 & B_S & 0 & 0 & 0 \\ 0 & 0 & B_\eta & 0 & 0 \\ 0 & 0 & 0 & B_u & 0 \\ 0 & 0 & 0 & 0 & B_v \end{pmatrix}, \tag{4.17}$$

where B_x is the error covariance of the unbalance component of variable x. The linear balance operator matrix is a lower triangular matrix

$$L = \begin{pmatrix} I & 0 & 0 & 0 & 0 \\ L_{ST} & I & 0 & 0 & 0 \\ L_{\eta T} & L_{\eta S} & I & 0 & 0 \\ L_{uT} & L_{uS} & L_{u\eta} & I & 0 \\ L_{vT} & L_{vS} & L_{u\eta} & 0 & I \end{pmatrix}, \tag{4.18}$$

where,

$$L_{\eta T} = L_{\eta\rho} L_{\rho T},$$

$$L_{\eta S} = L_{\eta\rho} L_{\rho S},$$

$$L_{uT} = L_{up} L_{p\rho} L_{\rho T},$$

$$L_{uS} = L_{up} L_{p\rho} L_{\rho S},$$

$$L_{u\eta} = L_{up} L_{p\eta},$$

$$L_{vT} = L_{vp} L_{p\rho} L_{\rho T},$$

$$L_{vS} = L_{vp} L_{p\rho} L_{\rho S},$$

$$L_{v\eta} = L_{vp} L_{p\eta}.$$

Therefore the background error covariance matrix is,

$$LB_U L^T = \begin{pmatrix} B_{TT} & B_{ST}^T & B_{\eta T}^T & B_{uT}^T & B_{vT}^T \\ B_{ST} & B_{SS} & B_{\eta S}^T & B_{uS}^T & B_{vS}^T \\ B_{\eta T} & B_{\eta S} & B_{\eta\eta} & B_{u\eta}^T & B_{v\eta}^T \\ B_{uT} & B_{uS} & B_{u\eta} & B_{uu} & B_{vu}^T \\ B_{vT} & B_{vS} & B_{v\eta} & B_{vu} & B_{vv} \end{pmatrix}, \tag{4.19}$$

where

$$B_{TT} = B_T,$$

$$B_{ST} = L_{ST} B_T,$$

$$B_{\eta T} = L_{\eta T} B_T,$$

$$B_{uT} = L_{uT} B_T,$$

$$B_{vT} = L_{vT} B_T,$$

$$B_{SS} = L_{ST} B_T L_{ST}^T + B_S,$$

$$B_{\eta S} = L_{\eta S} B_S,$$

$$B_{uT} = L_{uT} B_T,$$

$$B_{vT} = L_{vT} B_T,$$

$$B_{\eta\eta} = L_{\eta T} B_T L_{\eta T}^T + L_{\eta S} B_S L_{\eta S}^T + B_\eta,$$

$$B_{u\eta} = L_{uT} B_T L_{\eta T}^T + L_{uS} B_S L_{\eta S}^T + L_{u\eta} B_\eta,$$

$$B_{v\eta} = L_{vT} B_T L_{\eta T}^T + L_{vS} B_S L_{\eta S}^T + L_{v\eta} B_\eta,$$

$$B_{uu} = L_{uT} B_T L_{uT}^T + L_{uS} B_S L_{uS}^T + L_{u\eta} B_\eta L_{u\eta}^T + B_u,$$

$$B_{vu} = L_{vT} B_T L_{uT}^T + L_{vS} B_S L_{uS}^T + L_{v\eta} B_\eta L_{u\eta}^T,$$

$$B_{vv} = L_{vT} B_T L_{vT}^T + L_{vS} B_S L_{vS}^T + L_{v\eta} B_\eta L_{v\eta}^T + B_v.$$

This background error covariance matrix is used in all the balanced data assimilation experiments to compute the updated mean and covariance.

4.2.2 The Idealised Shallow Water Model

The prediction of ocean currents is of particular interest and satellite observed SSH is the most widely used variable in data assimilation systems to constrain the ocean currents (e.g. Jacobs et al., 2014). It is necessary to validate the effect of the geostrophic balance operator on ocean currents. Here we use a two-dimensional shallow water model to initially evaluate the effect of the balance operator. The shallow water equations describe a rotating (with constant Coriolis parameter), inviscid fluid with wind forcing in the x direction. Similar shallow water models have been used to study the physical balance issue (e.g. Daley, 1991; Greybush et al., 2011; Kepert, 2009). The model equations are,

$$\begin{aligned}
&\frac{\partial u}{\partial t}+u\frac{\partial u}{\partial x}+v\frac{\partial u}{\partial y}-fv+\tau=-g\frac{\partial \eta}{\partial x}\\
&\frac{\partial v}{\partial t}+u\frac{\partial v}{\partial x}+v\frac{\partial v}{\partial y}+fu=-g\frac{\partial \eta}{\partial y}\\
&\frac{\partial \eta}{\partial t}+\frac{\partial}{\partial x}[u(h+\eta)]+\frac{\partial}{\partial y}[v(h+\eta)]=0
\end{aligned}, \tag{4.20}$$

where η is the free surface displacement, h is the bottom topography (50 m in this experiment), τ is the wind forcing, and f is the Coriolis parameter. We set the Coriolis parameter to $10^{-4}\mathrm{s}^{-1}$, a typical value for the mid-latitudes. The model is constructed on a 2000 by 2000 km domain with 10 km horizontal resolution in both x and y direction and forced by periodic boundary conditions.

Each ensemble is initialised from meridional η ridges,

$$\eta(x)=\eta_0 cos(\frac{2\pi}{L}(x-x_{ps})), \tag{4.21}$$

where L is the wavelength and in the true state L is set to 200 km, η_0 is the amplitude and x_{ps} is the wave phase shift. Each ensemble is forced by a periodic zonal wind stress τ with a period of 48 hours,

$$\tau(t)=\tau_0 cos(\frac{2\pi}{t_\tau}(t-t_{ps})), \tag{4.22}$$

where τ_0 is the amplitude, t_τ is the period (48 hours), and t_{ps} is the wave phase shift. The initial sea surface height of each ensemble member is generated by shifting the phase of the true initial state x_{ps} by a uniform random distribution of [20, 40] km and the amplitude η_0 by [-0.05, 0.05] m. In the initial condition of the true state and each ensemble member, the velocities are calculated according to the geostrophic balance. The wind forcing of each ensemble member is perturbed by randomly shifting the amplitude by [-10%, 10%] and the phase by [-3, 3] hr. A schematic setup of the model is displayed in Fig. 4.2.

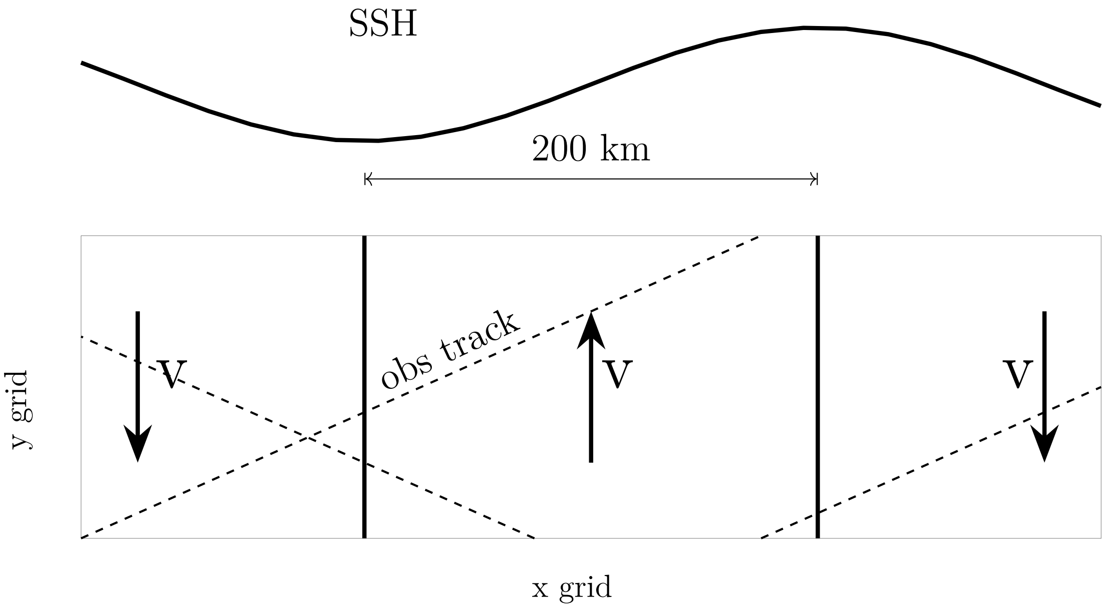

Figure 4.2 A schematic description of the shallow water model.

We first integrate the true state through a Lax-Wendroff scheme, with a time step of 6 s, for 576000 steps, or 40 days. The observations of η are then created by adding a Gaussian distributed white noise with 0 m mean and 0.03 m standard deviation to the true state. The locations of the observations are selected along 4 diagonal tracks with a 10km interval to mimic the satellite tracks. The period of the observations is set to 24 hours, and the observation tracks move eastward at a 3000 km/day speed, similar as the real satellite tracks. We conduct two sets of experiments by varying the initial SSH and wind stress, as described in Table. 4.1. In both the shallow water case and the ROMS real case, a background covariance matrix localisation technique (Gaspari and Cohn, 1999) is used. Two localisation scales (60 km and 100 km, the scale is the halfwidth of the Gaspari Cohn parameter in this chapter, as the default setup in DART) are compared in the idealised case. Larger scales have been tested but the resulting SSH and velocity fields are over-smoothed and thus not used here. In each experiment, the ensemble size is set to 100 and the error of the observations is set to 0.03 m. Each experiment is integrated for 40 days by assimilating sea surface height only with a 24-hour assimilation window and the results of the last 30 days are analysed.

Experiment set	η_0 (cm)	τ_0 (Pa)	localisation scale (km)
A (fixed τ_0 amplitude)	5,10,20,30,40,50	0.1	60,100
B (fixed η_0 amplitude)	10	0.05,0.1,0.2,0.3,0.4,0.5	60,100

Table 4.1 Experiment design for the shallow water model

4.2.3 The South Australian Sea System

The balance operator is also implemented in the South Australian Sea system. The setup is the same with that in Chapter 3, but two experiments are performed in which SSH (ExpE) and SST and SSH (ExpF) are assimilated with the balance operator.

4.3 Results

4.3.1 Idealised Shallow Water Model

Lorenc (2003a) pointed out that assimilating SSH in a shallow water model creates spurious ageostrophic waves. Fig. 4.3 shows the increments at the 25th data assimilation cycle with 0.2 Pa wind stress and 100 km localisation radius. The increment in the unbalanced experiment is strongly ageostrophic (Fig. 4.3(B)) while in the balanced experiment there is no ageostrophic current increment. The localisation reduces both SSH and velocities proportionally but increases the SSH gradient (Fig. 1.1). In addition, the wind forcing creates ageostrophic currents in the prior state and, in the unbalanced experiment, this signal propagates to the increment through the multivariate regression.

Therefore, a spurious ageostrophic shock is created in the posterior state and this degenerates the performance of data assimilation. Theoretically, the dynamical model is able to adjust and restore to a balanced state even it starts with spurious waves. However, this restored state is different from the one starting from a balanced state (not shown). In addition, this geostrophic adjustment in the dynamical model is usually not fast enough. The ageostrophic currents in the 24 hour forecast is stronger by around 3 cm/s in the unbalanced experiment than in the balanced experiment, while it is no more then 1 cm/s in the balanced experiment, when the wind stress is 0.2 Pa. Thus the balance operator is needed to reduce the misfit between the truth and assimilations in different scenarios.

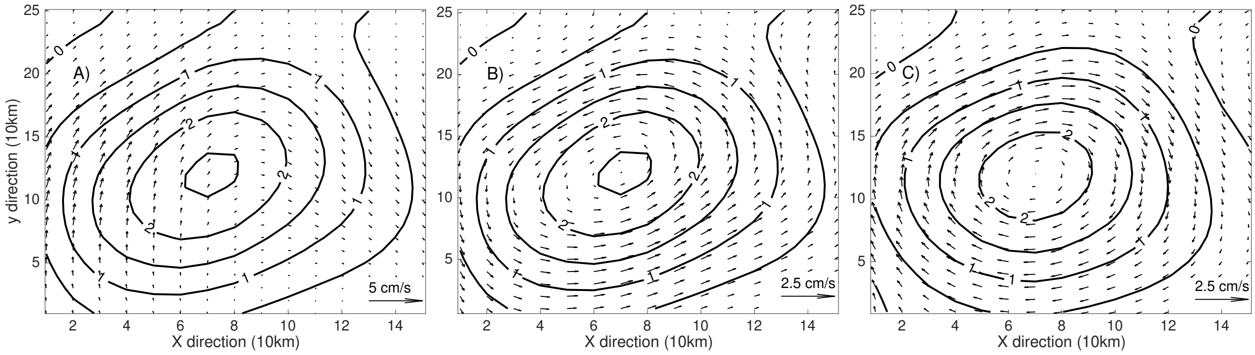

Figure 4.3 Snapshots of A) SSH (contour) and velocities (quiver) from the unbalanced experiment, B) SSH and ageostrophic velocities from the unbalanced experiment and C) SSH and velocities from the balanced experiment . The unit of SSH is cm.

The balance operator reduces the error of different variables in varying wind forcing and initial SSH displacement scenarios. Here we use the Root Mean Square Error

(RMSE) between the simulation and the true state as the metric for evaluating the assimilation. Fig. 4.4(a) and (b) display the RMSE of SSH and v velocity as a function of initial η amplitude (the amplitude does not change much in the integration), respectively. It is evident that the data assimilation with the balance operator produces a lower error for both sea surface height and velocity estimation compared to the unbalanced approach. Although the RMSE increases as the amplitude increases, the relative advantage of the balance operator also increases. In addition, a longer localisation radius is better than a shorter one for either method. However, the balanced method with smaller localisation radius outperforms the original method with the larger radius. When both use a larger radius (100 km), the balanced data assimilation produces a 17% lower average RMSE than the unbalanced approach (5.2 cm and 6.2 cm respectively) for the SSH and 11% for the v velocity (16 cm/s and 18 cm/s respectively).

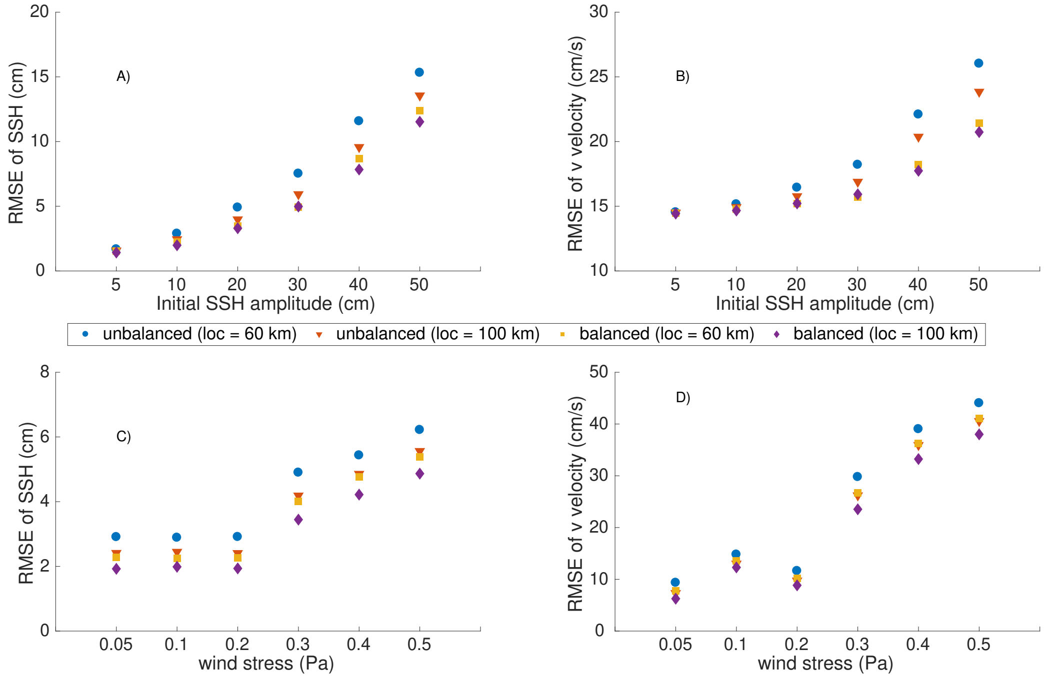

Figure 4.4 RMSE of SSH (A and C) and meridional velocity v (B and D) with varying initial η amplitude (upper panel) and wind forcing (lower panel) in the idealised case.

When forced by varying wind stress, the balance operator also improves the data assimilation performance although the error in both experiments is higher than that with fixed wind forcing, because of the noisy forcing (Fig. 4.4(c) and (d)). With a 100 km localisation radius, the average error of SSH decreases 12% from 4.2 to 3.7cm and the error of v reduces 9% from 22cm/s to 20cm/s. In the ocean, the typical value of SSH is around 10 to 20 cm while the wind stress is around 0.1 Pa. In those conditions, the balance operator reduces the RMSE of SSH and velocity by 12% (from 2.3cm to 2.0cm) and 7% (from 13cm/s to 12cm/s), respectively. The effect of the balance operator is more significant when the wind stress is larger. This is because the ageostrophic component in the prior ensembles increases as the wind stress increases, thus the increments of ageostrophic current in the unbalanced experiment get stronger. For example, when the wind stress is as large as 0.3 Pa the error increases significantly and the advantage of the balance operator is 17% and 11% for η and v respectively.

4.3.2 The South Australian Sea System

The effect of the balance operator in the South Australian model is tested by assimilating SSH alone (ExpE) and with SST (ExpF).

SST and SSH

When only SSH is assimilated, the major constraint is the geostrophic balance. If SST is also assimilated, the hydrostatic balance also provides some correction. Compared with the original algorithm, the balance operator improves the SSH and temperature estimation. As shown in Fig 4.5 and 4.6, the RMSE of both SST and SSH in ExpE (SSH assimilation with the balance operator) is lower during most of the period. Although the difference of average error is marginal in ExpB and ExpE (6.57 and 6.50 cm for SSH; 0.85 and 0.81 °C for SST, respectively), the improvement is more significant during some periods and can be as high as 0.2 °C and 1 cm. Particularly, the SSH forecast error with the balance operator is smaller by 1-3 cm than the unbalanced approach, suggesting that a posterior state with compatible SSH and velocity field is necessary for a better SSH forecast. On the other hand, if SST is assimilated, even with the balance operator (ExpF), the SSH error is higher than ExpE. This is consistent with the results in Chapter 3, indicating that assimilating SST in this region could deteriorate the model performance.

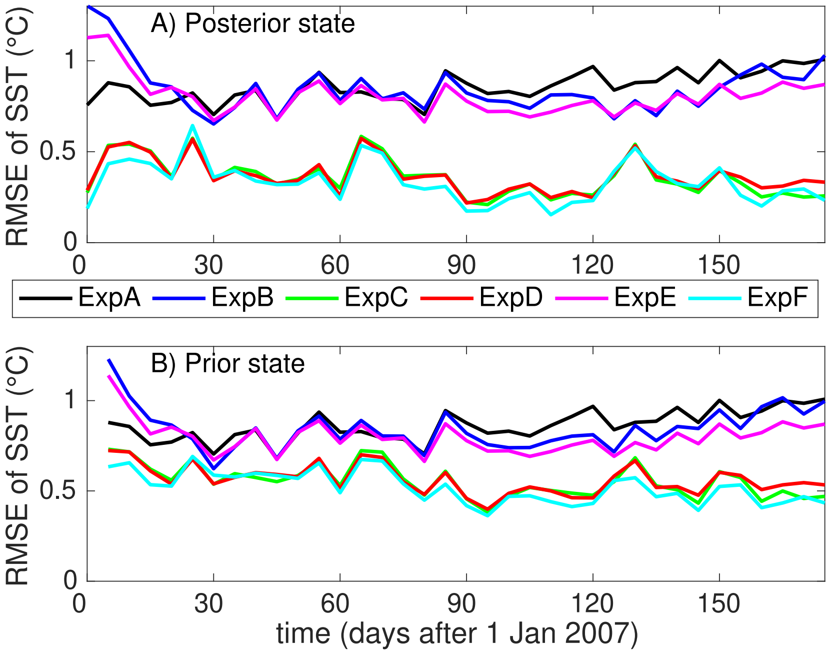

Figure 4.5 RMSE of SST for A) posterior state (i.e., the analysis) and B) prior state (i.e., the 5-day forecast). The units are °C.

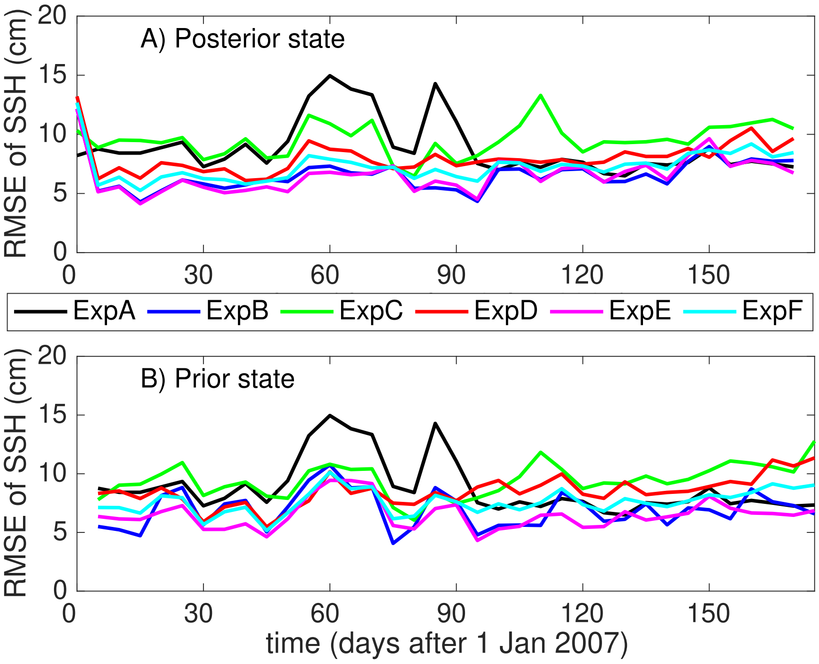

Figure 4.6 RMSE of SSH for A) posterior state (i.e., the analysis) and B) prior state (i.e., the 5-day forecast). The units are cm.

Subsurface Temperature and Salinity

The comparison with Argo temperature and salinity profiles shows that, assimilating surface observations using the original approach affects the simulation, although the subsurface variables are not assimilated (Fig. 4.7, Table 4.2). For instance, assimilating SSH alone reduces the RMSE of temperature and salinity by 12% (0.14°C) and 10% (0.02 PSU), respectively, in the upper 300 m. Assimilating SSH also reduces the error of temperature and salinity in the deeper ocean. On the other hand, in ExpC (assimilating SST alone), the error of temperature reduces by 10% (0.12°C) in the upper 300 m but increases by 7% (0.07°C) in 300-700 m, indicating the simulation of ocean circulation is degenerated. ExpD also shows that assimilating SST increases the error under 300 m. When the balance operator is used the results are better and assimilating SSH with the balance operator is an optimal way to improve the subsurface temperature and salinity profiles. For example, compared to ExpB, the improvement of temperature in ExpE is as high as 0.12 °C (12%) for the upper 300 m. The error of salinity shows a similar trend.

Surface Ocean Currents

A major challenge facing ocean data assimilation and forecast is the simulation of currents. The results demonstrate the benefit from the geostrophic balance. As in Chapter 3, the modelled surface currents are compared against OSCAR 1/3° 5-day mean ocean currents product (Fig. 4.8). The geostrophic balance is the major constraint on ocean currents. When SSH is assimilated with the balance operator, the half-year averaged RMSE of the currents components u and v reduces by 27% to 1.02 cm/s and 23% to 0.59 cm/s, respectively, compared with ExpB (SSH assimilation using the original EAKF). When SST is also assimilated, even with the balance operator, the results are not as good as SSH assimilation only (figure not shown), in line with the results in Chapter 3. The performance of the balanced EAKF is thus the best

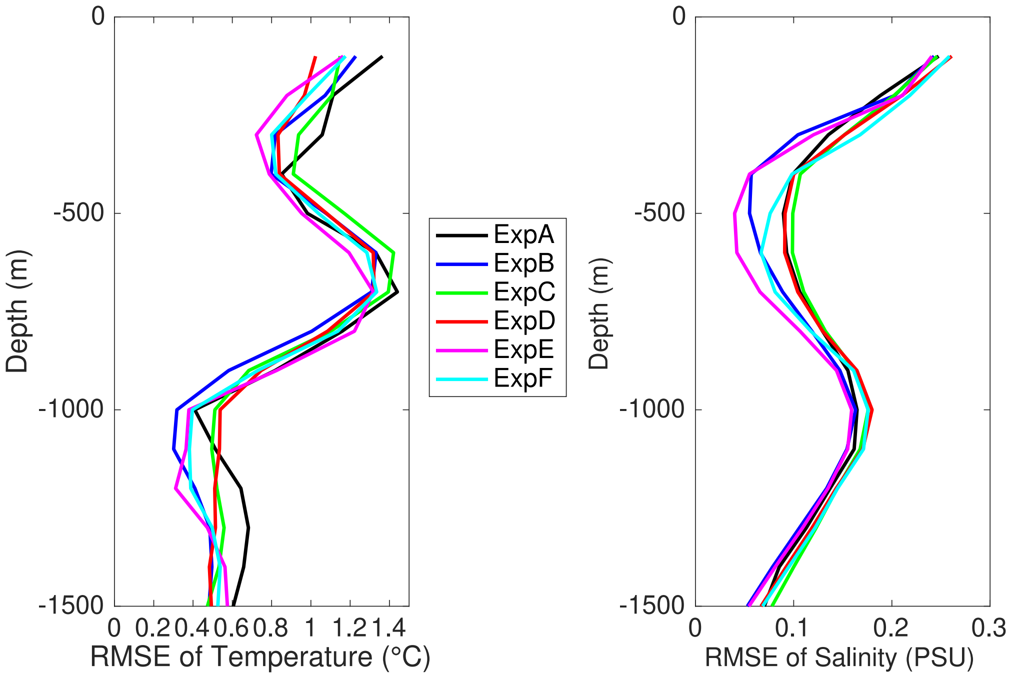

Figure 4.7 RMSE of subsurface temperature vertical profile.

among all three experiments and reduces the error by 40% to 50% compared to the control run (2.03 cm/s and 0.86 cm/s for u and v, respectively). The comparison with OSCAR data may be unfair since the OSCAR currents are mainly geostrophic, but a comparison with the drifter derived surface currents gives similar results (Table. 4.2), although the error is much higher than that compared with the OSCAR data.

The spatial pattern of surface currents (Fig. 4.9) also demonstrates the advantage of the balance operator for the currents simulation. In the control run the model is able to capture the eastward coastal currents but the currents are too strong and reach the east coast of the Great Australian Bight. In addition, an anticyclonic eddy is observed in the middle of the domain (127°E˜130°E, 34°S˜37°S) in the OSCAR dataset. The control run does not produce this eddy and the speed error is around 4cm/s in this region. When SSH is assimilated, even when the balance operator is not used, the over strong north boundary currents is weaker and more realistic. The assimilation

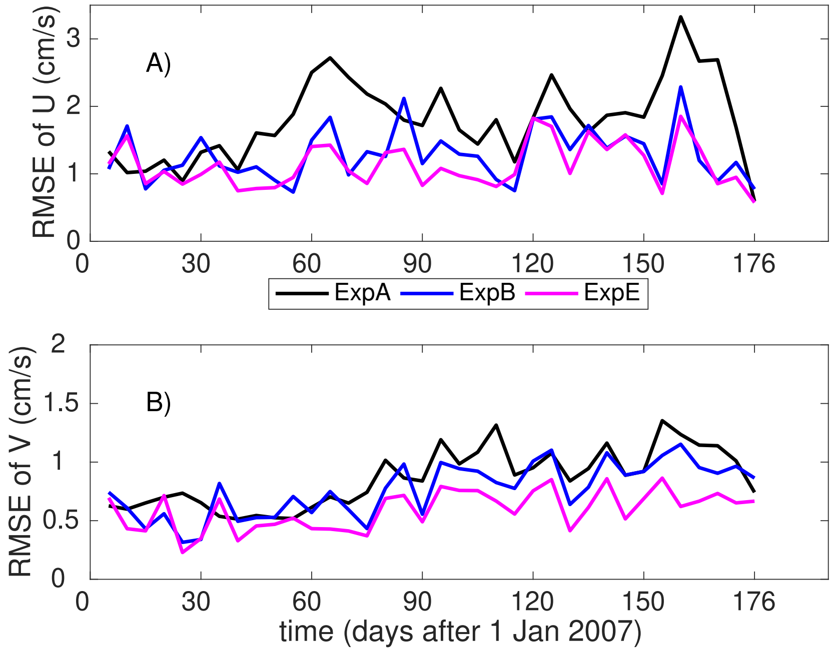

Figure 4.8 RMSE of top 30m A) zonal and B) meridional currents compared with OSCAR. The units are cm/s.

	ExpA	ExpB	ExpC	ExpD	ExpE	ExpF
SSH	8.87	6.57	9.55	7.98	6.50	7.28
SST	0.86	0.85	0.36	0.37	0.81	0.33
u	25.80	20.73	23.79	23.81	19.52	21.40
v	21.32	19.23	23.13	22.35	18.19	20.73
t (100-300m)	1.18	1.04	1.06	0.94	0.92	0.99
t (300-700m)	1.15	1.13	1.22	1.14	1.06	1.12
t (700-1500m)	0.69	0.51	0.61	0.61	0.59	0.57
s (100-300m)	0.20	0.18	0.21	0.19	0.18	0.21
s (300-700m)	0.09	0.07	0.10	0.05	0.06	0.08
s (700-1500m)	0.13	0.12	0.14	0.12	0.12	0.13

Table 4.2 The RMSE of SSH, SST, surface currents and subsurface temperature and salinity compared with AVISO, OISST, drifter and ARGO data. The units are cm, °C, cm/s, °C and PSU respectively.

also reproduces the anticyclonic eddy, and the assimilation with the balance operator (speed error ˜2 cm/s) is more realistic than without(speed error ˜2.5 cm/s).

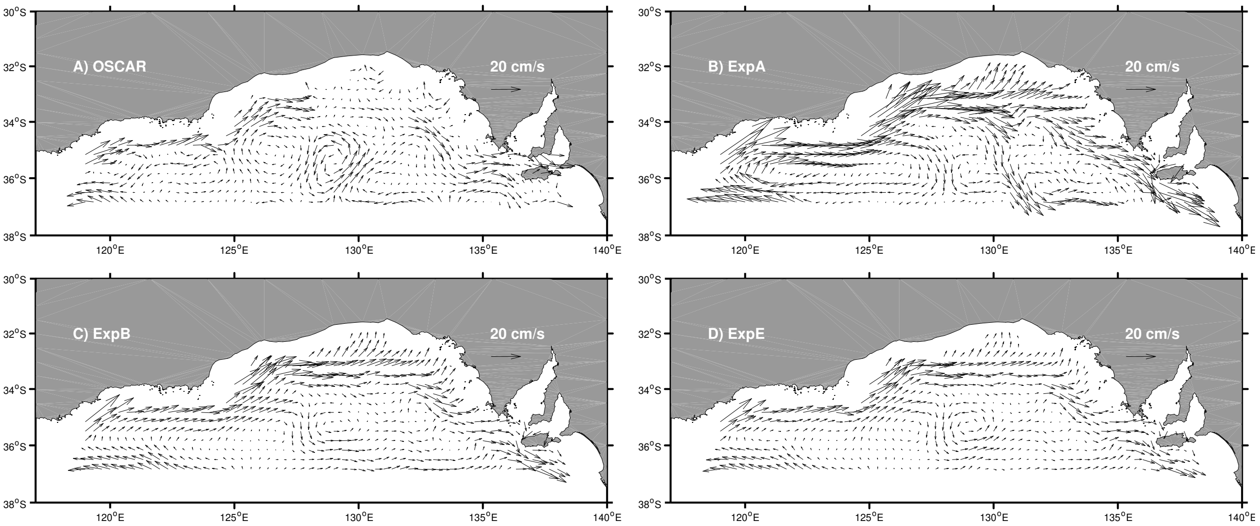

Figure 4.9 A comparison of top 30m currents of A) OSCAR dataset, B) ROMS control run, C) SSH assimilation without the balance operator and D) SSH assimilation with the balance operator.

A Case Study with Strong Wind Forcing

From 26 March 2007 to 27 March 2007, a storm passed the region, with a mean wind stress of 0.22 Pa and a maximum of 0.31 Pa. This process is of particular importance because a data assimilation cycle starts on 27 March 2007. Therefore the prior state is strongly unbalanced because the storm creates strong ageostrophic currents and the posterior state is also unbalanced. Fig. 4.10 depicts the ageostrophic currents in SSH assimilations with and without balance operator in a sub-domain significantly impacted by this storm (126°E˜132°E, 34°S˜37°S). The ageostrophic currents are stronger without balance operator (25.1 cm/s and 20.8 cm/s in ExpB and ExpE respectively). In the prior state (5-day forecast) on 01 April 2007, the ageostrophic currents reduce in both experiments but remain stronger in the unbalanced experiment

(13.7 cm/s and 10.3 cm/s). The comparison between simulated SSH and the AVISO observation also shows that the balanced experiment is more realistic (Fig. 4.11).

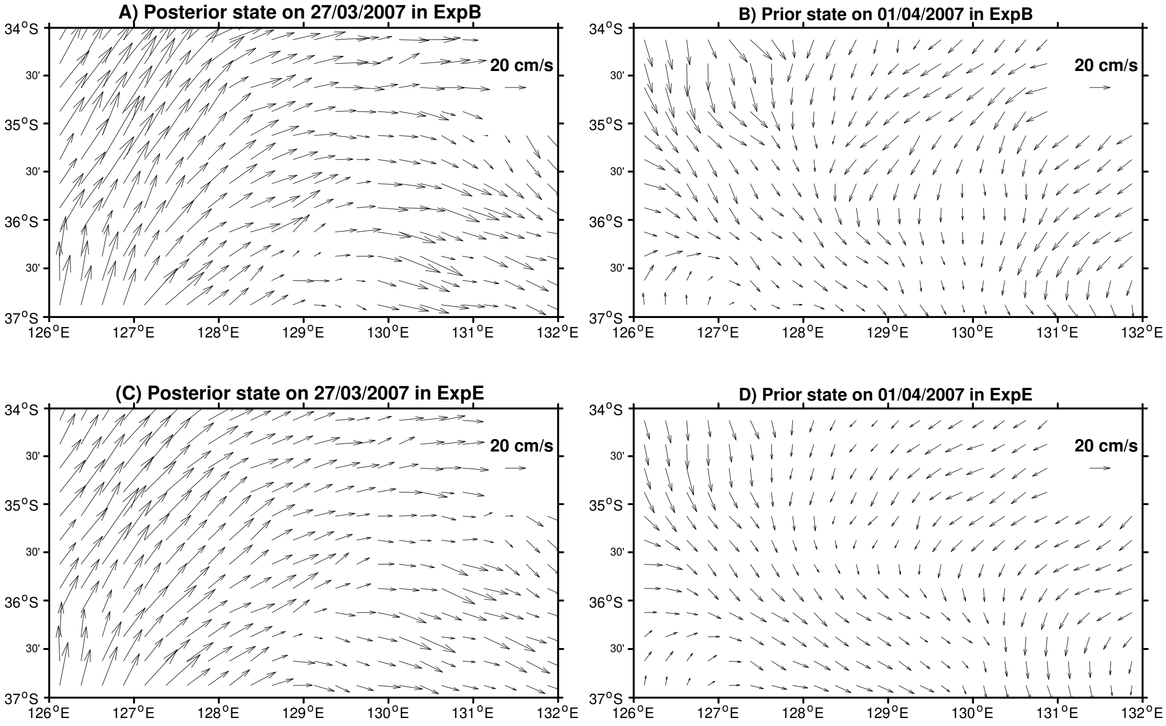

Figure 4.10 Snapshots of surface ageostrophic currents of the posterior state on 27/03/2007 and the prior state on 01/04/2007 in SSH assimilation without (ExpB) and with (ExpE) the balance operator.

When compared with the OSCAR dataset, the domain-averaged error of the 5-day mean surface currents during this period with the balance operator (1.4 cm/s and 0.7 cm/s for u and v respectively) is much smaller than that without balance operator (2.1 cm/s and 1.1 cm/s for u and v respectively). Daily differences between these two experiments are up to 3.2 cm/s. However, the daily observations are not available to verify which experiment is better. This case study suggests that when the wind stress is large (e.g., greater than 0.2 Pa) and hence the ageostrophic currents are strong, the balance operator is essential for a better estimation of the surface currents.

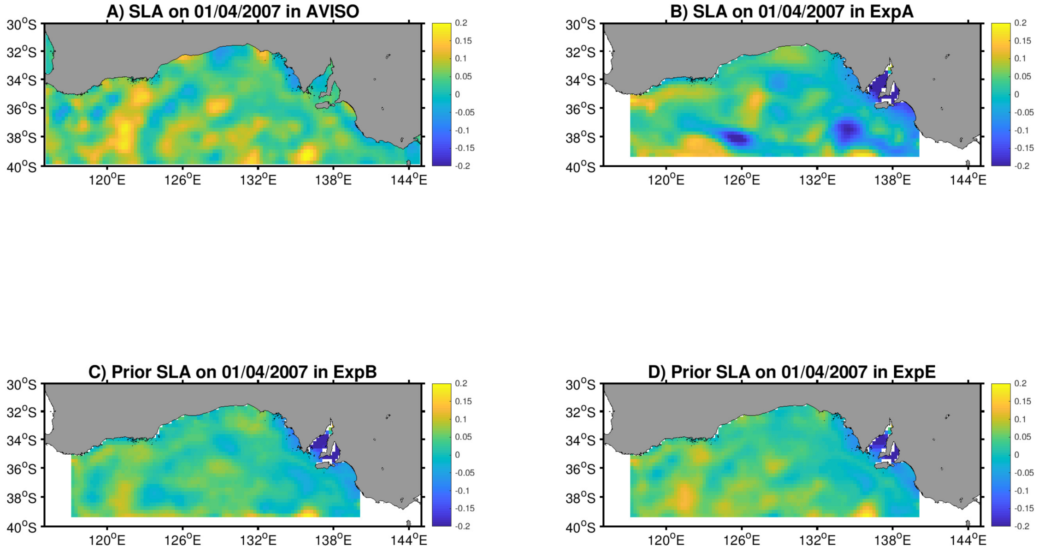

Figure 4.11 Snapshots of SLA of AVISO, the control run and the prior state on 01/04/2007 in SSH assimilation without (ExpB) and with (ExpE) the balance operator.

4.4 Discussion

In this chapter, we add a balance operator to the ensemble system and assimilate the surface observations in both an idealised and a real cases and reduce the imbalance caused by the data assimilation process. Numerical models are designed to be physically balanced so the forecast of each ensemble should be equilibrated. However the combination of observation and numerical model is not balanced so data assimilation introduces imbalance and spurious waves into the dynamical systems (e.g. Greybush et al., 2011; Kepert, 2009; Lorenc, 2003a; Neef et al., 2006). Theoretically, the numerical model is able to remove the imbalance within a certain period but the effect of unbalanced waves has been shown to be important in this study and other studies (e.g. Kepert, 2009; Neef et al., 2006). Several methods have been proposed to eliminate such waves. For example, by using a low-order idealised model, Neef et al. (2006) have demonstrated that the waves can be removed by increasing the ensemble size and decreasing the assimilation window, but it is usually difficult to do so in the high-dimensional GCMs.

Due to the small ensemble size, the covariance used in EnKFs is usually insufficient to represent the true relationship between state variables. Estimates of the background error covariance between substantially distant grid points are often exaggerated when using a small ensemble size (Houtekamer and Mitchell, 1998). Therefore a localisation procedure is necessary. However, localisation also causes spurious waves (e.g. Greybush et al., 2011; Lorenc, 2003a) and thus is a main disadvantage of EnKFs.

Following Weaver et al. (2005), three physical balance constraints (temperature-salinity, hydrostatic and geostrophic balance) are used in this chapter to reduce these spurious waves. We use an idealised shallow water model to reveal how the geostrophic balance operator enhances the data assimilation by removing the initial spurious ageostrophic waves. In this idealised model, the increment is strongly unbalanced (Fig. 4.3) without the balance operator and the spurious waves persist more than 24 hours. The unrealistic ageostrophic currents reduce the performance of data assimilation and therefore a balance operator is needed.

In the real case, the balance operator is also valuable in the estimation of ocean currents. Fig. 4.12 displays an example of the ensemble correlation between SST, SSH and surface and subsurface zonal ocean currents from a prior ensemble in the SSH only assimilation (ExpB). The correlation of surface variables with ocean currents is defined as,

$$\begin{aligned} C_{HUV} &= \sqrt{\frac{1}{2}(Corr(SSH,U)^2 + Corr(SSH,V)^2)} \\ C_{TUV} &= \sqrt{\frac{1}{2}(Corr(SST,U)^2 + Corr(SST,V)^2)} \end{aligned} \quad . \tag{4.23}$$

It is evident that in most of the region the correlation between surface observed variables and ocean currents is noisy and weak (less than 0.5 in most of the region). For

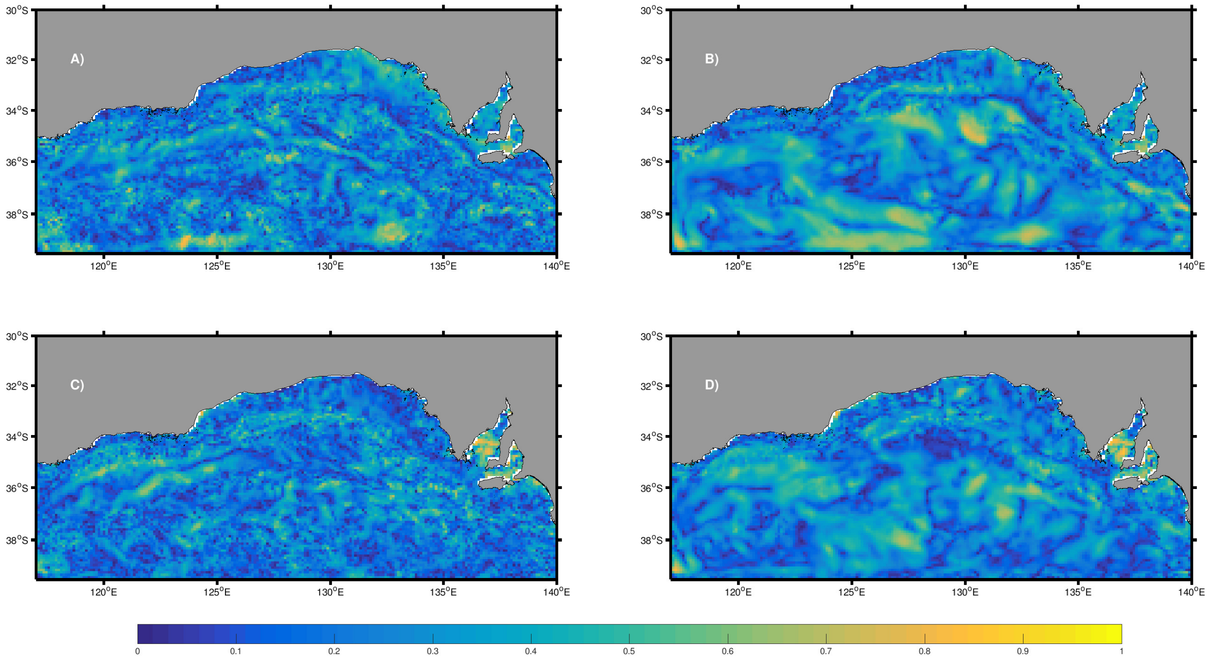

Figure 4.12 Ensemble correlations between surface variables and surface and subsurface currents on 30 January 2007 in ExpB. A) Correlation between SST and 5m currents, B) Correlation between SST and 200m currents, C) Correlation between SSH and 5m current, D) A) Correlation between SSH and 200m currents.

the deeper currents, the correlation is slightly stronger, especially in the southern part. Further analysis (figure not shown) reveals that in the eastern part the currents are dominated by wind stress and the southern part features with stronger SSH variability. This could explain why EAKF and Ensemble Optimal Interpolation (EnOI) show good results in the Gulf of Mexico (Counillon and Bertino, 2009; Hoteit et al., 2013) where the SSH variability is dominated by the loop current and the correlation between SSH and surface currents is high (around 0.7 - 0.8, (Counillon and Bertino, 2009)). However, in the Southern Australian Sea, the SSH variability is not constant and shows lower correlation with ocean currents. Thus EAKF gives worse currents result when only SSH is assimilated. Therefore the physical constraint is particularly important in this region.

The advantages of the balance operator have been shown in both an idealised shallow water model and the ROMS real case, in which the error of temperature, salinity, SSH and velocities reduces. Especially for the subsurface temperature and salinity, when SSH is assimilated with the balance operator, the simulated error reduces dramatically in each layer. This indicates a better subsurface ocean circulation is produced. When SST is also assimilated, the error increases. This may be because the SST information in this region does not reflect the mesoscale ocean dynamics, which also seen in the unbalanced experiments. Compared with other approaches (e.g., using the streamfunction-velocity potential covariance, Kepert, 2009), this balance operator is straightforward and easy to compute and implement. In this work, the balanced part of sea surface height is approximated by integrating the density from a reference level. However, in regions where the bathymetry is complicated, that may be questionable. Another potential challenge of implementing the balance operator is that the mixed layer depth varies in time and space, but here we assign a constant value. Nevertheless, we anticipate this to be a minor correction.

4.5 Conclusion

Chapter 3 describes an EnKF based regional ocean data assimilation system. Like all other ensemble-based data assimilation systems, this system is deteriorated by spurious waves generated in the data assimilation process, due to the small ensemble size and localisation. In this chapter, we add a physical balance operator to eliminate these spurious waves. The effect of the balance operator is first demonstrated in a two dimensional shallow water model for different localisation scale. A larger localisation shows advantages over the smaller one. For both localisation scales, the balance operator decreases the error of sea surface height and velocities. It is also shown that the benefit of balance operator increases as the amplitude of SSH and wind stress increase.

Then the balance operator is tested in the South Australian Sea data assimilation system, with the SSH only and SSH and SST assimilation experiments. The estimations of both SSH and temperature are improved, especially for the forecast, indicating a balanced posterior state is important. The balance operator is important in the estimation of ocean currents, assimilating SSH with the balance operator produces ocean currents the most comparable with OSCAR dataset. The error of u and v is reduced by 27% and 23% compared with the original data assimilation, and 40% to 50% compared with the control run. The comparison with drifter derived surface currents shows similar results. The error of temperature and salinity profiles against Argo data suggests assimilating SSH with balance operator produces the most realistic subsurface temperature and salinity. A case study with a storm affecting this region shows that under high wind forcing condition the balance operator reduces the ageostrophic currents significantly in both analysis and forecast. The results in all experiments performed in this study suggest that the balance operator described here may be useful to implement generally in ocean data assimilation systems.

Chapter 5

Improved TC forecast by assimilating coastal currents

In this chapter, an ocean-atmosphere coupled model is developed to assimilate coastal surface currents in a tropical cyclone (TC) forecast model. High-frequency (HF) radars can provide high-resolution and frequent ocean surface currents observations during the TC landfall. We describe the first assimilation of such potential observations using idealized Observing System Simulation Experiments. The data assimilation system consists of the Ensemble Adjustment Kalman Filter (EAKF) and a coupled ocean-atmosphere model. In this system, synthetic HF radar observed coastal currents are assimilated and the forecast performances for weak (Category 2) and strong (Category 4) TCs are examined. Assimilating coastal surface currents improves the 24-hour forecasts of both intensity and track. For the strong case, the errors of the maximum wind speed (V_{max}) and the integrated power dissipation (IPD) forecast reduce up to 50%. For the weak case, the improvements in V_{max} and IPD forecast are lower (20%), but the track forecast improves 30%. These improvements are similar to the magnitude of the current operational TC forecast error, so that assimilating HF radar observations could be a substantial benefit.

5.1 Introduction

Tropical cyclones (TCs) affect the populous coastal regions frequently, causing casualties as well as economic and societal losses so the predictions of TC intensity and track are of great importance. Many observations have been assimilated to improve the short-term prediction of TCs, including both oceanic and atmospheric variables (e.g. Dong et al., 2017; Zhang et al., 2009). However, the errors in the TC intensity forecasts have not decreased significantly during the past decades (e.g. Goni et al., 2017). Recently coupled systems have been used widely in weather centres, especially for the forecast of intensively air-sea interaction phenomena, including TCs (e.g. Ito et al., 2015). Coupled data assimilation is thus needed for the initialisation. The coupled data assimilation systems are divided into two categories: weakly-coupled and strongly-coupled. The strongly-coupled data assimilation is used in this chapter to provide initial conditions in an idealised coupled TC forecast model. When using the ensemble approaches, as in this chapter, the strongly-coupled data assimilation is superior (e.g. Sluka et al., 2016).

Here we assimilate synthetic surface currents potentially observed by HF radar in an idealised model using the strongly-coupled data assimilation. The data assimilation algorithm is the Ensemble Adjustment Kalman Filter (EAKF) algorithm (Anderson, 2001) provided by the data assimilation research testbed (DART) package (Anderson et al., 2009).

5.2 Methods and Data

5.2.1 Model Description

The strongly-coupled data assimilation system (Fig. 5.1) consists of an atmosphere-ocean coupled model and an ensemble-based data assimilation algorithm. The coupled model is a ROMS (Regional Ocean Modelling System) and WRF (Weather Research and

Forecasting model) coupled model within the COAWST (Coupled-Ocean-Atmosphere-Wave-Sediment Transport modeling system, Warner et al. (2010)) framework. The domain is a 2500 km (in x direction) × 2000 km (in y direction) rectangle. The horizontal resolutions are set to 5 km for both ROMS and WRF. There are 31 and 27 vertical layers in WRF and ROMS, respectively. A constant Coriolis parameter of 5×10^{-5} s^{-1} is used.

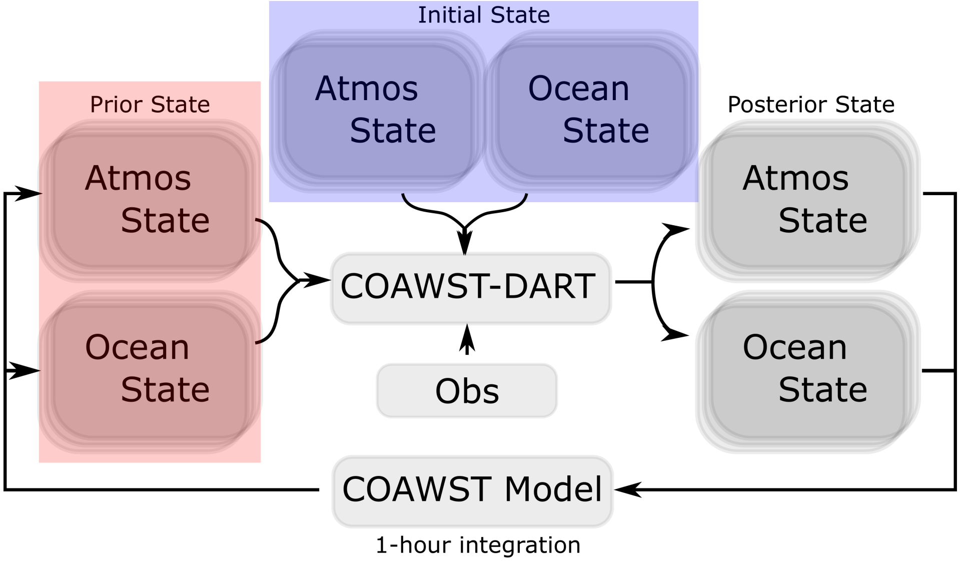

Figure 5.1 Schematic illustration of the strong-coupled DA system. At the beginning of the first cycle, the system starts from the top (blue rectangle) in which the initial state (including both oceanic (horizontal currents, temperature, salinity and sea surface height) and atmospheric variables (horizontal wind speeds, geopotential height, temperature, surface pressure and humidity)) and observed surface currents are assimilated. The posterior is used as initial condition for the 1-hour integration, whose output (prior state, red rectangle) is assimilated in the next cycle. This process repeats for 3 cycles.

Both strong and weak TC scenarios are tested in this chapter. The initial conditions for WRF are specified using the λ model proposed by Wang et al. (2015). In the λ model, the wind speed is defined as following,

$$V = \sqrt{\frac{2(P_{env} - P_{min})}{\rho}} \times \sqrt{\frac{2\lambda^2}{r^2}(1 - e^{-\frac{r^2}{2\lambda^2}}) - e^{-\frac{r^2}{2\lambda^2}}} - \frac{1}{2} f r. \tag{5.1}$$

Where V is the tangential wind speed near the surface, r the radius from the cyclone center, ρ the air density set as 1.1 kg m^{-3}, P_{env} the pressure in the ambient environment set as 1013 hPa, f the Coriolis parameter. λ represents the width of the Gaussian distribution of moist entropy in the boundary layer.

Based on the air-sea interaction theory by Emanuel (1986), Wang et al. (2015) gives the analytical solution of λ as,

$$\lambda = \frac{R_{th}(fR_{th}+2V_{th})}{4}\sqrt{\frac{\rho}{P_{env}-P_{min}}}. \tag{5.2}$$

where V_{th} is a threshold wind speed and R_{th} the radius of V_{th}. When the wind speed in Eq. 5.1 reaches the maximum value (V_{max}), the numerical solution for R_{max} can be written as

$$\lambda = \frac{1}{1.89}R_{max}, \tag{5.3}$$

and V_{max} is

$$V_{max} = 0.77\sqrt{\frac{2(P_{env}-P_{min})}{\rho}} - \frac{1}{2}fR_{max}. \tag{5.4}$$

Therefore Eq. 5.1 can be written as

$$V = \sqrt{2}\frac{V_{max}+fR_{max}}{0.77} \times \sqrt{2(\frac{R_{max}}{1.89r})^2(1-e^{-\frac{1}{2}(\frac{1.89r}{R_{max}})^2} - e^{-\frac{1}{2}(\frac{1.89r}{R_{max}})^2}} - \frac{1}{2}fr. \tag{5.5}$$

In practice, one needs to specify V_{max} and R_{max} to obtain the near-surface wind distribution. The vertical structure of the wind field is obtained by decaying the horizontal wind field linearly with height (Rotunno and Emanuel, 1987). The environmental sounding profile is obtained from the mean tropical sounding during the tropical cyclone season from July to October (Jordan, 1958). The parameterisation configurations are important for the success of the TC simulation, the set-up described in Chapter 2 is used here.

In the weak TC case, the initial condition is set with sea surface temperature (SST) of 28.5°C, the radius of maximum wind speed of 50km and the maximum wind speed of 30m/s in the centre of the domain and steering flow of 5.5m/s. Then the model is integrated for 3 days to create the model 'truth'. The 'truth' of the strong TC is created in the same manner, but the initial vortex (SST = 33°C, R_{max} = 80km, V_{max} = 50m/s) needs a 3-day spin-up in an uncoupled WRF model without any steering flow, before the WRF model is coupled with ROMS with a steering flow (6.0 m/s) added. Then the coupled model is integrated for 3 days. We take these 2 runs as the synthetic observations and calculate the errors against them. These initial conditions and initialisation approaches are selected to develop TCs of Category 2 and 4 intensities, the sensitivities in WRF and COAWST models have been tested in previous studies (Bruneau et al., 2018).

In ROMS the depth is set to 1500 m and the land is located in the west of the domain with is 250km (50 grids) width (Fig. 5.2). The subsurface temperature and salinity profiles are from the World Ocean Atlas (WOA) climatological dataset in the topical western Pacific (with SST of 28.5°C). In the strong TC case, the temperature profile is artificially increased in the top 100 m such that the SST is 33 °C and T_{100m} is 32 °C, so that the intensity of the TC is maintained. The parametrisation schemes of ROMS are the same in Chapters 3 and 4.

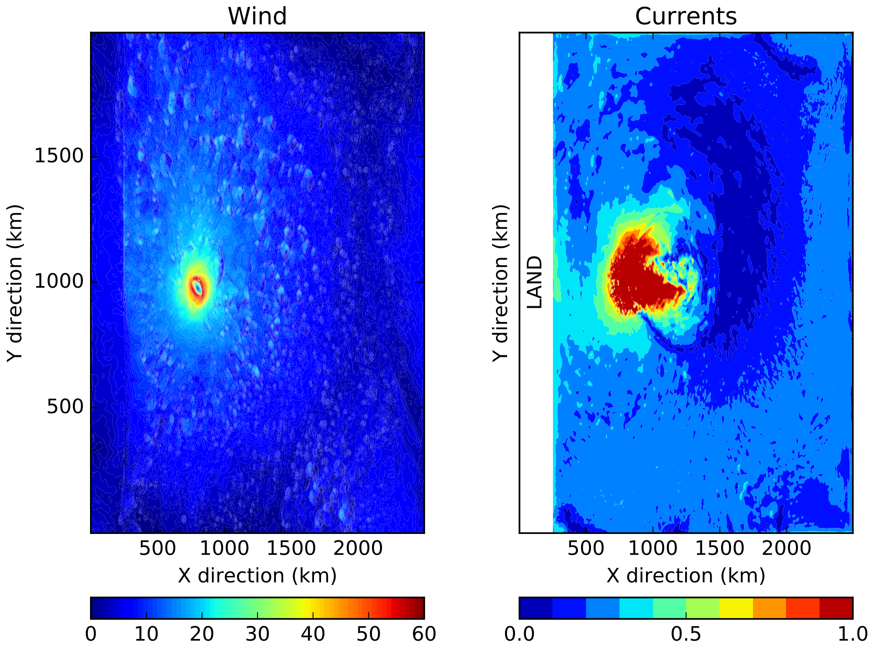

Figure 5.2 Snapshots of surface wind speed and surface ocean currents speed at Hour 24 (i.e., 28 hours before landfall) in the strong TC case.

5.2.2 Data Assimilation

Observing System Simulation Experiments (OSSEs) are often used to estimate the value of potential observations or the benefit of data assimilation (e.g. Halliwell et al., 2017b; Sluka et al., 2016). OSSEs are based on twin experiments where synthetic observations are assimilated in different ways. Here we design the twin experiments that one assimilates the synthetic ocean currents (hereafter DA) and the other does not (hereafter NoDA).

The initial ensembles play an important role in the success of a data assimilation system. In this study we generate the ensembles by perturbing the model 'truth'. For both strong and weak TC, the coupled models are perturbed at Hour 12 for the 24-hour forecast and Hour 24 for the 12-hour forecast, using the cv3 background error covariance option (Barker et al., 2004) in the WRF three-dimensional variational data assimilation (3DVAR) package. The perturbed variables include horizontal wind components, potential temperature, and mixing ratio for water vapour. In the weak case, the perturbation standard deviations thus generated are approximately 1.3 m/s for horizontal wind components (u and v), 1.0K for temperature (T), 1.0 hPa for pressure perturbation (P), and 0.8 g/kg for the water vapour mixing ratio (q). In the strong case, the standard deviations are approximately 1.7 m/s for u and v, 1.5K for T, 1.0 hPa for P, and 1.7 g /kg for q.

In both strong and weak TC cases, the observations are created from the corresponding model 'truth' by extracting the top layer (about 28 cm) ocean currents located 5km to 200km (1 to 40 grids) away from the coastline with 5 km spatial resolution and hourly temporal resolution, similar to what HF radar systems can achieve. The data within 600 km from the south and north boundaries are discarded.We assume that the observations have independent, Gaussian random errors of 0 mean and variance of 10 cm/s (Paduan and Washburn, 2013). Sensitivity tests (shown later) confirm that 10 cm/s is an optimal value, as smaller values inhibit TC model simulation and larger values make little difference. The observations are assimilated using EAKF provided by DART, which supports many geophysical models including ROMS (Li and Toumi, 2017) and WRF (Anderson et al., 2009). In the strongly-coupled data assimilation system, the error covariance matrix is calculated using the variables of both models. 40 ensemble members are used in this study. The localisation technique is needed in the ensemble data assimilation with limited ensemble size to reduce the spurious covariance between distant points (e.g. Houtekamer and Mitchell, 2001; Miyoshi et al., 2014). The Gaspari-Cohn localisation algorithm (Gaspari and Cohn, 1999) is used in this study with the half-width radius of 700 km. Vertically, the localisation is 5 layers for WRF and no vertical localisation is used for ROMS. The horizontal localisation scale is selected after several sensitivity experiments. The correlations between atmospheric vertical profiles (temperature, humidity and wind) with the local surface ocean currents are computed and the correlations are high below 940 hPa (the bottom 5 layers), thus the vertical localisation scale of 5 is chosen (Fowler and Lawless, 2016; Smith et al., 2017). In this study, we perform 24- and 12-hour forecast experiments for both strong and weak cases. The 24-hour forecast starts at 28 hours before the landfall (i.e., Hour 24) and the 12-hour forecast starts 12 hours later. In each of the experiments, 3 cycles of assimilation with 1-hour window are performed and then the forecasts are made.

5.2.3 Forecast Evaluation

Conventionally, the maximum wind speed (V_{max}) is used to estimate the destructiveness of TCs. However, V_{max} does not directly reflect the size and structure of TCs and therefore can be misleading for some large cyclones. For example, Hurricane Sandy (2012) caused great damage in the Caribbean islands and the U.S. although its peak $Vmax$ was just 100 kt (51 m/s, Category 3). Thus other metrics are needed to approximate the damage potential. The integrated power dissipation (IPD, Emanuel (2005)) has been developed recently and studies have shown that IPD is superior to V_{max} in describing the damage potential (e.g. Wang and Toumi, 2016). IPD is defined as the integration of the power dissipation of the surface wind field,

$$IPD = \int_V \rho C_D U^3 dV, \tag{5.6}$$

where ρ is the air density (1.1 kgm^{-3}), C_D the drag coefficient (Large and Yeager, 2009), V the integral area with the wind speed of at least gale force (18 m/s) and U the 10 m wind speed. In this study, V_{max}, P_{min} and IPD are used as metrics of TC intensity. The metrics of each ensemble member are calculated separately and the error is the difference between the ‘truth’ and the ensemble mean.

5.3 Results

5.3.1 The 'Truth'

One advantage of the OSSE is that the 'truth' is available and the observation can also be extracted. Here we describe the 'true state' of both the weak and strong cases. In an extreme event such as TC, the ocean is strongly influenced by the wind forcing. The surface ocean currents respond to the TC forcing even when the centre is still far away (e.g. Glenn et al., 2016). This feature can also be observed in this idealised modelling. For instance, in the strong case, when the TC is 28 hours before landfall, the coastal surface currents are as high as 0.5 m/s (Fig. 5.2). This is a substantial change compared with the background ocean currents (0 m/s).

The Weak TC Case

In the weak case, the TC is initialised from an initial vortex (SST = 28.5°C, R_{max} = 50km, V_{max} = 30m/s) in the middle of the domain (x = 250, y = 200). The ocean is initialised from a steady state and the temperature and salinity profiles (Fig. 5.3) are extracted from the World Ocean Atlas (WOA) climatological dataset in the topical western Pacific (with SST of 28.5°C). The initial easterly background flow is set to 5.5 m/s and the actual average translation speed is 5.3 m/s. The TC develops (Fig. 5.4) as it moves towards the coastline. It reaches Category 3 stage with the maximum wind speed of 53 m/s, 15 hours after the initialisation and makes the landfall at Hour 52. The minimum pressure (946 hPa) occurs 18 hours after the initialisation then it starts to increase. We use the second day (Hour 24 to 48, i.e., 28 to 4 hours before landfall, illustrated by the vertical dashed line in Fig. 5.4) as the period of forecast, because some of the ensemble members make landfall earlier due to different translation speeds. During the period of forecast, the maximum wind speed in the 'true state' is around 45 m/s (Category 2) the size (radius of 18 m/s wind, R_{18}) is approximately 80 km.

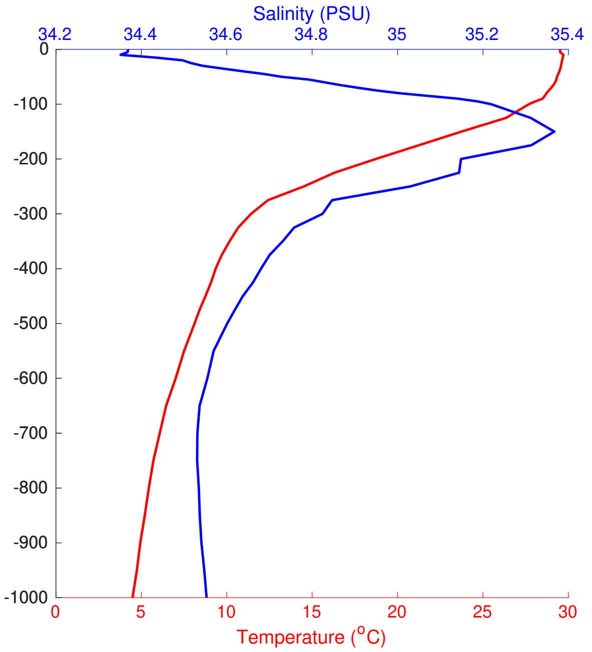

Figure 5.3 The vertical profiles of initial ocean temperature and salinity in the initial condition of the weak case.

The Strong TC Case

In the strong TC case, the TC is simulated in two phases. First, in a WRF-only model, the TC starts from a stronger and bigger initial vortex (SST = 33°C, R_{max} = 80km, V_{max} = 50m/s) located in the middle of the domain (x = 250, y =200). There is no background steering flow so the TC roughly maintains the initial location. It reaches Category 5 stage ($V_{max} = 75m/s$, $P_{min} = 890hPa$) in 3 days.

Then the WRF model is coupled with a ROMS model with a warmer temperature profile (Fig. 5.5) and an easterly steering flow of 6 m/s is added. The temperature is based on the WOA dataset but is increased in the top 100 m such that SST is 33 °C and T_{100m} is 32 °C. The changes between the ocean surface and 100m are linearly interpolated. The TC starts to move westward (with an average translation speed of 5.3 m/s) towards the coastline and makes landfall at Hour 52. The evolution is shown in Fig. 5.4. After the coupling, the TC starts to decline. Same as in the weak case,

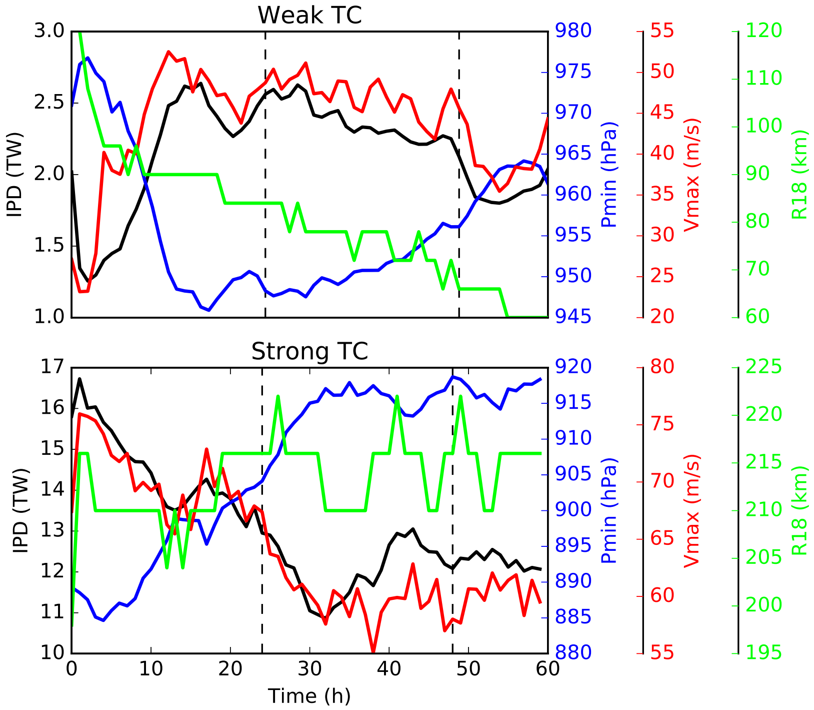

Figure 5.4 The time evolution from the initial condition (T=0) of IPD, P_{min}, V_{max} and R_{18} in the 'truth' of the weak and strong cases. The vertical dashed lines indicate the second day which is studied.

the period of Hour 24 to Hour 48 is studied. The maximum wind speed during this period is approximately 60 m/s (Category 4) and IPD is about 12 TW. The size of the strong TC is much larger than the weak one and maintains around 210 km during the second day.

5.3.2 The NoDA Run

The Ensemble Spread

It is important to have a reasonable spread in the initial ensembles for the data assimilation and forecast. As described above, the true atmospheric state was perturbed using the WRF-3DVAR package (Zhang et al., 2006, 2009) at Hour 12 after the initialisation and the perturbed state coupled with the ROMS model for 9 hours to generate the initial ensembles. The standard deviations of the ROMS and WRF model

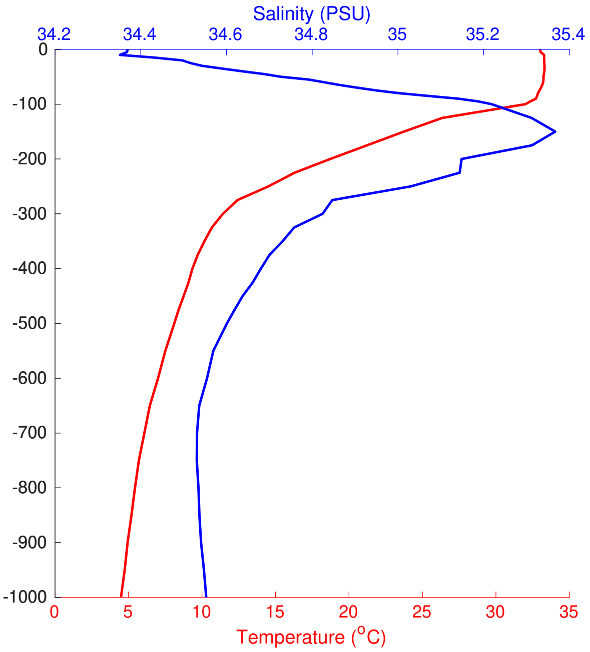

Figure 5.5 The vertical profiles of ocean temperature and salinity in the initial condition of the strong case.

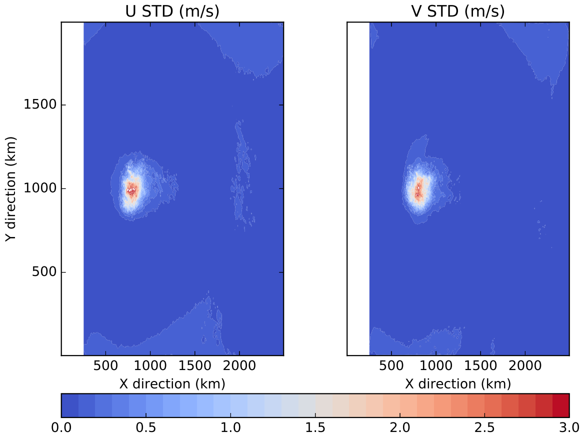

Figure 5.6 The standard deviation of surface u (left) and v (right) currents at Hour 24 (i.e., 28 hours before landfall) in the strong TC case.

states in the strong case are shown in Fig. 5.6 and Fig. 5.7. The maximum spread occurs near the centre of the cyclone, and is around 2.5 m/s for surface currents, 30 m/s for horizontal wind components and 20 hPa for surface pressure. In the weak TC case, the pattern is similar (figure not shown) but the values are smaller. The spread

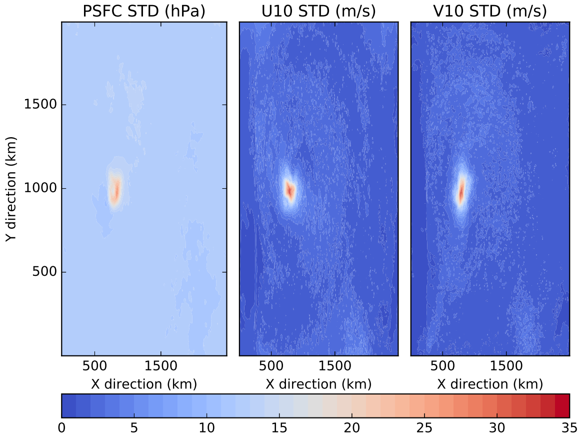

Figure 5.7 Same with Fig. 5.6, but for the surface pressure and 10 m wind speed.

is approximately 1.5 m/s for surface currents, 20 m/s for horizontal wind components and 15 hPa for surface pressure.

The Correlation

Forced by the strong wind stress of a tropical cyclone, the surface coastal currents change significantly ahead of the TC centre (e.g. Glenn et al., 2016) (Fig. 5.2). In the idealised swimming pool model in this study, the surface coastal currents and the TC location and intensity (IPD) are highly correlated (Fig. 5.8). When the TC centre is 26-hour (approximately 400 km) away from the coastline, the correlation between the currents and TC location is about 0.5 while that of the currents and IKE is about 0.3. As the cyclone moves toward the coastline, the correlation increases and the coefficients are as high as 0.5 for surface currents and IKE, and 0.7 for surface currents and TC location. The correlation in the weak case shows a similar pattern, but the value is lower (Fig. 5.9).

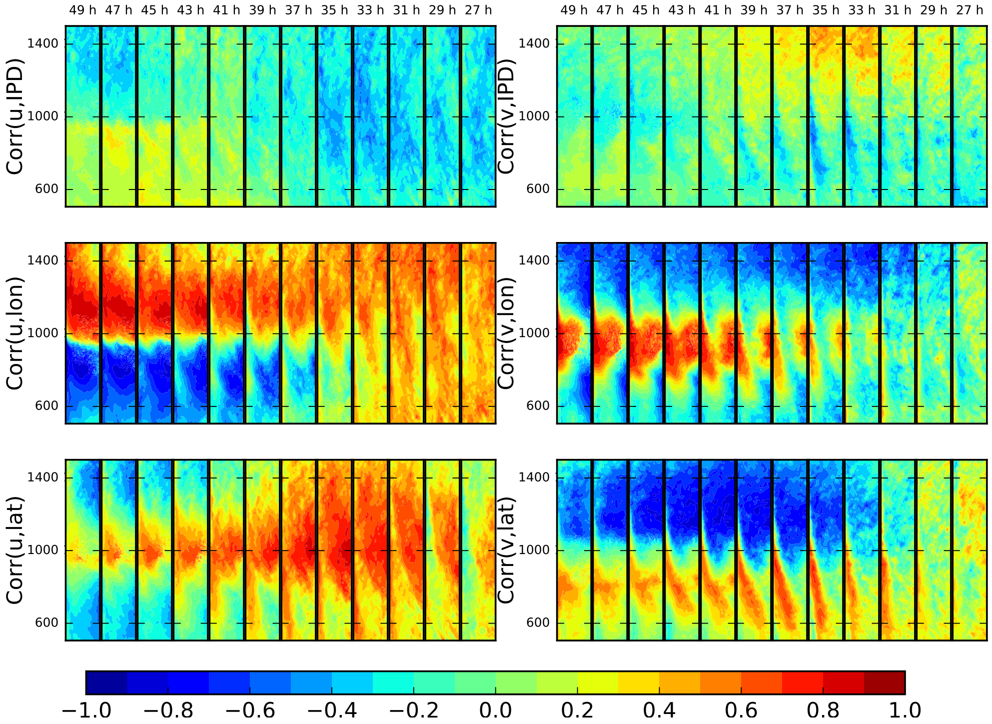

Figure 5.8 The spatial distribution of the Pearson correlation coefficients of the coastal currents in ROMS with IPD and longitude and latitude of the TC centre in the NoDA ensemble of the strong case at different times (h). The TC is moving to the left (westward). The x-axis is the from 5 to 200 km from the coast. The y-axis is the distance (km) in the y-direction.

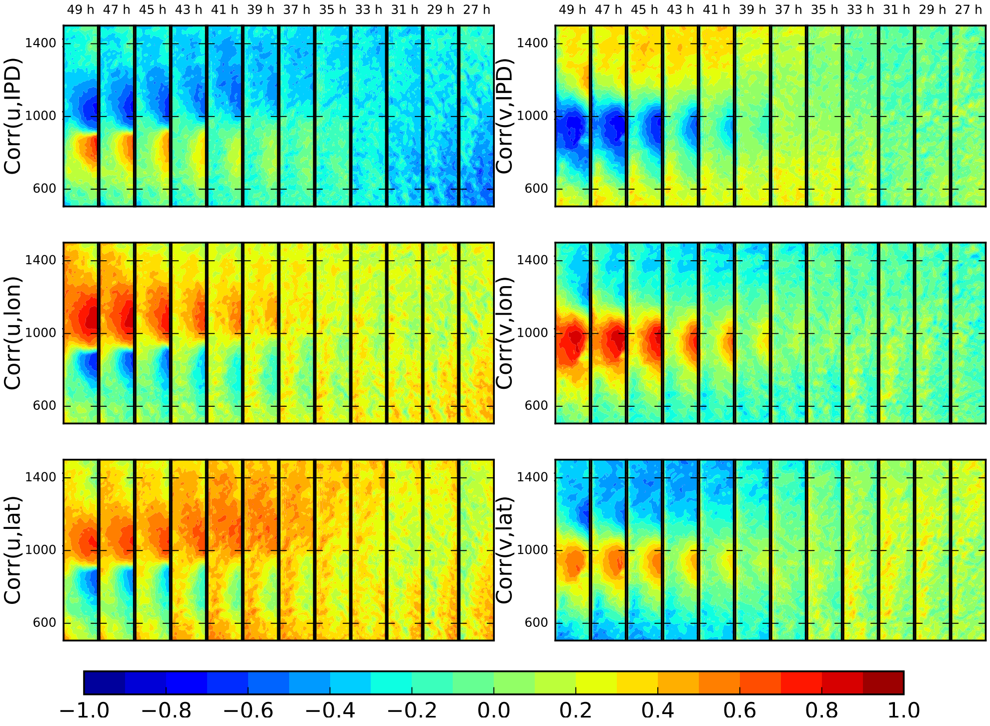

Figure 5.9 The same as Fig. 5.8, but for the weak TC case.

5.3.3 Vertical Localisation

The vertical localisation radius is usually determined by computing the error correlations between the variables in two domains(e.g. Smith et al., 2017). Here we take TC3 as an example, the correlation between the surface ocean currents and the vertical atmosphere temperature and wind profiles in the coastal region (Fig. 5.10) is high in the bottom. The correlation between ocean currents and u wind is higher (up to 0.8) and reach Level 15 to 20 (450 to 250 hPa). The correlation between other variables are weaker and constraint to the lower levels. For instance, the correlation between v currents and temperature is about 0.4 and is limited within the bottom 5 levels (940 hPa). It is also noteworthy that the correlation depends on the location and the distance to the TC. The correlation is weaker and more constraint to the bottom levels as the location is further to the TC. Therefore the vertical localistion scale of 5 levels is selected.

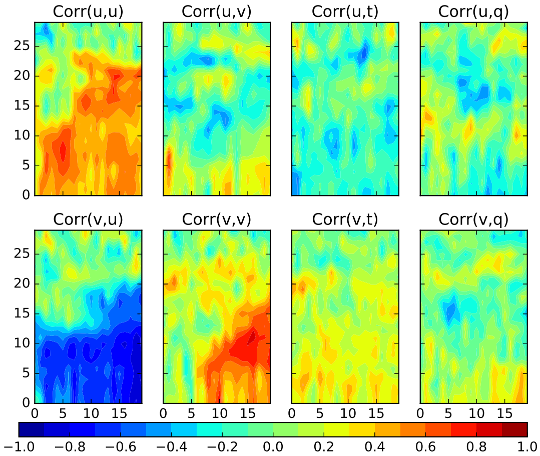

Figure 5.10 The error correlation coefficient between surface u (upper panel), v (lower panel) currents and the local atmosphere u, v, temperature (t), humidity (q) profiles. The correlation is computed at the edge of the observation region (x = 500 km, y = 1000 km). The y-axis is the vertical levels in WRF. The x-axis is time (h in the second day).

5.3.4 Sensitivity Test

The data assimilation systems are sensitive to several filter parameters, including the localisation radius, inflation factor and observation error. Here we first test the sensitivity in a set of 13-hour data assimilation experiments in the weak TC case to choose an optimum parameter combination. Because we are mainly interested in the effect of data assimilation on TC intensity, we evaluate the performance using IPD. Overall, the localisation radius of 700 km and the observation error of 10 cm/s are optimal choices, while the inflation factor makes little difference.

Localisation Radius

We first test the sensitivity of the system to the horizontal localisation radius. In this part, 3 localisation scales (350 km, 700 km and 1050 km) are tested with no inflation and the observation error is set to 10 cm/s. An ensemble size of 40 is used to expedite computation. The error of IPD (Fig. 5.11) suggests that the localisation scale plays an important role in the performance of the assimilation system. Overall, the radius of 700 km produces the best results, while the error with 350 km is the highest. The spatial pattern (figure not shown) suggests that although a too small localisation reduces the error close to the coast, the structures of the TCs are impaired. On the other hand, a too large radius makes less impact on the TC simulation. Therefore 750 km is an optimal choice.

Observation Error

In this part, 3 observation errors (5 cm/s, 10 cm/s and 20 cm/s) are tested with the localisation radius of 700 km and no inflation. An additional value (2 cm/s) is also tested but some of the ensemble members blow up after 2 hours integration. Smaller error value (5 cm/s) produces better results for some of the ensemble members but inhibits the TC structure for other members, therefore the average error is higher. On

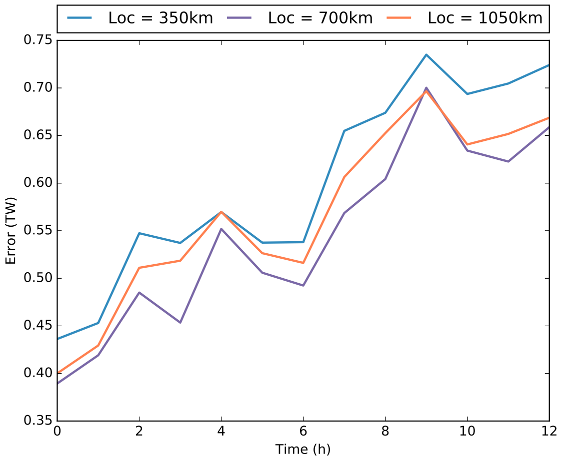

Figure 5.11 The time evolution of the error (difference between the 'truth' and the ensemble mean) of IPD during the 13-hour sensitivity tests with the localisation scales of 350, 700 and 1050 km. No inflation factor is used in these tests and the observation error is 10 cm/s.

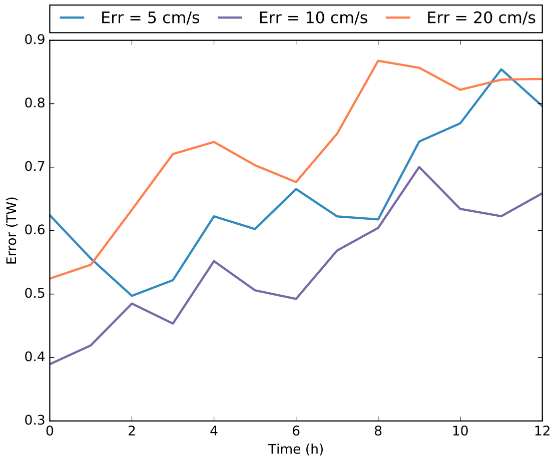

Figure 5.12 Same with Fig. 5.11, but for the tests with observation error of 5, 10 and 20 cm/s. No inflation factor is used in these tests and the localisation radius is 700 km.

the other hand, a bigger error (20 cm/s) does not improve the simulation. The overall performance suggests that 10 cm/s is an optimal value. This is consistent with the typical observation error of HF radars (Paduan and Washburn, 2013).

Inflation Factor

In this part, 4 inflation factors (1, 1.1, 2 and 5) are tested. The inflation does not change the data assimilation results significantly (Fig. 5.13). The error with higher inflation is larger. The problem of high inflation is similar with that of low observation error, that the TC structure is impeded although the simulation of coastal currents is improved (figure not shown). This feature is different with some other systems in which the observation is not limited within a relatively small region. Using an uncoupled WRF model, Zhang et al. (2009) proposed a different inflation technique in which the analysis is a combination of posterior and prior states. This technique could reduce the imbalance but limits the effect of data assimilation. In the forecast experiment of this study no inflation is used.

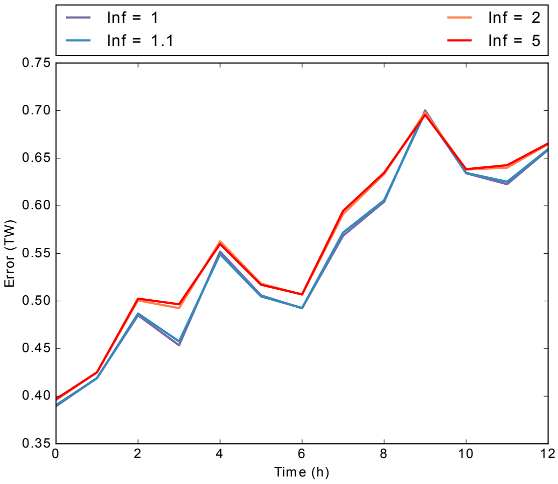

Figure 5.13 Same with Fig. 5.11, but for the tests with inflation factor of 1 (no inflation), 1.1, 2 and 5. The localisation radius is 700 km and the observation error is 10 cm/s in these tests.

5.3.5 The Data Assimilation and Forecast Experiments

In the data assimilation and forecast experiments, we first carry out three cycles of hourly data assimilation, then the posterior state was used as initial conditions for the following 24- and 12-hour forecasts.

For the 24-hour forecast (Fig. 5.14), which is important for the decision makers, the error of intensity reduces dramatically in the strong case. For instance, the error of V_{max} reduces by over 50% (from 7.1 m/s to 3.5 m/s). For the weak case, the error also reduces but the magnitude is smaller (20%, from 1.4 m/s to 1.1 m/s). The results are similar for IPD and the improvement in the strong case is 50% (from 1 to 0.5 TW), while in the weak case it improves 30% (from 0.15 to 0.1 TW). As for P_{min}, the error in the strong case reduces by about 15% (21 to 18 hPa) while in the weak case the improvement is marginal. However, the track forecast improves more for the weak TC, in which the error decreases 30% from 15 km to 10 km, while in the strong TC case the track forecast does not improve. During the data assimilation stage, when the TC is 28 hours away from the coastline, the observations are far (over 300 km) from the TC. Therefore the assimilation mainly affects the steering flow and track for the weak TC but can affect the structure and intensity of the strong TC.

In the 12-hour forecast (Fig. 5.15), the maximum wind speeds do not change much even when the coastal currents are assimilated. However, the error of IPD forecast decreases by over 50% for the strong TC, indicating the structure is much better predicted. The reason is that, when the cyclone is 16 hours (approximately 300 km) away from the coastline, the strong TC (with R_{18} of about 210 km) covers much of the ocean currents observation region and the localisation radius. Thus the TC is highly correlated with the coastal currents (Fig. 5.8) and assimilation has a larger impact. As for the weak TC, since the radius is much smaller (R_{18} is about 65 km), the size and intensity have a smaller effect on coastal currents (Fig. 5.8).

5.4 Discussion and Conclusion

It is well known that the coastal surface currents respond to the approaching cyclones and this response can be monitored by HF radars (e.g. Glenn et al., 2016). However, this potentially useful observation is not assimilated in TC forecast systems. In this study

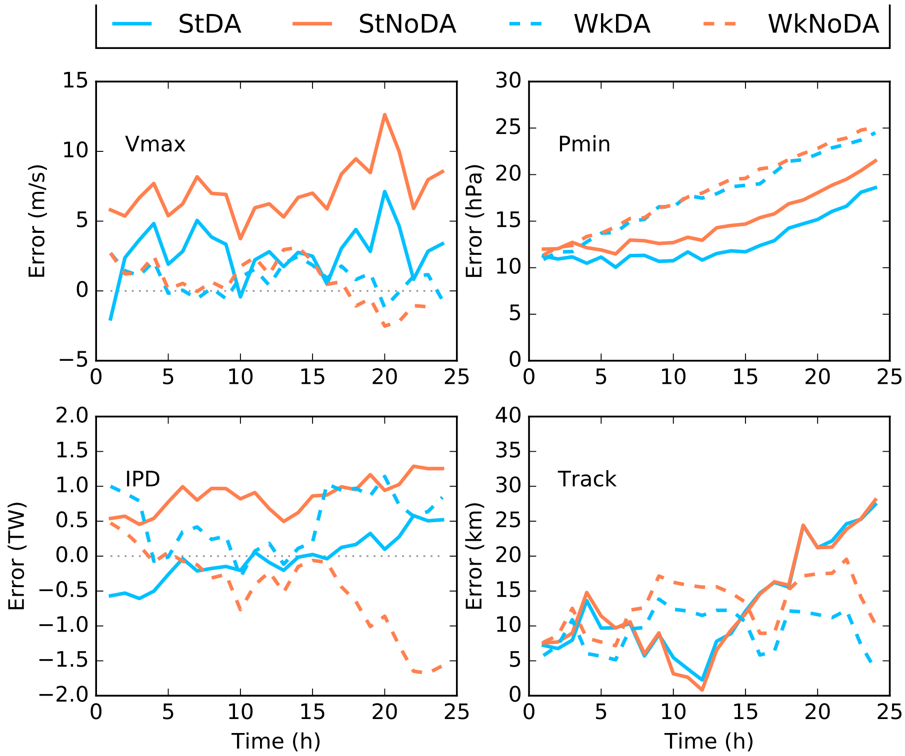

Figure 5.14 The temporal evolution of the error (difference between the 'truth' and the ensemble mean) of V_{max}, P_{min}, IPD and tracks during the 24-hour forecast for DA and NoDA experiments in the strong (St) and weak (Wk) cases.

we develop a strongly-coupled data assimilation system using the Ensemble Adjustment Kalman Filter (EAKF) and the Coupled-Ocean-Atmosphere-Wave-Sediment Transport modeling system (COAWST) and assimilate synthetic surface coastal currents in an idealized Observing System Simulation Experiment (OSSE). The effects are evaluated in both weak (Category 2) and strong (Category 4) TC cases. By performing strongly-coupled data assimilation, the ocean observations update the atmosphere state directly via the cross-covariance matrix and leads to substantial benefit for TC forecasts.

The improvements of the 24-hour intensity (V_{max} and IPD) forecast are as high as 50% for the strong TC, and 20-30% for the weak one. There is also benefit on the track forecast (30%) for the weak TC, but it is noteworthy that in these idealized experiments, the errors of TC tracks (order of 10 km) are much lower than in the real-time forecasts (order of 50 km (e.g. Yamaguchi et al., 2017)).

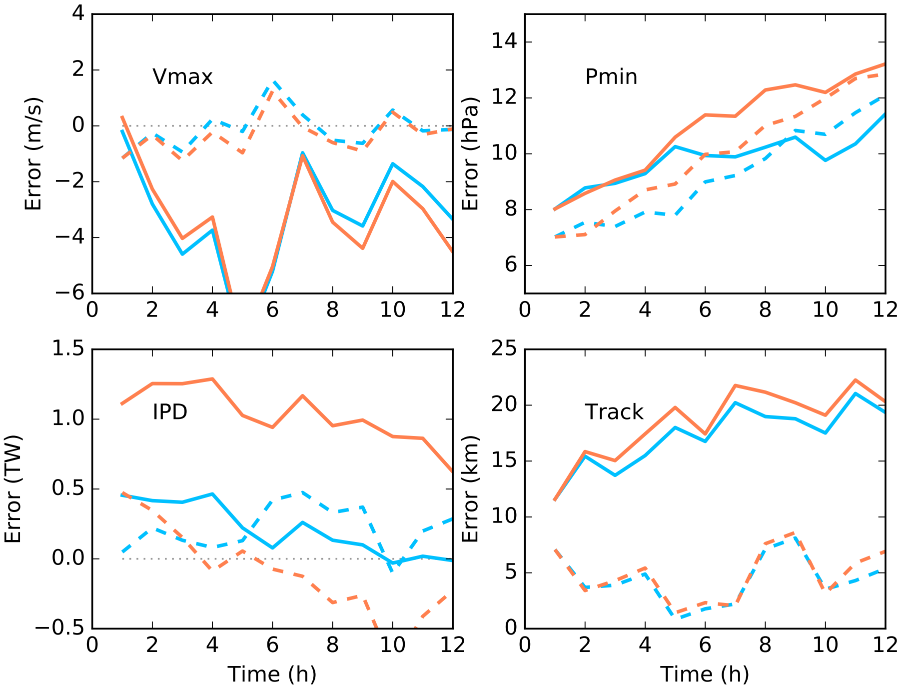

Figure 5.15 Same with Fig. 5.14, but for the 12-hour forecast.

The error of V_{max} reduces by 3.6 m/s for the strong TC, which is of the same order of the average error in real-time forecasts of around 5 m/s (e.g. Goni et al., 2017). In addition, HF radars can produce accurate measurements during TC landfall while much of other ocean observing systems (e.g., Argo floats and gliders) are usually unavailable or impacted. Halliwell et al. (2017a,b) pointed out that assimilating standard ocean observations (e.g., sea surface temperature and sea level anomaly) produced a better ocean state and could potentially improve TC forecast but the actual benefit was not demonstrated. In a real-case study of Hurricane Gonzalo (2014, Category 4 with V_{max} over 60 m/s), Dong et al. (2017) found that underwater glider observations had no effect on the TC forecast. However, the potential benefit of HF radar is demonstrated here.

The results show that the assimilation of coastal currents can improve the structure of the strong TC and the steering flow, thus it improves the forecast of the intensity for the strong (and large) TCs and the tracks for the weak (and small) ones. However, more studies are needed to estimate the influence of other factors in real settings, including the background ocean currents, combinations of different observations, the bathymetry and the translation speed and size of the TC.

Ensemble data assimilation can generate the cross-domain background error covariance automatically and the implementation of strongly-coupled data assimilation is feasible. In addition, unlike other observations such as airborne profilers which need to be deployed, the typical HF radar network is already immediately available to gather observations (e.g. Paduan and Washburn, 2013). This work suggests potential benefits of assimilating coastal current observations in coupled forecast systems.

Chapter 6

Conclusion and Future Work

6.1 Conclusion

Data assimilation provides an objective criterion for fusing observations with numerical models to produce an estimate of the true state, which is a crucial step in providing an optimal initial condition for atmosphere and ocean forecasting. Using the algorithms provided by the Data Assimilation Research Testbed (DART), two ensemble-based data assimilation systems have been developed in this thesis, one being a regional ocean system, the other being a coupled tropical cyclone (TC) system.

The regional ocean system consists of DART and the Regional Ocean Modeling System (ROMS). The system is applied to the South Australian Sea with 10 km resolution, and the sea surface temperature (SST) and the sea surface height (SSH) are assimilated. The errors of SST and SSH both reduce in the analysis. However, assimilating SST deteriorates the overall estimation of SSH, especially in the winter season. On the other hand, in the SSH assimilation experiment, the distribution of SST is similar to the control run. The assimilation of both SST and SSH is similar to just SST. One possible reason is that the number of SST observations is much higher than SSH.

The spurious waves caused by data assimilation usually degenerate the performance of the data assimilation and forecast. We add a physical balance operator, including the temperature-salinity, hydrostatic and geostrophic balance, to this regional ocean system, to reduce the spurious waves. The effect is studied in both an idealised shallow water model and the South Australian Sea system. For the shallow water model, the balance operator decreases the error of sea surface height and velocities. It is also shown that the benefit of the balance operator increases as the amplitude of SSH and wind stress increase. For the South Australian Sea system, the estimations of both SSH and temperature are improved, especially for the forecast, indicating a balanced posterior state is important. The balance operator improves the estimation of ocean currents significantly, assimilating SSH with the balance operator produces ocean currents that are the most comparable with OSCAR dataset. The error of u and v is reduced by 27% and 23% compared with the original data assimilation, and 40% to 50% compared with the control run. The comparison with drifter derived surface currents shows similar results. The error of temperature profiles against Argo data suggests assimilating SSH with the balance operator produces the most realistic subsurface temperature and salinity. A case study with a storm affecting this region shows that under high wind forcing condition the the balance operator reduces the ageostrophic currents significantly in both analysis and forecast. The results in all experiments performed in this thesis suggest that the balance operator may be useful to implement generally in ensemble based regional ocean data assimilation systems.

The TC system is a strongly-coupled data assimilation system, which consists of DART, ROMS and the Weather Research and Forecasting (WRF) model. High-frequency (HF) radars can provide high-resolution and frequent surface ocean currents observations during the TC landfall. The synthetic observations are assimilated using idealised Observing System Simulation Experiments, and the forecast performances for weak (Category 2) and strong (Category 4) TCs are examined. Assimilating coastal surface currents improves the 24-hour forecasts of both intensity and track. For the strong case, the errors of the maximum wind speed (V_{max}) and the integrated power dissipation (IPD) forecast reduce up to 50%. For the weak case, the improvements in V_{max} and IPD forecast are lower (20%), but the track forecast improves 30%. These improvements are similar to the magnitude of the current operational TC forecast error, so that assimilating HF radar observations could be a substantial benefit.

6.2 Future Work

This thesis uses a physical balance operator to reduce the spurious waves in a regional ocean data assimilation system. In Chapter 5 a coupled data assimilation system is developed, this brings up the following question, 'is there imbalance in the coupled system and, if so, how to reduce it?' As shown in Chapter 4, the imbalance between the atmospheric forcing and the ocean circulation could be amplified by the data assimilation process and is a source of the spurious waves. Some studies have shown that the coupled systems could also suffer from the spurious waves, since the ensemble size is usually smaller and the model size is bigger than the uncoupled model (A. Karspeck, personal communication). The balance between the atmosphere and the ocean components can be studied using this coupled system. This would require the development of a new balance operator, to include both oceanic and atmospheric variables (such as velocity, temperature, humidity and pressure). However, the physical relationship across the air-sea interface is not clear and statistical approaches (e.g., the linear regression between air temperature and ocean temperature) may be needed.

For the uncoupled ocean model, as the model resolution increases, the balances used in this thesis may breakdown (e.g. Vetra-Carvalho et al., 2012) and the balance operator needs to be modified. Such efforts have been taken for the atmospheric models (e.g. Honda et al., 2006) but have not been reported for the ocean models. Future work is needed to investigate the balance for high-resolution model and design new approaches/balance operators. In addition, the hybrid data assimilation systems have been developed (e.g. Wang et al., 2008a,b, 2013) recently and implemented operationally (e.g. Clayton et al., 2013) as they combine the advantages of both variational and sequential approaches (e.g. Hamill and Snyder, 2000; Lorenc, 2003b). The application of the balance operator in the hybrid systems is also interesting. In the hybrid systems, the balance operator should be applied simultaneously to the variational and ensemble components, but the relative contributions of each component with the balance operator are yet to be explored. A 4DVAR algorithm has already been supported by ROMS (Moore et al., 2011a,b,c) and a ROMS hybrid data assimilation system could be developed with which the balance issue can be studied.

The forecasts of TC intensity and tracks using an idealised case in Chapter 5. However, more studies are needed to estimate the influence of other factors in real settings, including the background ocean currents, combinations of different observations, the bathymetry and the translation speed and size of the TC. Future work is scheduled to study the forecast skill using a regional coupled model for the South China Sea. The proposed Observing System Simulated Experiments (OSSEs) include assimilation of aircraft drop-sound real observations and synthetic ocean surface currents. New high-Frequency radar could be deployed depending on the results of the OSSEs.

Acknowledgements

I would like to thank Ralf Toumi for all his supervision, guidance and support during the past three and half years, and Arnaud Czaja and Amos Lawless for examining this thesis. I would also like to thank Ibrahim Hoteit and Andrew Moore for their comments and suggestions, and Rossella Arcucci, Luke Phillipson, Cesar Quilodran and other members of the group for many interesting discussions. Finally, I would like to express my gratitude to my wife and my parents for their faith and support, and Yaya for being a good baby during most of the time.

This PhD project is sponsored by the China Scholarship Council (CSC) - Imperial College London Scholarship Program.

Bibliography

Anderson, J., Hoar, T., Raeder, K., Liu, H., Collins, N., Torn, R., and Avellano, A. (2009). The data assimilation research testbed a community facility. *Bulletin of the American Meteorological Society*, 90(9):1283–1296.

Anderson, J. L. (2001). An Ensemble Adjustment Kalman Filter for Data Assimilation. *Monthly Weather Review*, 129:2884–2903.

Anderson, J. L. (2007). An adaptive covariance inflation error correction algorithm for ensemble filters. *Tellus A*, 59(2):210–224.

Anderson, J. L. (2009). Spatially and temporally varying adaptive covariance inflation for ensemble filters. *Tellus, Series A: Dynamic Meteorology and Oceanography*, 61 A(1):72–83.

Anderson, J. L. and Anderson, S. L. (1999). A Monte Carlo Implementation of the Nonlinear Filtering Problem to Produce Ensemble Assimilations and Forecasts. *Monthly Weather Review*, 127(12):2741–2758.

Anderson, J. L. and Collins, N. (2007). Scalable implementations of ensemble filter algorithms for data assimilation. *Journal of Atmospheric and Oceanic Technology*, 24(8):1452–1463.

Balmaseda, M. A., Mogensen, K., and Weaver, A. T. (2013). Evaluation of the ECMWF ocean reanalysis system ORAS4. *Quarterly Journal of the Royal Meteorological Society*, 139(674):1132–1161.

Barker, D. M., Huang, W., Guo, Y.-R., Bourgeois, A. J., and Xiao, Q. N. (2004). A Three-Dimensional Variational Data Assimilation System for MM5: Implementation and Initial Results. *Monthly Weather Review*, 132(4):897–914.

Bauer, P., Thorpe, A., and Brunet, G. (2015). The quiet revolution of numerical weather prediction. *Nature*, 525(7567):47–55.

Bell, M., Lefèbvre, M., Le Traon, P.-Y., Smith, N., and Wilmer-Becker, K. (2009). GODAE: The Global Ocean Data Assimilation Experiment. *Oceanography*, 22(3):14–21.

Bocquet, M. and Sakov, P. (2014). An iterative ensemble Kalman smoother. *Quarterly Journal of the Royal Meteorological Society*, 140(682):1521–1535.

Bonjean, F. and Lagerloef, G. S. E. (2002). Diagnostic model and analysis of the surface currents in the tropical Pacific Ocean. *Journal of Physical Oceanography*, 32(10):2938–2954.

Booij, N., Ris, R. C., and Holthuijsen, L. H. (1999). A third-generation wave model for coastal regions: 1. Model description and validation. *Journal of Geophysical Research*, 104(C4):7649–7666.

Bruneau, N., Toumi, R., and Wang, S. (2018). Impact of wave whitecapping on land falling tropical cyclones. *Scientific Reports*, 8(1):652.

Buehner, M. and Shlyaeva, A. (2015). Scale-dependent background-error covariance localisation. *Tellus A*, 67:1–17.

Cangialosi, J. P. and Franklin, J. L. (2017). National Hurricane Center 2016 Atlantic Hurricane Season. Technical Report February.

Clayton, A. M., Lorenc, A. C., and Barker, D. M. (2013). Operational implementation of a hybrid ensemble/4D-Var global data assimilation system at the Met Office. *Quarterly Journal of the Royal Meteorological Society*, 139(675):1445–1461.

Cohn, S. E. and Parrish, D. F. (1991). The behavior of forecast error covariances for a Kalman filter in two dimensions.

Corsaro, C. M. and Toumi, R. (2017). A self-weakening mechanism for tropical cyclones. *Quarterly Journal of the Royal Meteorological Society*, 143(707):2585–2599.

Counillon, F. and Bertino, L. (2009). Ensemble Optimal Interpolation: Multivariate properties in the Gulf of Mexico. *Tellus, Series A: Dynamic Meteorology and Oceanography*, 61(2):296–308.

Courtier, P. and Talagrand, O. (1990). Variational assimilation of meteorological observations with the direct and adjoint shallow-water equations. *Tellus A*, 42(5):531–549.

Daley, R. (1991). *Atmospheric Data Analysis*. Cambridge University Press.

Dohan, K. and Maximenko, N. (2010). Monitoring Ocean Currents with Satellite Sensors. *Oceanography*, 23(4):94–103.

Dombrowsky, E., Bertino, L., Brassington, G., Chassignet, E., Davidson, F., Hurlburt, H., Kamachi, M., Lee, T., Martin, M., Mei, S., and Tonani, M. (2009). GODAE Systems in Operation. *Oceanography*, 22(3):80–95.

Dong, J., Domingues, R., Goni, G., Halliwell, G., Kim, H.-S., Lee, S.-K., Mehari, M., Bringas, F., Morell, J., and Pomales, L. (2017). Impact of Assimilating Underwater Glider Data on Hurricane Gonzalo (2014) Forecasts. *Weather and Forecasting*, 32(3):1143–1159.

Dudhia, J. (1989). Numerical Study of Convection Observed during the Winter Monsoon Experiment Using a Mesoscale Two-Dimensional Model.

Emanuel, K. (2001). Contribution of tropical cyclones to meridional heat transport by the oceans. *Journal of Geophysical Research: Atmospheres*, 106(D14):14771–14781.

Emanuel, K. (2005). Increasing destructiveness of tropical cyclones over the past 30 years. *Nature*, 436(7051):686–688.

Emanuel, K. A. (1986). An Air-Sea Interaction Theory for Tropical Cyclones. Part I: Steady-State Maintenance.

Emanuel, K. A. (1987). The dependence of hurricane intensity on climate. *Nature*, 326(6112):483–485.

Emerick, A. and Reynolds, A. (2011). Combining sensitivities and prior information for covariance localization in the ensemble Kalman filter for petroleum reservoir applications. *Computational Geosciences*, 15(2):251–269.

Evensen, G. (1994). Sequential data assimilation with a nonlinear quasi-geostrophic model using Monte Carlo methods to forecast error statistics. *Journal of Geophysical Research*, 99(C5):10143.

Fowler, A. M. and Lawless, A. S. (2016). An Idealized Study of Coupled Atmosphere–Ocean 4D-Var in the Presence of Model Error. *Monthly Weather Review*, 144(10):4007–4030.

Gaspari, G. and Cohn, S. E. (1999). Construction of correlation functions in two and three dimensions. *Quarterly Journal of the Royal Meteorological Society*, 125(554):723–757.

Gill, A. E. (1982). *Atmosphere-ocean Dynamics, Volume 30.* Academic Press.

Glenn, S. M., Miles, T. N., Seroka, G. N., Xu, Y., Forney, R. K., Yu, F., Roarty, H., Schofield, O., and Kohut, J. (2016). Stratified coastal ocean interactions with tropical cyclones. *Nature Communications*, 7(May 2015):10887.

Goni, G., Todd, R., Jayne, S., Halliwell, G., Glenn, S., Dong, J., Curry, R., Domingues, R., Bringas, F., Centurioni, L., DiMarco, S., Miles, T., Morell, J., Pomales, L., Kim, H.-S., Robbins, P., Gawarkiewicz, G., Wilkin, J., Heiderich, J., Baltes, B., Cione, J., Seroka, G., Knee, K., and Sanabia, E. (2017). Autonomous and Lagrangian Ocean Observations for Atlantic Tropical Cyclone Studies and Forecasts. *Oceanography*, 30(2):92–103.

Greybush, S. J., Kalnay, E., Miyoshi, T., Ide, K., and Hunt, B. R. (2011). Balance and Ensemble Kalman Filter Localization Techniques. *Monthly Weather Review*, 139(2):511–522.

Hacker, J. P. and Lei, L. (2015). Multivariate Ensemble Sensitivity with Localization. *Monthly Weather Review*, 143(6):2013–2027.

Haidvogel, D. B., Arango, H., Budgell, W. P., Cornuelle, B. D., Curchitser, E., Di Lorenzo, E., Fennel, K., Geyer, W. R., Hermann, a. J., Lanerolle, L., Levin, J., McWilliams, J. C., Miller, a. J., Moore, a. M., Powell, T. M., Shchepetkin, a. F., Sherwood, C. R., Signell, R. P., Warner, J. C., and Wilkin, J. (2008). Ocean forecasting in terrain-following coordinates: Formulation and skill assessment of the Regional Ocean Modeling System. *Journal of Computational Physics*, 227(7):3595–3624.

Haidvogel, D. B., Arango, H. G., Hedstrom, K., Beckmann, A., Malanotte-Rizzoli, P., and Shchepetkin, A. F. (2000). Model evaluation experiments in the North Atlantic Basin: Simulations in nonlinear terrain-following coordinates. *Dynamics of Atmospheres and Oceans*, 32(3-4):239–281.

Halliwell, G. R., Mehari, M., Shay, L. K., Kourafalou, V. H., Kang, H., Kim, H.-S., Dong, J., and Atlas, R. (2017a). OSSE quantitative assessment of rapid-response prestorm ocean surveys to improve coupled tropical cyclone prediction. *Journal of Geophysical Research: Oceans*, 122(7):5729–5748.

Halliwell, G. R., Mehari, M. F., Le Hénaff, M., Kourafalou, V. H., Androulidakis, I. S., Kang, H. S., and Atlas, R. (2017b). North Atlantic Ocean OSSE system: Evaluation of operational ocean observing system components and supplemental seasonal observations for potentially improving tropical cyclone prediction in coupled systems. *Journal of Operational Oceanography*, 10(2):154–175.

Hamill, T. M. and Snyder, C. (2000). A Hybrid Ensemble Kalman Filter–3D Variational Analysis Scheme. *Monthly Weather Review*, 128(8):2905–2919.

Hamill, T. M., Whitaker, J. S., and Snyder, C. (2001). Distance-Dependent Filtering of Background Error Covariance Estimates in an Ensemble Kalman Filter. *Monthly Weather Review*, 129(11):2776–2790.

Honda, Y., Nishijima, M., Koizumi, K., Ohta, Y., Tamiya, K., Kawabata, T., and Tsuyuki, T. (2006). A pre-operational variational data assimilation system for a non-hydrostatic model at the Japan Meteorological Agency: Formulation and preliminary results. *Quarterly Journal of the Royal Meteorological Society*, 131(613):3465–3475.

Hong, S. and Lim, J. (2006). The WRF single-moment 6-class microphysics scheme (WSM6).

Hoteit, I., Hoar, T., Gopalakrishnan, G., Collins, N., Anderson, J., Cornuelle, B., Köhl, A., and Heimbach, P. (2013). A MITgcm/DART ensemble analysis and prediction system with application to the Gulf of Mexico. *Dynamics of Atmospheres and Oceans*, 63:1–23.

Hoteit, I., Pham, D.-T., Triantafyllou, G., and Korres, G. (2008). A New Approximate Solution of the Optimal Nonlinear Filter for Data Assimilation in Meteorology and Oceanography. *Monthly Weather Review*, 136(1):317–334.

Houtekamer, P. L. and Mitchell, H. L. (1998). Data assimilation using an ensemble Kalman filter technique. *Monthly Weather Review*, 126(3):796–811.

Houtekamer, P. L. and Mitchell, H. L. (2001). A Sequential Ensemble Kalman Filter for Atmospheric Data Assimilation. *Monthly Weather Review*, 129(1):123–137.

Hu, A. and Meehl, G. A. (2009). Effect of the Atlantic hurricanes on the oceanic meridional overturning circulation and heat transport. *Geophysical Research Letters*, 36(3):1–6.

Ito, K., Kuroda, T., Saito, K., and Wada, A. (2015). Forecasting a Large Number of Tropical Cyclone Intensities around Japan Using a High-Resolution Atmosphere–Ocean Coupled Model. *Wea. Forecasting*, 30(3):793–808.

Jackett, D. R. and Mcdougall, T. J. (1995). Minimal Adjustment of Hydrographic Profiles to Achieve Static Stability.

Jacobs, G. A., Bartels, B. P., Bogucki, D. J., Beron-Vera, F. J., Chen, S. S., Coelho, E. F., Curcic, M., Griffa, A., Gough, M., Haus, B. K., Haza, A. C., Helber, R. W., Hogan, P. J., Huntley, H. S., Iskandarani, M., Judt, F., Kirwan, A. D., Laxague, N., Valle-Levinson, A., Lipphardt, B. L., J. Mariano, A., Ngodock, H. E., Novelli, G., Olascoaga, M. J., Özgökmen, T. M., Poje, A. C., Reniers, A. J. H. M., Rowley, C. D., Ryan, E. H., Smith, S. R., Spence, P. L., Thoppil, P. G., and Wei, M. (2014). Data assimilation considerations for improved ocean predictability during the Gulf of Mexico Grand Lagrangian Deployment (GLAD). *Ocean Modelling*, 83:98–117.

Janjić, Z. I. (1994). The Step-Mountain Eta Coordinate Model: Further Developments of the Convection, Viscous Sublayer, and Turbulence Closure Schemes.

Jones, A. C., Haywood, J. M., Dunstone, N., Emanuel, K., Hawcroft, M. K., Hodges, K. I., and Jones, A. (2017). Impacts of hemispheric solar geoengineering on tropical cyclone frequency. *Nature Communications*, 8(1):1382.

Jones, P. W. (1998). A User ' s Guide for SCRIP : A S pherical C oordinate R emapping and I nterpolation P ackage. Technical report, Los Alamos National Laboratory.

Jordan, C. L. (1958). Mean Soundings for the West Indies Area.

Karspeck, A. R., Yeager, S., Danabasoglu, G., Hoar, T., Collins, N., Raeder, K., Anderson, J., and Tribbia, J. (2013). An Ensemble Adjustment Kalman Filter for the CCSM4 Ocean Component. *Journal of Climate*, 26(19):7392–7413.

Kepert, J. D. (2009). Covariance localisation and balance in an Ensemble Kalman Filter. *Quarterly Journal of the Royal Meteorological Society*, 135(642):1157–1176.

Knutson, T. R., McBride, J. L., Chan, J., Emanuel, K., Holland, G., Landsea, C., Held, I., Kossin, J. P., Srivastava, A. K., and Sugi, M. (2010). Tropical cyclones and climate change. *Nature Geoscience*, 3(3):157–163.

Kuo, A. and Polvani, L. (1997). Time-dependent fully nonlinear geostrophic adjustment. *Journal of physical oceanography*, 27(Stoker 1958):1614–1634.

Kurapov, A. L., Foley, D., Strub, P. T., Egbert, G. D., and Allen, J. S. (2011). Variational assimilation of satellite observations in a coastal ocean model off Oregon. *Journal of Geophysical Research: Oceans*, 116(5):1–19.

Lahoz, W. a. and Schneider, P. (2014). Data assimilation: making sense of Earth Observation. *Frontiers in Environmental Science*, 2(May):1–28.

Large, W. G. and Yeager, S. G. (2009). The global climatology of an interannually varying air - Sea flux data set. *Climate Dynamics*, 33(2-3):341–364.

Larson, J., Jacob, R., and Ong, E. (2005). The Model Coupling Toolkit: A New Fortran90 Toolkit for Building Multiphysics Parallel Coupled Models. *The International Journal of High Performance Computing Applications*, 19(3):277–292.

Li, R. C. Y., Zhou, W., Shun, C. M., and Lee, T. C. (2017). Change in Destructiveness of Landfalling Tropical Cyclones over China in Recent Decades. *Journal of Climate*, 30(9):3367–3379.

Li, Y. and Toumi, R. (2017). A balanced Kalman filter ocean data assimilation system with application to the South Australian Sea. *Ocean Modelling*, 116:159–172.

Li, Z., Chao, Y., McWilliams, J. C., and Ide, K. (2008). A Three-Dimensional Variational Data Assimilation Scheme for the Regional Ocean Modeling System. *Journal of Atmospheric and Oceanic Technology*, 25(11):2074–2090.

Liu, H., Anderson, J., and Kuo, Y.-H. (2012). Improved Analyses and Forecasts of Hurricane Ernesto's Genesis Using Radio Occultation Data in an Ensemble Filter Assimilation System. *Monthly Weather Review*, 140(1):151–166.

Lorenc, A. C. (2003a). Modelling of error covariances by 4D-Var data assimilation. *Quarterly Journal of the Royal Meteorological Society*, 129(595):3167–3182.

Lorenc, A. C. (2003b). The potential of the ensemble Kalman filter for NWP—a comparison with 4D-Var. *Quarterly Journal of the Royal Meteorological Society*, 129(595):3183–3203.

Lumpkin, R. and Pazos, M. (2007). Measuring surface currents with Surface Velocity Program drifters: the instrument, its data, and some recent results. In Griffa, A., Kirwan, Jr., A. D., Mariano, A. J., Özgökmen, T., and Rossby, H. T., editors, *Lagrangian Analysis and Prediction of Coastal and Ocean Dynamics*, chapter 2. Cambridge University Press.

Lyard, F., Lefevre, F., Letellier, T., and Francis, O. (2006). Modelling the global ocean tides: modern insights from FES2004. *Ocean Dynamics*, 56(5-6):394–415.

Lynch, P. (2008). The origins of computer weather prediction and climate modeling. *Journal of Computational Physics*, 227(7):3431–3444.

Mainelli, M., DeMaria, M., Shay, L. K., and Goni, G. (2008). Application of Oceanic Heat Content Estimation to Operational Forecasting of Recent Atlantic Category 5 Hurricanes. *Weather and Forecasting*, 23(1):3–16.

Mendelsohn, R., Emanuel, K., Chonabayashi, S., and Bakkensen, L. (2012). The impact of climate change on global tropical cyclone damage. *Nature Climate Change*, 2(3):205–209.

Metzger, E., Smedstad, O. M., Thoppil, P. G., Hurlburt, H. E., Cummings, J. A., Wallcraft, A. J., Zamudio, L., Franklin, D. S., Posey, P. G., Phelps, M. W., Hogan, P. J., Bub, F. L., and Dehaan, C. J. (2014). US Navy Operational Global Ocean and Arctic Ice Prediction Systems. *Oceanography*, 27(3):32–43.

Middleton, J. F. and Bye, J. a. T. (2007). A review of the shelf-slope circulation along Australia's southern shelves: Cape Leeuwin to Portland. *Progress in Oceanography*, 75(1):1–41.

Milman, O. (2015). BP oil spill in Great Australian Bight would be catastrophic, modelling shows | Environment | The Guardian.

Mitchell, H. L., Houtekamer, P. L., and Pellerin, G. (2002). Ensemble Size, Balance, and Model-Error Representation in an Ensemble Kalman Filter*. *Monthly Weather Review*, 130(11):2791–2808.

Miyoshi, T., Kondo, K., and Imamura, T. (2014). The 10,240-member ensemble Kalman filtering with an intermediate AGCM. *Geophysical Research Letters*, 41(14):5264–5271.

Mlawer, E. J., Taubman, S. J., Brown, P. D., Iacono, M. J., and Clough, S. A. (1997). Radiative transfer for inhomogeneous atmospheres: RRTM, a validated correlated-k model for the longwave. *Journal of Geophysical Research: Atmospheres*, 102(D14):16663–16682.

Monin, A. S. and Obukhov, A. M. (1954). Basic laws of turbulent mixing in the surface layer of the atmosphere. *Contrib. Geophys. Inst. Acad. Sci. USSR*, 24(151):163–187.

Moore, A. M., Arango, H. G., Broquet, G., Edwards, C., Veneziani, M., Powell, B., Foley, D., Doyle, J. D., Costa, D., and Robinson, P. (2011a). The Regional Ocean Modeling System (ROMS) 4-dimensional variational data assimilation systems. Part II - Performance and application to the California Current System. *Progress in Oceanography*, 91(1):50–73.

Moore, A. M., Arango, H. G., Broquet, G., Edwards, C., Veneziani, M., Powell, B., Foley, D., Doyle, J. D., Costa, D., and Robinson, P. (2011b). The Regional Ocean Modeling System (ROMS) 4-dimensional variational data assimilation systems. Part III - Observation impact and observation sensitivity in the California Current System. *Progress in Oceanography*, 91(1):74–94.

Moore, A. M., Arango, H. G., Broquet, G., Powell, B. S., Weaver, A. T., and Zavala-Garay, J. (2011c). The Regional Ocean Modeling System (ROMS) 4-dimensional variational data assimilation systems. Part I - System overview and formulation. *Progress in Oceanography*, 91(1):34–49.

Munk, W. and Wunsch, C. (1998). Abyssal recipes II: energetics of tidal and wind mixing. *Deep Sea Research Part I: Oceanographic Research Papers*, 45(12):1977–2010.

Neef, L. J., Polavarapu, S. M., and Shepherd, T. G. (2006). Four-Dimensional Data Assimilation and Balanced Dynamics. *Journal of the Atmospheric Sciences*, 63(7):1840–1858.

Newinger, C. and Toumi, R. (2015). Potential impact of the colored Amazon and Orinoco plume on tropical cyclone intensity. *Journal of Geophysical Research: Oceans*, 120(2):1296–1317.

Oke, P. R., Sakov, P., Cahill, M. L., Dunn, J. R., Fiedler, R., Griffin, D. A., Mansbridge, J. V., Ridgway, K. R., and Schiller, A. (2013). Towards a dynamically balanced eddy-resolving ocean reanalysis: BRAN3. *Ocean Modelling*, 67:52–70.

Paduan, J. D. and Washburn, L. (2013). High-Frequency Radar Observations of Ocean Surface Currents. *Annual Review of Marine Science*, 5(1):115–136.

Parrish, D. F. and Derber, J. C. (1992). The National Meteorological Center's Spectral Statistical-Interpolation Analysis System.

Pascual, A., Bouffard, J., Ruiz, S., Buongiorno Nardelli, B., Vidal-Vijande, E., Escudier, R., Sayol, J. M., and Orfila, A. (2013). Recent improvements in mesoscale characterization of the western Mediterranean Sea: synergy between satellite altimetry and other observational approaches. *Scientia Marina*, 77(1):19–36.

Pham, D. T. (2001). Stochastic methods for sequential data assimilation in strongly nonlinear systems. *Monthly Weather Review*, 129(5):1194–1207.

Phillipson, L. and Toumi, R. (2017). Impact of data assimilation on ocean current forecasts in the Angola Basin. *Ocean Modelling*, 114:45–58.

Powers, J. G., Klemp, J. B., Skamarock, W. C., Davis, C. A., Dudhia, J., Gill, D. O., Coen, J. L., Gochis, D. J., Ahmadov, R., Peckham, S. E., Grell, G. A., Michalakes, J., Trahan, S., Benjamin, S. G., Alexander, C. R., Dimego, G. J., Wang, W., Schwartz, C. S., Romine, G. S., Liu, Z., Snyder, C., Chen, F., Barlage, M. J., Yu, W., and Duda, M. G. (2017). The weather research and forecasting model: Overview, system efforts, and future directions. *Bulletin of the American Meteorological Society*, 98(8):1717–1737.

Price, J. F. (1981). Upper Ocean Response to a Hurricane. *Journal of Physical Oceanography*, 11(2):153–175.

Price, J. F. (1983). Internal Wave Wake of a Moving Storm. Part I. Scales, Energy Budget and Observations. *Journal of Physical Oceanography*, 13:949–965.

Price, J. F., Sanford, T. B., and Forristall, G. Z. (1994). Forced Stage Response to a Moving Hurricane.

Reynolds, R. W., Smith, T. M., Liu, C., Chelton, D. B., Casey, K. S., and Schlax, M. G. (2007). Daily High-Resolution-Blended Analyses for Sea Surface Temperature. *Journal of Climate*, 20(22):5473–5496.

Rotunno, R. and Emanuel, K. a. (1987). An Air–Sea Interaction Theory for Tropical Cyclones. Part II: Evolutionary Study Using a Nonhydrostatic Axisymmetric Numerical Model.

Saha, S., Moorthi, S., Pan, H. L., Wu, X., Wang, J., Nadiga, S., Tripp, P., Kistler, R., Woollen, J., Behringer, D., Liu, H., Stokes, D., Grumbine, R., Gayno, G., Wang, J., Hou, Y. T., Chuang, H. Y., Juang, H. M. H., Sela, J., Iredell, M., Treadon, R., Kleist, D., Van Delst, P., Keyser, D., Derber, J., Ek, M., Meng, J., Wei, H., Yang, R., Lord, S., Van Den Dool, H., Kumar, A., Wang, W., Long, C., Chelliah, M., Xue, Y., Huang, B., Schemm, J. K., Ebisuzaki, W., Lin, R., Xie, P., Chen, M., Zhou, S., Higgins, W., Zou, C. Z., Liu, Q., Chen, Y., Han, Y., Cucurull, L., Reynolds, R. W., Rutledge, G., and Goldberg, M. (2010). The NCEP climate forecast system reanalysis. *Bulletin of the American Meteorological Society*, 91(8):1015–1057.

Scoccimarro, E., Gualdi, S., Bellucci, A., Sanna, A., Fogli, P. G., Manzini, E., Vichi, M., Oddo, P., and Navarra, A. (2011). Effects of tropical cyclones on ocean heat transport in a high-resolution coupled general circulation model. *Journal of Climate*, 24(16):4368–4384.

Seroka, G., Miles, T., Xu, Y., Kohut, J., Schofield, O., and Glenn, S. (2016). Hurricane Irene Sensitivity to Stratified Coastal Ocean Cooling. *Monthly Weather Review*, 144(9):3507–3530.

Shchepetkin, A. F. and McWilliams, J. C. (2005). The regional oceanic modeling system (ROMS): A split-explicit, free-surface, topography-following-coordinate oceanic model. *Ocean Modelling*, 9(4):347–404.

Shchepetkin, A. F. and McWilliams, J. C. (2009). Correction and commentary for "Ocean forecasting in terrain-following coordinates: Formulation and skill assessment of the regional ocean modeling system" by Haidvogel et al., J. Comp. Phys. 227, pp. 3595-3624. *Journal of Computational Physics*, 228(24):8985–9000.

Shuman, F. G. (1989). History of Numerical Weather Prediction at the National Meteorological Center. *Weather and Forecasting*, 4(3):286–296.

Skamarock, W., Klemp, J., Dudhi, J., Gill, D., Barker, D., Duda, M., Huang, X.-Y., Wang, W., and Powers, J. (2008). A Description of the Advanced Research WRF Version 3. *Technical Report*, (June):113.

Sluka, T. C., Penny, S. G., Kalnay, E., and Miyoshi, T. (2016). Assimilating atmospheric observations into the ocean using strongly coupled ensemble data assimilation. *Geophysical Research Letters*, 43(2):752–759.

Smit, A. J., Roberts, M., Anderson, R. J., Dufois, F., Dudley, S. F. J., Bornman, T. G., Olbers, J., and Bolton, J. J. (2013). A Coastal Seawater Temperature Dataset for Biogeographical Studies: Large Biases between In Situ and Remotely-Sensed Data Sets around the Coast of South Africa. *PLoS ONE*, 8(12):e81944.

Smith, P. J., Fowler, A. M., and Lawless, A. S. (2015). Exploring strategies for coupled 4D-Var data assimilation using an idealised atmosphere-ocean model. *Tellus, Series A: Dynamic Meteorology and Oceanography*, 67(1):1–25.

Smith, P. J., Lawless, A. S., and Nichols, N. K. (2017). Estimating Forecast Error Covariances for Strongly Coupled Atmosphere–Ocean 4D-Var Data Assimilation. *Monthly Weather Review*, 145(10):4011–4035.

Smith, W. H. (1997). Global Sea Floor Topography from Satellite Altimetry and Ship Depth Soundings. *Science*, 277(5334):1956–1962.

Song, H., Miller, A. J., McClatchie, S., Weber, E. D., Nieto, K. M., and Checkley, D. M. (2012). Application of a data-assimilation model to variability of Pacific sardine spawning and survivor habitats with ENSO in the California Current System. *Journal of Geophysical Research: Oceans*, 117(3):1–15.

Stepanov, V. N., Haines, K., and Smith, G. C. (2012). Assimilation of RAPID array observations into an ocean model. *Quarterly Journal of the Royal Meteorological Society*, 138(669):2105–2117.

Tewari, M., Chen, F., Wang, W., Dudhia, J., LeMone, M. A., Mitchell, K., Ek, M., Gayno, G., Wegiel, J., and Cuenca, R. H. (2004). Implementation and verification of the unified noah land surface model in the WRF model. *Bulletin of the American Meteorological Society*, pages 2165–2170.

Tintoré, J., Vizoso, G., Casas, B., Heslop, E., Pascual, A., Orfila, A., Ruiz, S., Martínez-Ledesma, M., Torner, M., Cusí, S., Diedrich, A., Balaguer, P., Gómez-Pujol, L., Álvarez-Ellacuria, A., Gómara, S., Sebastian, K., Lora, S., Beltrán, J. P., Renault, L., Juzà, M., Álvarez, D., March, D., Garau, B., Castilla, C., Cañellas, T., Roque, D., Lizarán, I., Pitarch, S., Carrasco, M. A., Lana, A., Mason, E., Escudier, R., Conti, D., Sayol, J. M., Barceló, B., Alemany, F., Reglero, P., Massuti, E., Vélez-Belchí, P., Ruiz, J., Oguz, T., Gómez, M., Álvarez, E., Ansorena, L., and Manriquez, M. (2013). SOCIB: The Balearic Islands Coastal Ocean Observing and Forecasting System Responding to Science, Technology and Society Needs. *Marine Technology Society Journal*, 47(1):101–117.

Tippett, M. K., Anderson, J. L., Bishop, C. H., Hamill, T. M., and Whitaker, J. S. (2003). Ensemble Square Root Filters*. *Monthly Weather Review*, 131(7):1485–1490.

Tonani, M., Balmaseda, M., Bertino, L., Blockley, E., Brassington, G., Davidson, F., Drillet, Y., Hogan, P., Kuragano, T., Lee, T., Mehra, A., Paranathara, F., Tanajura, C. A., and Wang, H. (2015). Status and future of global and regional ocean prediction systems. *Journal of Operational Oceanography*, 8(sup2):s201–s220.

Torn, R. D. and Hakim, G. J. (2008). Ensemble-Based Sensitivity Analysis. *Monthly Weather Review*, 136(2):663–677.

van Ruth, P. D., Ganf, G. G., and Ward, T. M. (2010). Hot-spots of primary productivity: An Alternative interpretation to Conventional upwelling models. *Estuarine, Coastal and Shelf Science*, 90(3):142–158.

Vetra-Carvalho, S., Dixon, M., Migliorini, S., Nichols, N. K., and Ballard, S. P. (2012). Breakdown of hydrostatic balance at convective scales in the forecast errors in the Met Office Unified Model. *Quarterly Journal of the Royal Meteorological Society*, 138(668):1709–1720.

Vorosmarty, C. J., Fekete, B., and Tucker, B. (1998). Global River Discharge, 1807-1991, Version 1.1 (RivDIS).

Wada, A. and Kunii, M. (2017). The role of ocean-atmosphere interaction in Typhoon Sinlaku (2008) using a regional coupled data assimilation system. *Journal of Geophysical Research: Oceans*, 122(5):3675–3695.

Wang, B., Ding, Q., Fu, X., Kang, I. S., Jin, K., Shukla, J., and Doblas-Reyes, F. (2005). Fundamental challenge in simulation and prediction of summer monsoon rainfall. *Geophysical Research Letters*, 32(15):2–5.

Wang, G., Wu, L., Johnson, N. C., and Ling, Z. (2016). Observed three-dimensional structure of ocean cooling induced by Pacific tropical cyclones. *Geophysical Research Letters*, 43(14):7632–7638.

Wang, S. and Toumi, R. (2016). On the relationship between hurricane cost and the integrated wind profile. *Environmental Research Letters*, 11(11).

Wang, S., Toumi, R., Czaja, A., and Kan, A. V. (2015). An analytic model of tropical cyclone wind profiles. *Quarterly Journal of the Royal Meteorological Society*, 141(693):3018–3029.

Wang, X., Barker, D. M., Snyder, C., and Hamill, T. M. (2008a). A Hybrid ETKF–3DVAR Data Assimilation Scheme for the WRF Model. Part I: Observing System Simulation Experiment. *Monthly Weather Review*, 136(12):5116–5131.

Wang, X., Barker, D. M., Snyder, C., and Hamill, T. M. (2008b). A Hybrid ETKF–3DVAR Data Assimilation Scheme for the WRF Model. Part II: Real Observation Experiments. *Monthly Weather Review*, 136(12):5132–5147.

Wang, X., Parrish, D., Kleist, D., and Whitaker, J. (2013). GSI 3DVar-Based Ensemble–Variational Hybrid Data Assimilation for NCEP Global Forecast System: Single-Resolution Experiments. *Monthly Weather Review*, 141(11):4098–4117.

Warner, J. C., Armstrong, B., He, R., and Zambon, J. B. (2010). Development of a Coupled Ocean–Atmosphere–Wave–Sediment Transport (COAWST) Modeling System. *Ocean Modelling*, 35(3):230–244.

Warner, J. C., Sherwood, C. R., Signell, R. P., Harris, C. K., and Arango, H. G. (2008). Development of a three-dimensional, regional, coupled wave, current, and sediment-transport model. *Computers and Geosciences*, 34(10):1284–1306.

Weaver, A. T., Deltel, C., Machu, E., Ricci, S., and Daget, N. (2005). A multivariate balance operator for variational ocean data assimilation. *Quarterly Journal of the Royal Meteorological Society*, 131(613):3605–3625.

Webster, P. J. (2005). Changes in Tropical Cyclone Number, Duration, and Intensity in a Warming Environment. *Science*, 309(5742):1844–1846.

White, R. H. and Toumi, R. (2014). River flow and ocean temperatures: The Congo River. *Journal of Geophysical Research: Oceans*, 119(4):2501–2517.

Wikle, C. K. and Berliner, L. M. (2007). A Bayesian tutorial for data assimilation. *Physica D: Nonlinear Phenomena*, 230(1-2):1–16.

Wilkin, J. L., Arango, H. G., Haidvogel, D. B., Lichtenwalner, C. S., Glenn, S. M., and Hedström, K. S. (2005). A regional ocean modeling system for the Long-term Ecosystem Observatory. *Journal of Geophysical Research: Oceans*, 110(6):1–13.

Wu, W.-S., Purser, R. J., and Parrish, D. F. (2002). Three-Dimensional Variational Analysis with Spatially Inhomogeneous Covariances. *Monthly Weather Review*, 130(12):2905–2916.

Yamaguchi, M., Ishida, J., Sato, H., and Nakagawa, M. (2017). WGNE Intercomparison of Tropical Cyclone Forecasts by Operational NWP Models: A Quarter Century and Beyond. *Bulletin of the American Meteorological Society*, 98(11):2337–2349.

Zhang, F., Meng, Z., and Aksoy, A. (2006). Tests of an Ensemble Kalman Filter for Mesoscale and Regional-Scale Data Assimilation. Part I: Perfect Model Experiments. *Monthly Weather Review*, 134(2):722–736.

Zhang, F., Weng, Y., Sippel, J. A., Meng, Z., and Bishop, C. H. (2009). Cloud-Resolving Hurricane Initialization and Prediction through Assimilation of Doppler Radar Observations with an Ensemble Kalman Filter. *Monthly Weather Review*, 137(7):2105–2125.